OPEN ACCESS

University of BRISTOL

Magee, C., Stevenson, C. T. E., Ebmeier, S. K., Keir, D., Hammond, J. O. S., Gottsmann, J. H., Whaler, K. A., Schofield, N., Jackson, C. A-L., Petronis, M. S., O'driscoll, B., Morgan, J., Cruden, A., Vollgger, S. A., Dering, G., Micklethwaite, S., & Jackson, M. D. (2018). Magma Plumbing Systems: A Geophysical Perspective. *Journal of Petrology*, [egy064]. https://doi.org/10.1093/petrology/egy064

Peer reviewed version

Link to published version (if available):
10.1093/petrology/egy064

Link to publication record in Explore Bristol Research
PDF-document

This is the author accepted manuscript (AAM). The final published version (version of record) is available online via Oxford University Press at https://academic.oup.com/petrology/advance-article/doi/10.1093/petrology/egy064/5043305 . Please refer to any applicable terms of use of the publisher.

University of Bristol - Explore Bristol Research
General rights

This document is made available in accordance with publisher policies. Please cite only the published version using the reference above. Full terms of use are available:
http://www.bristol.ac.uk/red/research-policy/pure/user-guides/ebr-terms/

Perspectives in Petrology

Magma Plumbing Systems: A Geophysical Perspective

[1]Craig Magee, [2]Carl T.E. Stevenson, [3]Susanna K. Ebmeier, [4,5]Derek Keir, [6]James O.S. Hammond, [7]Joachim H. Gottsmann, [8]Kathryn A. Whaler, [9]Nick Schofield, [1]Christopher A-L. Jackson, [10]Michael S. Petronis, [11]Brian O'Driscoll, [1]Joanna Morgan, [12]Alexander Cruden, [12]Stefan A. Vollgger, [13]Greg Dering, [12]Steven Micklethwaite, [1]Matthew D. Jackson,

[1]Department of Earth Science and Engineering, Imperial College London, London, SW7 2BP, UK

[2]School of Geography, Earth and Environmental Sciences, University of Birmingham, Birmingham, B15 2TT, UK

[3]School of Earth Science and Environment, University of Leeds, Leeds, LS2 9JT, UK

[4]Ocean and Earth Science, University of Southampton, Southampton, SO14 3ZH, UK

[5]Dipartimento di Scienze della Terra, Università degli Studi di Firenze, Florence, 50121, Italy

[6]Department of Earth and Planetary Sciences, Birkbeck, University of London, London, WC1E 7HX, UK

[7]School of Earth Sciences, University of Bristol, Bristol, BS8 1RJ, UK

[8]School of GeoSciences, University of Edinburgh, Grant Institute, Edinburgh, EH9 3FE, UK

[9]Geology and Petroleum Geology, School of Geosciences, University of Aberdeen, Aberdeen, AB24 3UE, UK

[10]Environmental Geology, Natural Resource Management Department, New Mexico Highlands University, PO Box 9000, Las Vegas, NM 87701, USA

[11]School of Earth and Environmental Sciences, University of Manchester, Manchester, M13 9PL, UK

[12]School of Earth, Atmosphere and Environment, Monash University, Melbourne, Victoria, 3800, Australia

[13]School of Earth Sciences, University of Western Australia, Perth, 6009, Australia

Abstract

Over the last few decades, significant advances in using geophysical techniques to image the structure of magma plumbing systems have enabled the identification of zones of melt accumulation, crystal mush development, and magma migration. Combining advanced geophysical observations with petrological and geochemical data has arguably revolutionised our understanding of and afforded exciting new insights into the development of entire magma plumbing systems. However, divisions between the scales and physical settings over which these geophysical, petrological, and geochemical methods are applied still remain. To characterise some of these differences and promote the benefits of further integration between these methodologies, we provide a review of geophysical techniques and discuss how they can be utilised to provide a structural context for and place physical limits on the chemical evolution of magma plumbing systems. For example, we examine how Interferometric Synthetic Aperture Radar (InSAR), coupled with Global Positioning System (GPS) and Global Navigation Satellite System (GNSS) data, and seismicity may be used to track magma migration in near real-time. We also discuss how seismic imaging, gravimetry, and electromagnetic data can image contemporary melt zones, magma reservoirs, and/or crystal mushes. These techniques complement seismic reflection data and rock magnetic analyses that delimit the structure and emplacement of ancient magma plumbing systems. For each of these techniques, with the addition of full-waveform inversion (FWI), the use of Unmanned Aerial Vehicles (UAVs), and the integration of geophysics with numerical modelling, we discuss potential future directions. We show that approaching problems concerning magma plumbing systems from an integrated petrological, geochemical, and geophysical perspective will undoubtedly yield important scientific advances, providing exciting future opportunities for the volcanological community.

1. Introduction

Igneous petrology and geochemistry are concerned with the chemical and physical mechanisms governing melt genesis, mobilisation, and segregation, as well as the transport/ascent, storage,

54 evolution, and eruption of magma. The reasons for studying these fundamental processes include
55 understanding volcanic eruptions, modelling the mechanical development of magma conduits and
56 reservoirs, finding magma-related economic ore deposits, exploring for active geothermal energy
57 sources, and determining the impact of magmatism in different plate tectonic settings on the
58 evolution of the lithosphere and crustal growth. However, whilst petrological and geochemical
59 studies over the last century have shaped our understanding of the physical and chemical evolution
60 of magma plumbing systems, assessing the distribution, movement, and accumulation of magma in
61 the Earth's crust from these data remains challenging. A key frontier in igneous petrological and
62 geochemical research thus involves deciphering how and where magma forms, the routes it takes
63 toward the Earth's surface, and where exactly it is stored.

64 This contribution will demonstrate how geophysical data can be used to determine the
65 architecture of magma plumbing systems, providing a structural framework for the interpretation of
66 petrological and geochemical data. To aid the alignment of petrological, geochemical, and
67 geophysical disciplines it is first important to delineate what we mean by 'magma'. We follow
68 Glazner *et al.,* (2016) and define magma as, "naturally occurring, fully or partially molten rock
69 material generated within a planetary body, consisting of melt with or without crystals and gas
70 bubbles and containing a high enough proportion of melt to be capable of intrusion and extrusion".
71 Importantly, this definition specifically considers that magma: (i) forms through the migration and
72 accumulation of partial melt that is initially distributed throughout pore spaces in a rock volume;
73 and (ii) is a suspension of particles (i.e. crystals, xenoliths, and/or bubbles) within melt (see
74 Cashman *et al.,* 2017). As magma starts to solidify, the proportion of suspended crystals and thus
75 the relative viscosity of the magma increases until a relatively immobile, continuous network of
76 crystals and interstitial melt develops; we term this a 'crystal mush' (e.g., Hildreth, 2004; Glazner *et*
77 *al.,* 2016; Cashman *et al.,* 2017). The rheological transition from a magma to a crystal mush is
78 partly dependent on its chemistry, but typically occurs abruptly when the particle volume increases
79 across the 50–65% range (Cashman *et al.,* 2017). Crystal mushes thus exist at or above the solidus

and generally cannot be erupted, although they may be partly entrained in eruptible magma as glomerocrysts, cumulate nodules, or restite (Cashman *et al.,* 2017). Migration of interstitial melt within a crystal mush can lead to its accumulation and, thus, formation of a magma. A magma plumbing system therefore consists of interconnected magma conduits and reservoirs, which store magma as it evolves into a crystal mush, ultimately fed from a zone of partial melting (e.g., Fig. 1). These definitions are supported by geophysical imaging and analyses of contemporary reservoirs, which show melt volumes in the mid- to upper crust are typically low (<10%) and likely exist within a crystal mush (e.g., Paulatto *et al.,* 2010; Koulakov *et al.,* 2013; Ward *et al.,* 2013; Hammond, 2014; Comeau *et al.,* 2015; Comeau *et al.,* 2016; Delph *et al.,* 2017). These definitions and geophysical data question the traditional view that magma resides in long-lived, liquid-rich, and volumetrically significant magma chambers. Following this, the emerging paradigm for igneous systems is thus that liquid-rich magma chambers are short-lived, transient phenomena with: (i) melt typically residing in mushes that develop through the incremental injection of small, distinct magma batches; and (ii) magma accumulating in thin lenses (e.g., Hildreth, 2004, Annen *et al.*, 2006; Annen, 2011; Miller *et al.*, 2011; Solano *et al.,* 2012; Cashman & Sparks, 2013; Annen *et al.*, 2015; Cashman *et al.,* 2017). We are now starting to view magmatic systems as a vertically extensive, transcrustal, interconnected networks of magma conduits and magma/mush reservoirs (Fig. 1) (e.g., Cashman *et al.,* 2017).

The current use of geophysical techniques within the igneous community can be separated into two distinct areas focused on either characterising active volcanic domains or investigating the structure and emplacement of ancient magma plumbing systems. For example, in areas of active volcanism, our understanding of magma plumbing system structure principally comes from the application of geophysical techniques that detect sites of magma movement or accumulation (e.g., Sparks *et al.,* 2012; Cashman & Sparks, 2013). Such geophysical techniques include Interferometric Synthetic Aperture Radar (InSAR; e.g., Biggs *et al.,* 2014), seismicity (e.g., recording of earthquakes associated with magma movement; e.g., White & McCausland, 2016), various seismic

imaging methods (e.g., Paulatto *et al.,* 2010; Hammond, 2014), gravimetry (e.g., Battaglia *et al.,* 1999; Rymer *et al.,* 2005), and electromagnetic techniques (Desissa *et al.,* 2013; Comeau *et al.,* 2015). These techniques allow examination of: (i) the temporal development of magma plumbing systems (e.g., Pritchard & Simons, 2004; Sigmundsson et al., 2010); (ii) vertical and lateral movements of magma (e.g., Keir *et al.,* 2009; Jay *et al.,* 2014); (iii) the relationship between eruption dynamics, volcano deformation, and intrusion (e.g., Sigmundsson *et al.,* 2010; Sigmundsson *et al.,* 2015); and (iv) estimates of melt sources and melt fractions (e.g., Desissa *et al.,* 2013; Johnson *et al.,* 2016). However, inversion of these geophysical data typically results in non-unique, relatively low-resolution models of subsurface structures. Furthermore, some methods only capture active processes, which may be short-lived or even instantaneous, potentially providing information on only a small fraction of the magma plumbing system.

In contrast to the study of active volcanic domains, the analysis of ancient plumbing systems through field observations, geophysical imaging techniques (e.g., reflection seismology, gravity, and magnetic data), and/or rock magnetic experiments can provide critical insights into magma emplacement, mush evolution, and allow the geometry of entire plumbing systems to be reconstructed (e.g., Cartwright & Hansen, 2006; Stevenson *et al.,* 2007a; Petronis *et al.,* 2013; Muirhead *et al.*, 2014; O'Driscoll *et al.,* 2015; Magee *et al.*, 2016). Whilst such studies of ancient plumbing systems provide a framework for interpreting the structure of active intrusion networks, capturing a snapshot of how magma moved and melt was distributed through the system at any one time is difficult because magmatism has long since ceased.

All the techniques employed to define active and ancient plumbing systems, including petrological and chemical analyses, provide information at different spatial and/or temporal resolutions. Answering the major outstanding questions in studies of magma plumbing systems therefore requires the integration of complementary petrological, geochemical, geophysical, geochronological, and structural techniques. Here, we examine active plumbing systems using InSAR, seismicity, seismic imaging, gravimetry, and electromagnetic techniques. To provide a

context for the interpretation of data pertaining to the active systems, we also discuss how seismic reflection data and rock magnetic techniques can be used to derive the structure and evolution of ancient intrusion networks. The potential of emerging techniques involving seismic full-waveform inversion (FWI) and unmanned aerial vehicles (UAVs) are also considered, as is the role of numerical modelling in bringing together outputs from different datasets. For each technique described, we briefly discuss the methodology and limitations and provide a summary of the key findings and potential uses, with a focus on integration with petrological and geochemical data. The aim of this review is to facilitate and promote integration between petrologists, geochemists, geochronologists, structural geologists, and geophysicists interested in addressing outstanding problems in studies of magma plumbing systems.

2. Understanding magma plumbing system structure

Here, we discuss a range of techniques that can be utilised to define different aspects of magma plumbing system structure and evolution. In particular, we describe how InSAR, seismicity, seismic imaging (e.g., seismic tomography), gravity, and electromagnetic data is used to determine melt fractions and distribution, track movement of magma in near real-time, and/or locate sites and examine the evolution of magma/mush storage. Overall, these geophysical techniques allow the structure of active plumbing systems and their transient evolution to be assessed. We also discuss how seismic reflection data can provide unprecedented images of ancient plumbing systems and associated host rock deformation in three-dimensions at resolutions of 10's of metres. Finally, we examine the application of rock magnetic techniques to assess magma flow and crystallisation processes at a range of scales.

Although beyond the scope of this review, it is critical to highlight that interpreting the geophysical response of a rock or magma relies on understanding its physical and chemical properties (e.g., density, temperature, and melt fraction). Laboratory experiments testing how rock or magma properties influence geophysically measured parameters (e.g., seismic velocities and

158 resistivity) thus provide context for interpreting magma plumbing system structure and evolution
159 from geophysical data (e.g., Gaillard, 2004; Pommier *et al.,* 2010; Pommier, 2014).
160
161 **2.1. Insights into magma plumbing systems from ground deformation data**
162 ***Technique***
163 Changes in volume within magma plumbing systems can deform the host rock, potentially resulting
164 in displacement of the Earth's surface. Such displacements are a unique source of information for
165 volcanologists and can be modelled to estimate geodetic source depth and, to varying extents, the
166 source geometry and volume change (e.g., Segall, 2010). Measuring the deformation of the Earth's
167 surface can thus provide information about the characteristics and timing of magma movement and
168 accumulation, as well as variations in internal reservoir conditions. Traditionally, deformation
169 measurements are made using levelling, electronic distance meters, tiltmeters, and Global
170 Positioning System (GPS), all of which have proven to be reliable methods and thus are widely
171 used in volcano monitoring (e.g., Dzurisin, 2006). For example, GPS measurements retrieve the
172 relative positions of receivers on Earth's surface from dual frequency carrier phase signals
173 transmitted from GPS or Global Navigation Satellite System (GNSS) satellites with precisely
174 known orbits. Distances between satellites and receivers are assessed from the travel-time, i.e. the
175 measured difference between the transmitted and received times of a unique ranging code, allowing
176 movement of the Earth's surface over time to be monitored (see review by Dixon, 1991).
177 Permanently installed receivers record position data continuously, but receivers can also be
178 deployed for a limited time during GPS campaigns to provide additional measurements, normally
179 made relative to a standard benchmark location (e.g., Dvorak & Dzurisin, 1997). Whilst tiltmeters
180 and GPS can provide continuous measurements, their spatial resolution is limited by logistical
181 constraints such as cost and accessibility, which may be restricted at active volcanoes.
182 The geographic reach of volcano geodesy has been greatly expanded over the past two
183 decades by the application of Interferometric Synthetic Aperture Radar (InSAR), an active remote

sensing technique that uses microwave electromagnetic radiation to image the Earth's surface (e.g., Simons & Rosen, 2007; Pinel *et al.,* 2014). Surface displacements can be measured by constructing interferograms, where the difference in phase between radar echoes from time-separated images appear as 'fringes' of variation in the line of sight distance to the satellite (Fig. 2). The patterns of fringes in individual interferograms are distinctive for different deformation source geometries, such as for horizontal (sill-like) or vertical (dyke-like) opening of intrusions, or the pressurisation of a spheroidal reservoir (i.e. a Mogi source) (e.g., Fig. 2b). However, magma intrusion processes can rarely be uniquely identified from geodetic source geometry alone, and distinguishing between magmatic, hydrothermal, structural (e.g., faulting and compaction), and combinations of elastic and inelastic sources is particularly challenging (e.g., Galland, 2012; Holohan *et al.,* 2017).

Whilst a single interferogram only provides displacements in satellite line-of-sight, a pseudo-3D displacement field can be estimated by combining multiple images from polar orbits that are ascending (i.e. satellite moves roughly northward, looking east) and descending (i.e. satellite moves roughly southward, looking west) (Fig. 2a), especially where GNSS measurements can also be incorporated. The lateral spatial resolution of most InSAR data is on the order of metres to tens of metres, whilst vertical movements can be resolved on the order of centimetres and sometimes millimetres. Temporal resolution depends on the satellite revisit time and ranges between days to months depending upon the sensor type and satellite orbit. This means that InSAR can be used to regularly assess ground deformation at virtually any volcano worldwide situated above sea level, with a higher spatial density of measurements than achieved using from ground-based instrumentation.

Magmatic processes are only observable by InSAR when either magma movement or internal reservoir processes (e.g., cooling and contraction, phase changes) cause changes in pressure and thereby instigate deformation of the host rock and free surface. The best-fit parameters of a deformation source (e.g., an intruding magma body) are most often assessed by inverting measured displacements using analytical elastic-half space models of simple source geometries, although

there are often trade-offs between parameters such as source depth and volume change (e.g., Pritchard & Simons, 2004). Complex and more realistic deformation source geometries may be retrieved using finite element-based linear inversion of displacement fields (e.g., Ronchin *et al.,* 2017). A proportion of any pressure change may be accommodated by magma compressibility, leading to underestimation of volume changes (e.g., Rivalta & Segall, 2008; McCormick-Kilbride *et al.,* 2016). Assessing both volume changes and especially the total volume of a magma reservoir from geodetic data therefore remains challenging. Furthermore, host rocks in areas of repeated intrusion that have been heated above the brittle-ductile transition are better described by a viscoelastic rheology (e.g., Newman *et al.,* 2006; Yamasaki *et al.,* 2018), while ductile accommodation of volume changes may occur at greater depth. Where some constraints are available for the structure and rheology of Earth's crust, finite or boundary element models may achieve a more realistic model of the deformation source (e.g., Masterlark, 2007; Hickey *et al.,* 2017; Gottsmann *et al.,* 2017).

Observations

Measurements of volcano deformation preceding and/or accompanying eruption have provided insights into the extent and structure of magma plumbing systems and, in some instances, the dynamics of magma movement. For example, InSAR-based observations at Eyjafjallajökull, Iceland have recognised the intrusion of multiple, distinct sills over a decade and their subsequent extraction when tapped during an explosive eruption (e.g., Pedersen & Sigmundsson, 2006; Sigmundsson *et al.,* 2010). Extensive lateral connections via dykes and sills between reservoirs and/or volcanoes have been illuminated by eruptions or unrest accompanied by ground deformation tens of kilometres away, and by the existence of multiple deformation sources (e.g., Alu-Dalafilla shown in Figures 3 and b, Pagli *et al.,* 2012; Korovin, Lu & Dzurisin, 2014; Cordon-Caulle, Jay *et al.,* 2014; Kenyan volcanoes, Biggs *et al.,* 2014; global synthesis, Ebmeier *et al.,* 2018). Inter-eruptive deformation at calderas is especially complex and seems to be particularly frequent and

high magnitude (e.g., Laguna del Maule; Fournier *et al.,* 2010; Singer *et al.,* 2014; Le Mével *et al.,* 2015), with the location of the deformation sources inferred to vary over time (e.g., Campi Flegrei, Trasatti *et al.,* 2004; Yellowstone, Wicks *et al.,* 2006). The geometries of dykes and sills inferred from InSAR data inform our understanding of changing subsurface stress fields (e.g., Afar, Hamling *et al.,* 2010; Fernandina, Bagnardi *et al.,* 2013), as do measurements of displacements caused by moderate earthquakes in close proximity to magma plumbing systems (e.g., Kilauea, Wauthier *et al.,* 2013; Chiles-Cerro Negro, Ebmeier *et al.,* 2016).

At a transcrustal scale, deformation measurements have contributed to evidence for temporal variations in magma supply rates (e.g., in Hawaii, Poland *et al.,* 2012). Volume increases in the mid- to lower-crust, notably in the Central Andes, have provided the first observations of deep pluton growth (Pritchard & Simons, 2004). Furthermore, uplift during episodes of unrest that have not (yet) resulted in eruption have been detected at a broad range of volcanoes (e.g., Westdahl, Mount Peulik, Lu & Dzurisin, 2014; Alutu and Corbetti, Biggs *et al.,* 2011) and, in some cases, have been interpreted as evidence for the 'pulsed' accumulation of potentially eruptible magma (e.g., Santorini, Parks *et al.,* 2012). In addition to magma movement, volume changes associated with internal reservoir processes can also cause deformation of the host rock and free surface. For example, InSAR measurements have recorded subsidence linked to cooling and crystallisation of sills (Medicine Lake, Parker, 2016; Taupo Volcanic Zone, Hamling *et al.,* 2015). Transient periods of subsidence during inter-eruptive uplift have been attributed to phase transitions in response to the addition of more juvenile magma (e.g., Okmok, Caricchi *et al.,* 2014).

Implications and integration

InSAR has increased the number of volcanoes where measurements of ground deformation have been made, from less than 50 in the late 1990s to over 200 today (Biggs & Pritchard, 2017; Ebmeier *et al.,* 2018). This increase in coverage has been particularly influential in the developing world where monitoring infrastructure is typically poor (Ebmeier *et al.,* 2013; Chaussard *et al.,* 2013),

262 with InSAR often providing the first evidence of magmatic activity at many volcanoes previously
263 considered to be inactive (e.g., Pritchard & Simons, 2004; Biggs *et al.,* 2009; Biggs *et al.,* 2011; Lu
264 & Dzurisin, 2014). A continued increase in the number and range of satellite- and large-scale UAV-
265 based SAR instruments, as well as enhancements to their spatial and temporal resolution, will allow
266 the detection of a greater range of volcanic ground deformation (e.g., Salzer *et al.,* 2014; Schaefer *et*
267 *al.,* 2015; Stephens *et al.,* 2017). Overall, improved InSAR coverage will also increase the number
268 of volcanoes where deformation measurements have been made across multiple cycles of eruption
269 and deformation, increasing its usefulness for both hazard assessment and for characterising the
270 extent, geometry, and changes in magma plumbing systems.
271 Geodetic measurements provide information only about the parts of a plumbing system that
272 are currently active, and do not necessarily reflect the full extent and character of the intrusion
273 network (e.g., Sigmundsson, 2016). However, geodetic analyses of ground deformation provide
274 critical insight into the spatial and temporal development of active plumbing systems. Comparing
275 observations of ancient plumbing systems (e.g., Magee *et al.,* 2013; Schofield *et al.,* 2014),
276 integration of ground deformation measurements with petrological observations (e.g., Caricchi *et*
277 *al.,* 2014; Jay *et al.,* 2014) or thermal models (Parker *et al.,* 2016), as well as tomographic
278 geophysical imaging, will increase the sophistication of models of magmatic systems. Integrating
279 InSAR with gravity or electromagnetic measurements is particularly powerful, as it can allow
280 discrimination between melt, volatiles, and hydrothermal fluids for which deformation signals are
281 similar (see section 2.4) (e.g., Tizzani *et al.,* 2009).
282
283 **2.2. Seismicity and magma plumbing systems**
284 ***Technique***
285 Seismicity (i.e. earthquakes) at volcanoes is primarily caused by the dynamic interaction of magma
286 and hydrothermal fluids with the solid host rock (e.g., Chouet & Matoza, 2013), as well as by
287 fracturing and fragmentation of silicic magma (e.g., Tuffen *et al.,* 2008). There are a number of

primary physical mechanisms for causing volcano seismicity (e.g., faulting), each of which typically produces seismic signals of specific frequency content (Chouet & Matoza, 2013). Recording and isolating different volcano seismicity signals therefore allows a variety of plumbing system processes to be assessed. The majority of volcano monitoring agencies have now deployed or aim to use a network of distributed seismic sensors, including broadband seismometers, to monitor volcano activity (Neuberg *et al.,* 1998; Sparks *et al.,* 2012). Furthermore, an increase in computing power and reduction in cost of seismic sensors means that researchers are now developing fast, fully automated detection and real-time location techniques that can locate seismicity to sub-decimetre precision (e.g., Drew *et al.,* 2013; Sigmundsson *et al.,* 2015).

Observations

Volcano-tectonic (VT) seismicity generally produces relatively high frequency (1–20 Hz), short period signals, involving clear primary (P), secondary (S), and surface waves, which are caused by displacement on new or existing faults in the host rock in response to fluid-induced stress changes (e.g., Rubin & Gillard, 1998; Roman & Cashman, 2006; Tolstoy *et al.,* 2008). These earthquakes commonly occur near the propagating edge of intrusions, meaning the space-time evolution of VT earthquake locations can be used to track the horizontal and vertical growth of sills and dykes (e.g., Keir *et al.,* 2009; Sigmundsson *et al.,* 2010; Sigmundsson *et al.,* 2015). Inflation of a magma or mush body can also induce VT seismicity on any preferentially oriented faults surrounding the intrusion, thereby recording the delivery time and locus of new magma injected into a reservoir (e.g., Roman & Cashman, 2006; Vargas-Bracamontes & Neuberg, 2012).

Earthquakes with longer period seismic signals and low-frequencies (0.5–2 Hz) are thought to be generated near the interface between magma and solid rock (Chouet & Matoza, 2013). The earthquake source proximity to the magma causes the seismic signal to resonate in parts of the plumbing system (e.g., conduits, dykes, and cracks), leading to a reduction in its frequency content (Chouet & Matoza, 2013). These earthquakes can potentially be caused by stick-slip motion

between the magma and wall-rock or fracturing of cooling magma near the conduit wall (Neuberg *et al.,* 2006; Tuffen *et al.,* 2008). Such earthquakes typically occur at restricted portions of conduits where the magma flow and shear strain rate are highest (Neuberg *et al.,* 2006; Tuffen *et al.,* 2008).

Very long period seismicity (VLP) of 10s of seconds to several minutes period are typically attributed to inertial forces associated with perturbations in the flow of magma and gases through conduits (Chouet & Matoza, 2013). These signals can record the response of the host rock to reservoir inflation and deflation and may be used to model conduit shape and size (Chouet *et al.,* 2008). To do this requires a better understanding of the links between flow processes and resultant pressure/momentum changes using laboratory experiments and numerical models that include the elastic response to magma flow across multiple signal frequency bands (e.g., Thomas & Neuberg, 2012).

Implications and integration

Studies of evolving reservoirs now aim to link episodes of seismicity related to new magma injection to petrological evidence for timing of reservoir recharge events, thereby providing independent constraints on day to year-long time-scales of magma residence and input prior to eruptions. For example, Fe-Mg diffusion chronometry modelling of orthopyroxene crystals from the 1980–1986 eruption of Mount St. Helens indicates that compositionally distinct rims grew within 12 months prior to eruption (Fig. 4) (Saunders *et al.,* 2012). Peaks in crystal growth correlated extremely well with increased seismicity and SO_2 flux (Fig. 4), confirming the relationship between seismicity and magma movement, as well as demonstrating how a combination of seismicity and petrological information can be used to detect magma injections (Saunders *et al.,* 2012).

Petrology and seismicity can also be integrated with other methods, such as GPS and InSAR. Field *et al.,* (2012) analysed volatiles in melt inclusions trapped in phenocrysts within peralkaline lavas from historic eruptions at the Dabbahu Volcano in Afar, Ethiopia. Volatile saturation pressures at typical magmatic temperatures were constrained to be in the range 43–207

MPa, consistent with the phenocryst assemblage being stable at 100–150 MPa. The interpreted magma/mush storage depths for these historic eruptions are ~1–5 km, consistent with the depths of earthquakes associated with reservoir inflation following dyke intrusion in 2005–2006 (Fig. 5) (Ebinger *et al.,* 2008; Field *et al.,* 2012). Additionally, the best-fit result for modelling of uplift patterns recorded by InSAR data, which were collected over the same time period as seismicity measurement, suggests the magma/mush reservoir comprises a series of stacked sills over a ~1–5 km depth range (Fig. 5) (Ebinger *et al.,* 2008). The consistency of depth estimates based on petrological study of ancient eruptions, along with the seismicity and inflation of the Dabbahu Volcano following axial dyke intrusion in 2005–2006, implies a vertically extensive and potentially long-lived magma/mush storage region. Such multidisciplinary studies demonstrate that joint observations and modelling of seismic signals, petrological data, and other techniques (e.g., geodesy and gas emissions) significantly strengthen interpretation of the physical structure, emplacement, and evolution of magma plumbing systems.

2.3. Identifying melt in plumbing systems using seismic imaging

Techniques

Both active and passive source seismological techniques, which utilise man-made seismic events and natural earthquakes respectively, can be used to identify areas where the presence of partial melt or magma causes a local reduction in seismic wavespeed, an increase in anisotropy, or an increase in attenuation (e.g., Berryman, 1980; Hammond & Humphreys, 2000a, b). With the recent availability of dense seismic networks, resolution of the crust and mantle seismic velocity structure has improved to the degree that active source seismic experiments can: (i) use tomographic techniques to image likely storage regions in the upper crust beneath ocean island volcanoes (e.g., Soufrière Hills Volcano, Montserrat; Fig. 6) (Paulatto *et al.,* 2010; Shalev *et al.,* 2010) and, occasionally, onshore volcanoes (e.g., Mt Erebus, Antarctica, Zandomeneghi *et al.,* 2013; Mt. St. Helens, Kiser *et al.,* 2014); and (ii) utilise reflected data to image individual sills beneath mid-ocean

366 ridges (e.g., Kent *et al.,* 2000, Marjanovic *et al.,* 2014). A further example from Katla volcano
367 Iceland, demonstrates how active source seismic experiments can be used to identify S-wave
368 shadow zones (i.e. S-waves cannot travel through fluids) and delays in P-waves, which may be used
369 to infer the location and geometry of shallow-level magma reservoirs (Gudmundsson *et al.,* 1994).
370 However, recent modelling approaches suggest that the upper crust likely represents only a small
371 portion of magma plumbing systems and long-term storage is dominated by mushy zones
372 throughout the lower crust (e.g., Annen *et al.,* 2006). Active source seismic experiments,
373 particularly on land where the crust is thick and coverage less uniform, cannot penetrate to these
374 depths efficiently. Furthermore, whilst seismic tomographic methods using local earthquakes offer
375 3D images of crustal velocity beneath many volcanoes (e.g., Mt. St. Helens, Waite & Moran, 2009;
376 Askja, Iceland, Mitchell *et al.,* 2013), they can only resolve areas directly above the deepest
377 earthquakes. Non-uniform coverage thus makes interpreting tomographic images difficult as
378 resolution varies across the model (see review by Lees, 2007).
379 To illuminate lower crustal regions, seismologists rely on passive seismology. Extending
380 seismic tomographic images of magma plumbing systems to lower crustal depths requires the use of
381 teleseismic body-wave and surface wave data, which emanate far (>1000 km) from the
382 measurement site. However, these data are dominated by longer period signals, meaning their
383 resolution is relatively low. For example, the Fresnel zone (i.e. the region within ¼ seismic
384 wavelength and an estimate of the minimum resolvable structure) for active source data at 10 Hz is
385 on the order of 3 km in the upper crust compared to 10–15 km for 1 Hz teleseismic data used in
386 receiver function or tomography studies.
387
388 ***Observations***
389 Active and passive seismological techniques provide crucial insight into transcrustal melt and
390 magma distribution. For example, P-wave seismic travel-time tomography across Monserrat and the
391 Soufrière Hills Volcano images a series of relatively fast seismic velocity zones, which are

interpreted as solidified andesitic intrusions, surrounded by regions of slow seismic velocities likely related to either areas of hydrothermal alteration or buried volcaniclastic deposits (Fig. 6) (Paulatto *et al.,* 2010; Shalev *et al.,* 2010). Within the lower crust, inversions using surface wave data generated by ambient seismic noise and receiver function data, which isolates P-wave to S-wave conversions at major discontinuities in the earth, have identified low shear-wave velocities probably related to melt presence beneath several volcanic settings (e.g., New Zealand, Bannister *et al.,* 2007; Toba, Sumatra, Stankiewicz *et al.,* 2010; Ethiopia, Hammond *et al.,* 2011; Jaxybulatov *et al.,* 2014; Costa Rica, Harmon & Rychert, 2015).

When trying to determine how much melt or magma is present, numerous studies have shown that seismic velocities are more sensitive to the shapes of melt/magma-filled spaces on a range of scales compared to the melt fraction (e.g., Hammond & Humphreys, 2000a, b; Miller & Savage, 2001; Johnson & Poland, 2013; Hammond & Kendall, 2016). On the grain-scale, melt commonly wets grain boundaries, forming planar pockets (e.g., Takei, 2002; Garapic *et al.,* 2013; Miller *et al.,* 2014), whereas on the larger scale magma may form planar intrusions of either mush (e.g., Annen *et al.,* 2006), or liquid-rich dykes or sills. If these features are preferentially aligned, they will appear as a distributed region of melt to seismic waves and the analyses described will not be able to discriminate between a melt-poor region dominated by aligned melt-pockets on grain boundaries and an elongate melt-rich body such as an intrusion (e.g., Hammond & Kendall, 2016). A further problem is that seismic velocities are affected by variations in temperature (Jackson *et al.,* 2002), composition (Karato & Jung, 1998), and attenuation (Goes *et al.,* 2012). Relating seismic velocity anomalies to melt fraction is therefore difficult without some prior knowledge of melt distribution (Hammond & Kendall, 2016).

One possible approach to investigate melt distributions further is through measuring seismic anisotropy. If melt has some preferential distribution on a length-scale smaller than the seismic wavelength, such as a stacked network of sills or an anisotropic permeability on the grain scale, then the seismic wavespeed will vary with direction of propagation, i.e. be anisotropic. As a result,

418 measuring the effects of seismic anisotropy allows inferences about sub-seismic wavelength
419 structures, leading to estimates of the preferential orientation of melt distribution. It is common to
420 observe strong anisotropy beneath volcanoes and this has been used to place constraints on melt
421 distribution. For example, high degrees of shear-wave splitting from volcanic earthquakes can either
422 directly map out regions of significant quantities of melt aligned in pockets (Keir *et al.,* 2011), or
423 map out stress changes related to overpressure from injections of magma into the upper crust (Gerst
424 & Savage, 2004; Roman *et al.,* 2011). To image the deeper crustal magmatic system, azimuthal
425 variations in the ratio of P-wave to S-wave speeds (i.e. V_P/V_S) from receiver functions led to the
426 interpretation that a stacked network of sills is present in the lower crust beneath the Afar
427 Depression, Ethiopia (Hammond, 2014). Differences in the velocity of Rayleigh Waves and Love
428 Waves, which are vertically polarised shear-waves and horizontally polarised shear waves
429 respectively, suggest a similar anisotropic melt distribution is present beneath the Toba Caldera,
430 Sumatra (Jaxybulatov *et al.,* 2014) and Costa Rica (Harmon & Rychert, 2015).
431
432 ***Implications and integration***
433 Due to the interference of signals denoting the geometry of melt-filled pockets and the volumetric
434 proportion of that melt, estimating melt fraction remains difficult using seismology alone. Some
435 attempt has been made to directly infer magma/mush reservoir properties from seismic velocities.
436 For example, Paulatto *et al.,* (2012) used thermal modelling to test the range of melt fractions that
437 could account for the low velocity zones imaged in the upper crust beneath Soufrière Hills Volcano
438 (Fig. 6), Montserrat and concluded the melt fraction is between 3 and 10%. However, accounting
439 for resolution of the tomography, together with uncertainties in the distribution and geometry of
440 melt, means >30% melt may be present more locally in the low velocity zones defined beneath
441 Soufrière Hills Volcano (Paulatto *et al.,* 2012). Possible ways forward involve integrating
442 seismological data with: (i) petrological data that can place limits on likely melt fractions and/or
443 emplacement depths (e.g., McKenzie & O'Nions, 1991; Comeau *et al.,* 2016); (ii) geochemical

444 techniques that can help determine timescales of melt and magma evolution (e.g., Hawkesworth *et*
445 *al.,* 2000); and (iii) geodetic or other monitoring data, which helps determine magma movement
446 (Sturkell *et al.,* 2006). Recent efforts applying industry software, such as full waveform inversions
447 (FWI; Warner *et al.,* 2013), which is discussed in section 3.1, are also pushing the potential
448 application of seismological data further and mean that it may be possible to resolve features to sub-
449 kilometre levels, particularly in the upper crust. Together, these techniques may allow us to directly
450 relate seismic velocity anomalies to melt fractions and distributions in the whole crust.
451
452 **2.4. Studying magma plumbing systems using gravimetry**
453 ***Techniques***
454 Gravimetry measures the gravitational field and its changes over space and time, which can be
455 related to variations in the subsurface distribution and redistribution of mass (e.g., magma). A
456 variety of gravimeter instruments (e.g., free-fall, superconducting, and spring-based) and techniques
457 (e.g., ground-based, sea-floor, ship-borne, and air-borne instrumentations) are available. Spring
458 gravimeters, where a test mass is suspended on a spring, are mostly used to study magmatic and
459 volcanic processes in ground-based surveys (e.g., Carbone *et al.,* 2017; Van Camp *et al.,* 2017).
460 Changes in the gravitational acceleration across a survey area shorten or lengthen the spring, which
461 is recorded electronically and converted to gravity units. These changes are evaluated across a
462 survey network in relation to a reference and are hence termed 'relative measurements'. Absolute
463 gravimetry can also be measured, i.e. the value of gravitational acceleration, and serves primarily to
464 create a reference frame into which other geodetic methods (e.g., InSAR, GNSS, levelling, relative
465 gravimetry) can be integrated for joint data evaluation. Recent reviews by Carbone *et al.,* (2017)
466 and Van Camp *et al.,* (2017) provide a broad account of gravimetric instruments, measurement
467 protocols, and data processing relevant for the study of magmatic systems.
468 Static gravimetric techniques obtain a single snap-shot of the subsurface mass distribution.
469 For example, Bouguer anomaly maps are perhaps the best-known products of static gravity surveys

and capture spatial variations in gravity over an area of interest, providing insight into anomalous mass distribution in the subsurface. Within magmatic studies, computational modelling and inversion of Bouger anomaly data allows identification of shallow intrusions (e.g., dykes and sills; Rocchi *et al.,* 2007), magma-related ore bodies (Hammer, 1945; Bersi *et al.,* 2016), and plutons (e.g., Figs 7a and b) (e.g., Vigneresse, 1995; Vigneresse *et al.,* 1999; Petford *et al.,* 2000) exhibiting a density contrast with their host rocks.

In contrast to static surveys, dynamic gravimetric observations allow spatio-temporal mass changes to be tracked. Dynamic gravimetric studies investigate how the subsurface architecture changes over time and is usually performed by measuring variations in gravity across a network of survey points (e.g., Fig. 7c) or, in a few exceptional cases, by installing a network of continuously operating gravimeters. Dynamic observations demand one-to-two orders of magnitude higher data precision (i.e. to a few μGal where 1 μGal = 10^{-8} m/s^2) compared to static surveys, making them an elaborate and time-consuming exercise. However, dynamic gravity data yields important insights into the source processes behind non-tectonic volcano and crustal deformation, particularly if combined with surface deformation data (e.g., InSAR and GNSS) as subsurface mass and volume changes can be employed to characterise the density of the material behind the stress changes (Figs 7c-f and 8) (e.g., Battaglia & Segall, 2004; Jachens & Roberts, 1985; Poland & Carbone, 2016). There are also cases where volcano unrest, due either to magma intrusion into a ductile host rock or to volatile migration at shallow depths, does not result in resolvable surface deformation; in these scenarios, gravity data have provided vital clues about subsurface processes otherwise hidden from conventional monitoring techniques (e.g., Gottsmann *et al.,* 2006; Gottsmann *et al.,* 2007; Miller *et al.,* 2017).

Whilst static and dynamic gravimetric observations offer considerable insight into the structure and dynamics of magma plumbing systems, care must be exercised when collecting and interpreting gravity data from active magmatic areas where seasonal variations in hydrothermal systems, aquifers, or the vadose zone can influence subsurface mass distribution (e.g., Hemmings *et*

al., 2016). These seasonal changes can, in some cases, result in data aliasing artefacts and inhibit the quantification of deeper-seated magmatic processes (e.g., Gottsmann *et al.,* 2005; Gottsmann *et al.,* 2007).

Observations

Gravimetric investigations have been at the heart of studies into the subsurface structure of active and ancient magma plumbing systems for more than 80 years (e.g., Carbone *et al.,* 2017; Van Camp *et al.,* 2017). Using techniques initially designed for imaging salt domes, silicic plutons were the first components of magma plumbing systems to be examined using gravimetry because their low density relative to surrounding rocks produces clear, negative gravity anomalies of ~10 to ~40 mGal amplitude (e.g., Reich, 1932; Bucher, 1944; Bott, 1953). Gravity data have been instrumental in the investigation of upper-crustal, silicic magma plumbing systems, helping to reveal: (i) the 3D geometry of plutons by allowing floor morphologies (e.g., flat-floored or wedge-shaped) to be determined (e.g., Vigneresse *et al.,* 1999; Petford *et al.,* 2000); and (ii) how plutons are constructed, for example, by the amalgamation of multiple intrusions fed from depth by dykes (e.g., Vigneresse, 1995). Furthermore, recent high-precision static surveys over active silicic volcanoes have enabled detailed modelling of the sub-volcanic magma plumbing system, commonly demonstrating the occurrence of vertically extensive, transcrustal magma bodies (Figs 7a and b) (e.g., Gottsmann *et al.,* 2008; del Potro *et al.,* 2013; Saxby *et al.,* 2016; Miller *et al.,* 2017). In addition to examining silicic magma plumbing systems, negative gravity anomalies with typical amplitudes of up to 60 mGal and up to 100 km wavelength can be associated with, and provide insight into, the geometry and size of silicic ash-flow calderas (e.g., Eaton *et al.,* 1975; Masturyono *et al.,* 2001). Positive gravity anomalous with amplitudes of up to 30 mGal and wavelengths of up to 20 km are commonly identified at mafic volcanoes and likely result from dense intrusive complexes (e.g., Rymer & Brown, 1986).

521 Dynamic gravity observations have provided unprecedented insight into the evolution of
522 magma plumbing systems over timescales of seconds to decades, including: (i) the characterisation
523 of multi-year lava lake dynamics (e.g., Poland & Carbone, 2016); (ii) mass budgets of magma
524 intrusions (e.g., Fig. 8) (e.g., Battaglia *et al.,* 1999; Jousset *et al.,* 2000; Rymer *et al.,* 2005;
525 Bonforte *et al.,* 2007; Tizzani *et al.,* 2009); (iii) shallow hydrothermal fluid flow processes induced
526 by deeper magmatic unrest (e.g., Battaglia *et al.,* 2006; Gottsmann *et al.,* 2007; Miller *et al.,* 2017);
527 and (iv) parameters of magmatic geothermal reservoirs (e.g., Hunt & Bowyer, 2007; Sofyan *et al.,*
528 2011). For example, using data from a network of continuously recording gravimeters, Carbone *et*
529 *al.,* (2013) calculated the density of the Kilauea lava lake as 950±300 kg m^3, i.e. similar to and
530 potentially less than that of water, suggesting that the magma column within the upper portions of
531 the volcanic edifice is gas-rich. Because density and volatile content are critical controls on magma
532 rheology, identification of a gas-rich magma column and lava lake at Kilauea is crucial to modelling
533 and understanding convection and eruption dynamics (Carbone *et al.,* 2013).
534
535 ***Implications and integration***
536 The advent of data-rich geodetic observations from satellite-remote sensing (e.g., InSAR), in
537 conjunction with spatio-temporal gravity studies, provides unprecedented opportunities to
538 characterise magma plumbing system dynamics and the driving mechanisms behind volcano
539 deformation. At Long Valley caldera, for example, a residual gravity increase of more than 60 μGal
540 between 1982 and 1999 indicates a mass addition at depth (Battaglia *et al.,* 1999). Joint inversion of
541 InSAR and gravity data from Long Valley derives a best fit-source density of 2509 kg m^3 and is
542 indicative of a magmatic intrusion (Fig. 8) (Tizzani *et al.,* 2009). At the deforming Laguna del
543 Maule volcanic centre, Chile, multi-year InSAR and dynamic gravity records demonstrate that
544 uplift and extension above an inflating sill-like reservoir at ~5 km depth promoted migration of
545 hydrothermal fluids along a fault to shallow (1–2 km) depths (Miller *et al.,* 2017). Alternatively,
546 although no ground deformation is observed at Tenerife, Spain, deconvolution of dynamic gravity

547 into a shallow and deep gravity field provides evidence of unrest (Prutkin *et al.,* 2014). The gravity
548 data suggest hybrid processes have generated the unrest, whereby fluids were released and migrated
549 upward along deep-rooted faults from an intrusion at ~9 km beneath the summit of Teide Volcano
550 (Prutkin *et al.,* 2014). Overall, combining ground deformation and gravimetric observations has
551 highlighted complex processes both within magma reservoirs (e.g., mass addition by magma input,
552 density decrease by volatile exsolution, or density increase by crystallisation; Figs 7c-f) and in the
553 surrounding host rock (e.g., migration of magmatic fluids, phase changes in hydrothermal systems).
554 Key to a better understanding of the processes governing these magma plumbing system and
555 volcano deformation dynamics is the integration of gravimetric and geodetic data with other
556 geophysical data (e.g., seismicity or magnetotellurics) and petrological data. Coupled with
557 advanced numerical modelling, such multi-parameter studies promise exciting new insights into the
558 inner workings of sub-volcanic magma plumbing systems (e.g., Currenti *et al.,* 2007; Hickey *et al.,*
559 2016; Currenti *et al.,* 2017; Gottsmann *et al.,* 2017; Miller *et al.,* 2017).
560
561 **2.5. Resolving magma plumbing system structure with electromagnetic methods**
562 ***Techniques***
563 Electromagnetic (EM) methods probe subsurface electrical resistivity or its inverse, i.e. electrical
564 conductivity. Spatial variations in resistivity control the position, strength, and geometry of local
565 electrical eddy currents and the magnetic fields they produce. These electrical eddy currents are
566 induced by time-varying, naturally occurring magnetic fields external to Earth, which forms the
567 basis of the magnetotelluric (MT) technique, or by controlled sources. Monitoring these decaying
568 electrical and magnetic fields with passive MT techniques therefore allows the subsurface resistivity
569 distribution to be inferred. Controlled source methods generally probe only the shallow subsurface,
570 but MT has a greater depth range as it uses longer-period signals to penetrate deeper. The signals
571 propagate diffusively, which means EM methods typically have a lower resolution than seismic
572 techniques. However, melt, magma, and magmatic hydrothermal fluids are generally considerably

573 less resistive than solid rock and can thus easily be detected by EM methods, which are sensitive to
574 conductive materials (e.g., Whaler & Hautot, 2006; Wannamaker *et al.,* 2008; Desissa *et al.,* 2013;
575 Comeau *et al.,* 2015). EM methods, particularly MT, have therefore been used extensively to study
576 magmatic systems in various tectonic settings.

577 MT equipment, data acquisition, and processing is described by Simpson & Bahr (2005) and
578 Ferguson (2012). Measured field variations have very low amplitudes, meaning equipment needs to
579 be positioned and installed carefully to reduce vibrational (e.g., from wind, vegetation, or vehicles)
580 and electrical (e.g., from power lines) noise. If data are recorded synchronously at a second, less
581 noisy site, remote reference methods can be used to improve the data quality (e.g., Gamble *et al.,*
582 1979). One further problem is that small-scale resistivity anomalies in the shallow subsurface
583 generate galvanic (non-inductive) effects that distort MT data. The distortion is identified and
584 corrected for, which may involve using controlled source transient electromagnetic data to ensure
585 complete removal (e.g. Sternberg *et al.,* 1988), at the same time as assessing whether the data can
586 be modelled with a one-, two- or three-dimensional resistivity structure (e.g. Jones, 2012). Failure
587 to remove galvanic distortion can result in models having resistivity features at the wrong depth.
588 For example, there has been controversy as to whether a conductor beneath Vesuvius Volcano, Italy
589 is caused by a deep (~8–10 km depth) magma reservoir (Di Maio *et al.,* 1998) or a shallow brine
590 layer (Manzella *et al.,* 2004). All of these factors can be a significant problem when using MT to
591 study magmatic systems, especially on volcanic islands.

592 The relationship between MT data and subsurface resistivity is strongly non-linear meaning
593 that inversion is fundamentally non-unique and computationally expensive (e.g., Bailey, 1970;
594 Parker, 1980; Weaver, 1994). Most practical algorithms for inverting MT data obtain a unique
595 result by minimising a combination of misfit to the data and a measure of model roughness (e.g.,
596 Constable *et al.,* 1987). This approach poorly delimits how magma is distributed in the subsurface,
597 whether it is in sills, dykes, or larger reservoirs (Johnson et al., 2016). Whilst MT data are sensitive
598 to the top surface of a conductor, its base may not be detected because conductive material reduces

599 the penetration depth of the signal. Sensitivity analysis is used to ascertain the model features
600 required to fit the MT data, which allows a conductor to be confined to a certain depth range and
601 thereby constrains its base (e.g., Desissa *et al.,* 2013). Furthermore, if the resistivity of a conductor
602 can be inferred, its conductance (i.e. a product of thickness and conductivity) can be used to
603 determine its thickness (e.g., Comeau *et al.,* 2016).
604
605 ***Observations***
606 EM induction surveys have been conducted on most major sub-aerial volcanoes and magmatic
607 systems; only a few will be mentioned here to illustrate the type information on magma plumbing
608 systems that has been obtained. MT data have been used to image several low resistivity features in
609 the central Andes, particularly beneath the uplifting (10–15 mm/yr) Volcán Uturuncu, Bolivia (Fig.
610 9a) (Comeau *et al.,* 2015; Comeau *et al.,* 2016). The deepest of these bodies has resistivities of <3
611 Ω m, has a top contact at ~15–20 km depth (i.e. it is shallowest beneath Uturuncu), likely has a
612 thickness of >6 km, and extends E-W for ~170 km (Fig. 9) (Comeau *et al.,* 2015; Comeau *et al.,*
613 2016). This large-scale structure is interpreted to be the Altiplano-Puna magma body (APMB),
614 which has been identified in other geophysical datasets (e.g., Fig. 7a) (e.g., gravimetry, del Potro *et*
615 *al.,* 2013), with its low resistivity attributed to the presence of at least 20% andesitic melt and/or
616 magma. Extending from the top of the APMB towards the surface are several vertical, narrow (<10
617 km wide), low resistivity (<10 Ω m) zones that coincide with areas of seismicity and negative
618 gravity anomalies (Fig. 9). These zones likely reflect a network of dykes and upper crustal magma
619 reservoirs (Jay *et al.,* 2012; del Potro *et al.,* 2013; Comeau *et al.,* 2015; Comeau *et al.,* 2016).
620 Monitoring of magmatic systems can also be undertaken by both time-lapse and continuous
621 EM measurement. For example, MT data collected immediately after the 1977–1978 eruption at
622 Usu volcano, Japan revealed a conductive zone (<100 Ω m) beneath the summit that probably
623 corresponded to intruded magma. By 2000, MT data revealed that this conductive body had become
624 resistive (500–1000 Ω m) as the intrusion cooled, from 800°C to 50°C, and crystallised

(Matsushima *et al.,* 2001). Continuous MT monitoring of Sakurajima volcano, Japan between May 2008 and July 2009 revealed temporal changes in resistivity of ±20%, some of which correlated to periods of surface deformation and were inferred to reflect mixing between groundwater and volatiles exsolved from an underlying magma body (Aizawa *et al.,* 2011). Continuous MT monitoring at La Fournaise, Réunion Island recorded apparent resistivity decreases associated with the large 1998 eruption, which were attributed to the injection of a N-S striking dyke (Wawrzyniak *et al.,* 2017).

Several EM studies have focussed on magma plumbing systems at divergent margins, including mid-ocean ridges and continental rifts. For example, at the fast-spreading East Pacific Rise, a ~10 km wide, sub-vertical conductor, slightly displaced from the ridge axis and connected to a deep, broad conductive zone was interpreted as a channel efficiently transporting melt to the base of the crust (Baba *et al.,* 2006; Key *et al.,* 2013). Imaging of a crustal conductor for the first time beneath a slow-spreading ridge, i.e. the Reykjanes ridge in the Atlantic Ocean, suggests that magma injection into crustal reservoirs is intermittent but rapid (MacGregor *et al.,* 1998; Heinson *et al.,* 2000). Conversely, slow-spreading continental rifting in the Dabbahu magma segment, Afar, Ethiopia appears to be underlain by a large conductor, either at the top of the mantle or straddling the Moho, containing more melt (>300 km^3) than is intruded into the magma plumbing system during a typical rifting episode (Desissa *et al.,* 2013). The volume of this large conductor implies it is a long-lived feature that could source magmatic activity for tens of thousands of years (Desissa *et al.,* 2013).

Implications and integration

It is clear from MT studies of the APMB that other geophysical techniques aid and/or corroborate data interpretation (Fig. 9) (e.g., Comeau *et al.,* 2015; Comeau *et al.,* 2016). Over the last two decades, numerous geophysical studies have been applied to examine magma and melt distribution beneath various portions of the East African Rift, providing an excellent opportunity to test how

651 different techniques and data can be integrated. For example, extensive zones of melt beneath the
652 Afar region in Ethiopia inferred from MT data by Desissa *et al.,* (2013) is supported by: (i) the
653 occurrence of coincident, low P-wave velocity (down to 7.2 km s^{-1}) zones identified using from
654 analysis of seismic Pn waves that propagate along the Moho (Stork *et al.,* 2013); (ii) surface wave
655 studies that reveal lower crustal areas in magmatic domains with low S-wave velocities (~3.2 km s^{-1})
656 (Guidarelli *et al.,* 2011); and (iii) high anisotropic V_P/V_S ratios and low amplitude receiver
657 functions, which are indicative of the presence of melt (Hammond *et al.,* 2011; Hammond, 2014).
658 Similarly, crustal conductors along the northern flanks of the Main Ethiopian Rift, interpreted to
659 represent melt/magma (Whaler & Hautot, 2006; Samrock *et al.,* 2015; Hübert *et al.,* 2018), coincide
660 with locations where receiver functions either have amplitudes too low to interpret or indicate high
661 V_P/V_S values (Dugda *et al.,* 2005; Stuart *et al.,* 2006). Electrical anisotropy can be inferred directly
662 from MT data consistent with a two-dimensional subsurface resistivity distribution (Padilha *et al.,*
663 2006; Hamilton *et al.,* 2006). Large amounts of electrical anisotropy were found in the lower crust
664 beneath Quaternary magmatic segments in Afar, Ethiopia, where there is also significant crustal
665 seismic anisotropy (see Fig. 11 of Ebinger *et al.,* 2017); oriented melt-filled pockets are the
666 probable cause of both.

667 Although EM methods can image subsurface conductors that are interpreted to represent
668 magma bodies or zones of partial melt (i.e. crystal mushes), additional information is required to
669 determine their composition, volume, and/or melt fraction. However, there are several challenges in
670 inverting measured bulk resistivities to recover this information. Two-phase mixing laws predict
671 bulk resistivity is primarily a function of melt resistivity and geometry in the rock matrix when the
672 fluid phase has low resistivity, as in the case of partial melt. Well-connected melt gives a lower bulk
673 resistivity than isolated melt pockets, for the same melt fraction and resistivity (e.g. Hashin &
674 Shtrikman, 1963; Roberts & Tyburczy, 1999; Schmeling, 1986). Whilst resistivities of basaltic and
675 rhyolitic melts have been measured in laboratory experiments (e.g., Laumonier *et al.,* 2015; Guo *et*
676 *al.,* 2016), they are strongly dependent on temperature, pressure, silica, sodium and water content,

677 making extrapolation uncertain. The web-based SIGMELTS tool can, however, be used to predict
678 melt and bulk resistivities for a wide range of compositions and conditions (Pommier & Le Trong,
679 2011). Importantly, petrological and geochemical characterisation of eruptive products can help
680 inform interpretations of associated, subsurface conductors but it is difficult to ascertain either
681 whether their composition reflects the current magma/melt present in the plumbing system or
682 whether melt pockets are interconnected. These large uncertainties in melt resistivity and the
683 requirement to make assumptions about its geometry make direct inference of melt fraction
684 difficult. Nonetheless, information from laboratory studies, petrology, and geochemistry aids
685 interpreting resistivity anomalies in magmatic regions (see review by Pommier, 2014).
686
687 **2.6. Imaging ancient magma plumbing systems in seismic reflection data**
688 ***Techniques***
689 Over the last two decades, major advances have been made in imaging deep crustal melt beneath
690 active volcanic terrains using P- and S-wave tomographic data (e.g., Yellowstone, Husen *et al.,*
691 2004; Mt. St. Helens, Lees, 2007; Hawaii, Okubo *et al.,* 1997). These data image deep (>7 km),
692 often laterally extensive (up to 20 km), sill-like magma reservoirs (e.g., Paulatto *et al.,* 2012).
693 However, like many geophysical and geodetic techniques applied to study active magma plumbing
694 systems, these data typically lack the spatial resolution to resolve the detailed geometry of pathways
695 transporting magma to the Earth's surface. Active source seismic reflection data, which have a
696 spatial resolution of metres-to-decametres down to depths of ~5 km, can provide unprecedented
697 images of and insights into the geometry and dynamics of shallow-level, crystallised, magma
698 plumbing systems (e.g., Fig. 10) (e.g., Planke *et al.*, 2000; Smallwood & Maresh, 2002; Thomson &
699 Hutton, 2004; Cartwright & Hansen, 2006; Jackson *et al.*, 2013; Magee *et al.*, 2016; Schofield *et*
700 *al.*, 2017). Whilst seismic reflection data are traditionally used to find and assist in the production of
701 hydrocarbons in sedimentary basins (Cartwright & Huuse, 2005), we here discuss and support its
702 application to volcanological problems.

703 Acquiring active source seismic reflection data involves firing acoustic energy (i.e. seismic
704 waves) into the subsurface and measuring the surface arrival times (i.e. the travel-time) of reflected
705 energy. Processing of these arrival time data allows reconstruction of the location and geometry of
706 the geological interfaces from which acoustic energy was reflected. Mafic intrusive igneous rocks
707 are generally well-imaged in seismic reflection data because they typically have greater densities
708 (>2.5 g/cm^3) and acoustic velocities (i.e. >4000 m s) than encasing sedimentary strata; these
709 differences result in a high acoustic impedance contrast, causing more seismic energy to be
710 reflected back to the surface compared to low acoustic impedance boundaries (Smallwood &
711 Maresh, 2002; Brown, 2004). In contrast, silicic igneous rocks have similar acoustic properties to
712 encasing sedimentary strata, meaning that felsic intrusions are rarely imaged in seismic reflection
713 data (Mark *et al.,* 2017; Rabbel *et al.,* 2018). Furthermore, because reflection seismology relies on
714 the return of acoustic energy to the surface, seismic reflection data favourably image mafic, sub-
715 horizontal-to-moderately inclined intrusions (e.g., sills, inclined sheets, and laccoliths; Smallwood
716 & Maresh, 2002; Jackson *et al.,* 2013; Magee *et al.,* 2016). Sub-vertical dykes reflect only a limited
717 amount of acoustic energy back to the surface and are thus typically poorly imaged in seismic
718 reflection data (e.g., Smallwood & Maresh, 2002; Planke *et al.,* 2005; Thomson, 2007; Wall *et al.,*
719 2010; Eide *et al.,* 2017a; Phillips *et al.,* 2017).
720
721 ***Observations***
722 Sills and inclined sheets are commonly observed in seismic reflection data as laterally
723 discontinuous, high-amplitude reflections, which may cross-cut the host rock strata (Fig. 10) (e.g.,
724 Symonds *et al.*, 1998, Smallwood & Maresh, 2002; Planke *et al.*, 2005, Magee *et al.*, 2015). Many
725 of the sills and inclined sheets imaged in seismic reflection data are, however, expressed as tuned
726 reflection packages, whereby discrete reflections from the top and base contacts interfere on their
727 return to the surface and cannot be distinguished (e.g., Figs 10 and 11a) (e.g., Smallwood &
728 Maresh, 2002; Peron-Pinvidic *et al.,* 2010; Magee et al., 2015; Eide *et al.,* 2017a; Rabbel *et al.,*

729 2018). It is therefore difficult to assess either intrusion thicknesses, or to detect whether imaged sills
730 are composite bodies made of numerous, stacked, thin sheets. Either way, subtle vertical offsets and
731 corresponding amplitude variations of sill reflections can often be mapped, defining linear
732 structures that radiate out from either the central, deepest portions of sills or areas where underlying
733 intrusions intersect the sill (e.g., Schofield *et al.,* 2012a; Magee *et al.,* 2014; Magee *et al.,* 2016).
734 These structures are interpreted to relate to magma flow indicators such as intrusive steps, broken
735 bridges, and magma fingers (e.g., Schofield *et al.,* 2010; Schofield *et al.,* 2012b; Magee *et al.,*
736 2018).

737 A recurring observation from seismic reflection-based studies of extinct and buried intrusive
738 systems is that complexes of interconnected sills and inclined sheets, which may cover $>3 \times 10^6$
739 km^2, can dominate magma plumbing systems (e.g., Fig. 10b) (e.g., Svensen *et al.*, 2012, Magee *et*
740 *al.*, 2016). Importantly, where buried volcanic edifices are imaged in seismic reflection data, they
741 rarely appear to be underlain by 'magma chambers' (i.e. a spheroidal or ellipsoidal body of now-
742 crystallised magma). Instead, these imaged volcanoes commonly appear laterally offset from
743 genetically related sills and/or laccoliths that are inferred to represent their feeder reservoirs (e.g.,
744 Fig. 10b) (Magee *et al.*, 2013a; McLean *et al.*, 2017). The geometry, location, and connectivity of
745 these intrusions, which can represent magma storage sites and conduits to the surface, are often
746 heavily influenced by both the host rock structure and lithology (see review by Magee *et al.*, 2016).
747 For example, magma may flow along pronounced discontinuities (e.g., bedding) or within specific
748 stratigraphic units (e.g., coal) for considerable distances, occasionally climbing to higher
749 stratigraphic levels by instigating deformation of the host rock or by exploiting pre-existing faults
750 (e.g., Jackson *et al.*, 2013; Magee *et al.*, 2016; Schofield *et al.*, 2017; Eide *et al.,* 2017b). It is clear
751 from seismic reflection data that shallow-level tabular intrusions are commonly accommodated by
752 roof uplift to form a flat-topped or dome-shaped forced fold (e.g., Figs 11a and b) (e.g., Trude *et al.,*
753 2003; Hansen & Cartwright, 2006; Jackson *et al.,* 2013; Magee *et al.,* 2013b). Moreover, if the age
754 of reflections onlapping onto these intrusion-induced forced folds can be ascertained, the timing and

to some extent the duration of magmatic activity can be determined (e.g., Trude *et al.,* 2003; Hansen & Cartwright, 2006; Magee *et al.,* 2014; Reeves *et al.,* 2018). Although most seismic-based studies examine intrusions within sedimentary basins, saucer-shaped sills and laterally extensive sill-complexes emplaced into crystalline basement rock are also imaged (e.g., Ivanic *et al.,* 2013; McBride *et al.,* 2018). Lastly, seismic reflection data can also be used to image the internal structure of layered ultramafic-mafic intrusions (e.g., the Bushveld Layered Intrusion, Malehmir *et al.*, 2012) and, in some instances, identify dykes (e.g., Fig. 11c) (e.g., Wall *et al.,* 2010; Abdelmalak *et al.,* 2015; Bosworth *et al.,* 2015; Phillips *et al.,* 2017).

Implications and integration

Despite being limited in terms of their spatial resolution (typically a few tens of metres) and ability to image steeply dipping features (i.e. dykes), they provide unprecedented snapshots into the final 3D structure of magma plumbing systems. Beyond quantifying the structure and connectivity of magma plumbing systems, seismic-based studies have shown that: (i) magma flow patterns mapped across entire sill-complexes indicate they can transport melt from source to surface over great lateral (>100's km) and vertical distances (10's km), potentially without significant input from dykes (Fig. 10a) (e.g., Thomson & Hutton, 2004; Cartwright & Hansen, 2006; Magee *et al.*, 2014; Magee *et al.*, 2016; Schofield *et al.*, 2017); and (ii) a variety of elastic and inelastic mechanisms can accommodate host rock deformation during magma emplacement, meaning that the location and size of ground deformation does not necessarily equal that of the forcing intrusion (e.g., Jackson *et al.*, 2013, Magee *et al.*, 2013b). Importantly, observations from seismic reflection data highlight that the lateral dimension should be considered when modelling the transit of magma in the crust, posing problems for the widely held and simple assumption that magma simply travels vertically from melt source to eruption site.

Seismic-based studies have also shown that direct comparison to active deformation structures can be informative. For example, through comparing mapped lava flows and structures

781 associated with the Alu dome to similar features observed in seismic reflection data (see section
782 2.6), Magee *et al.,* (2017) concluded that the shallow-level sill likely has a saucer-shaped, as
783 opposed to the sill-like tabular morphology inferred from an episode of deformation measured using
784 InSAR (Figs 3c and d). Despite its benefits, it is important to remember that seismic reflection data
785 typically reveal only the final geometry of the magma plumbing system. There thus remains a
786 challenge in using these data to understand areas where deformation captures potentially transient,
787 active processes, rather than structures resulting from (multiple) periods of intrusion and cooling
788 (Reeves *et al.,* 2018). One potential and exciting way forward is the development of Virtual
789 Reflection Seismic Profiling, by which microseismicity at active volcanoes may be used to image
790 magma reservoirs and subsurface structure in 4D (Kim *et al.,* 2017). Although challenges exist in
791 dataset integration, the imaging power afforded by modern seismic reflection data thus presents a
792 unique opportunity to further unite field-, petrological-, geochemical-, and other geophysical-based
793 analyses within more realistic structural frameworks (e.g., Figs 3, 11a and b). In our view, however,
794 seismic reflection data are under-utilized in igneous research, remaining an unfamiliar technique to
795 many Earth Scientists in the volcanic and magmatic community.
796
797 **2.7. Rock magnetism**
798 ***Technique***
799 Whilst seismic reflection data provide unique 3D images of ancient magma plumbing systems,
800 which can be used to infer magma flow patterns across entire intrusion networks, we commonly
801 lack sufficient data (e.g., boreholes) to test seismic-based hypotheses. It is therefore critical to
802 compare seismic interpretations to field analogues where magma flow patterns, emplacement
803 mechanics, and intrusion evolution can be investigated via other techniques. In this section, we
804 examine how rock magnetic analyses can be used to systematically study magnetic mineralogy and
805 petrofabrics, thereby illuminating the structure and history of igneous intrusions.

There are two principal types of rock magnetic study; magnetic remanence and magnetic susceptibility, where the total magnetisation (M) of a rock is the sum of the magnetic remanence (M_{rem}) and the induced magnetisation (M_{ind}), which is a product of the susceptibility (K) and applied field strength (H) (Dunlop & Özdemir, 2001). Remanence carries a geological record of the various magnetisations acquired over time and is central to palaeomagnetic studies. However, we focus on magnetic fabric analysis, which relies on measurements of the anisotropy of magnetic susceptibility (AMS). The AMS signal of a rock carries information from all constituent grains. Although mineral phases that have a paramagnetic behaviour (i.e. they are weakly attracted to externally applied magnetic fields) volumetrically dominate most igneous rocks (e.g., olivine, clinopyroxene, biotite), ferromagnetic mineral phases (e.g., titanomagnetite) are highly susceptible to magnetization and therefore tend to dominate K (e.g., Dunlop & Özdemir, 2001; Biedermann *et al.,* 2014). Magnetic fabrics therefore typically reflect the preferential orientation of crystallographic axes (i.e. crystalline anisotropy), the shape-preferred orientation of individual crystals (i.e. shape anisotropy), and/or the alignment of closely spaced crystals (i.e. distribution anisotropy) belonging to Fe-bearing silicate and oxide phases (e.g., Voight & Kinoshita, 1907; Graham, 1954; Hrouda, 1982; Tarling & Hrouda, 1993; Dunlop & Özdemir, 2001). The principal axes of the magnetic fabrics measured by AMS can thus be related to the orientation, shape, and distribution of individual grains (i.e. the petrofabric) (e.g., Fig. 12a).

Regardless of whether mineral phases crystallise early or late, whereby their orientation and distribution typically mimics the earlier silicate framework, it is expected that the initial petrofabric developed in intrusive rocks will likely be sensitive to alignment of crystals during primary magma flow. However, it is also critical to recognise that later magmatic processes (e.g., convection and melt extraction) and syn- or post-emplacement tectonic deformation can modify or overprint primary magma flow fabrics during intrusion, solidification (i.e. mush development), or sub-solidus conditions (e.g., Borradaile & Henry, 1997; Bouchez, 1997; O'Driscoll *et al.,* 2015; Kavanagh *et al.,* 2018). Whilst anisotropy of magnetic susceptibility (AMS) can thus rapidly and accurately

detect weak or subtle mineral alignments within igneous intrusions, which may be attributable to magmatic and/or tectonic processes, evaluating the origin and evolution of petrofabric development requires additional information (e.g., Borradaile & Henry, 1997; Bouchez, 1997). For example, shape-preferred orientation analyses and comparison to visible flow indicators (e.g., intrusive steps and bridge structures) allow magma flow axes and directions that have been inferred from magnetic fabrics to be verified (e.g., Launeau & Cruden, 1998; Callot *et al.,* 2001; Magee *et al.,* 2012a). For a useful précis of AMS-related magnetic theory in igneous rocks, the reader is referred to early works by Balsey & Buddington (1960) and Khan (1962), and more recent summaries provided by Martín-Hernández *et al.,* (2004), O'Driscoll *et al.,* (2008), and O'Driscoll *et al.,* (2015).

The principle behind AMS relies on the measurement of the bulk susceptibility (K_m) of a single sample in different orientations to determine the susceptibility anisotropy tensor, which relates the induced magnetisation (M_{ind}) to the applied field (H) in three dimensions (Tarling & Hrouda, 1993). The orientation and magnitude of the eigenvectors and eigenvalues of this tensor define an ellipsoid with three principal axes; the long axis of the ellipsoid, K_1, defines the magnetic lineation and the short axis, K_3, defines the normal (i.e. the pole) to the magnetic foliation plane (K_1–K_2; Fig. 12a) (Stacy *et al.,* 1960; Khan, 1962; Tarling & Hrouda, 1993). In order to interpret magnetic fabrics, it is important to determine the mineralogy of the phases carrying the magnetic signal because the composition, grainsize, and distribution of magnetically dominant minerals (e.g., titanomagnetite) can control fabric orientation (e.g., Hargreaves *et al.,* 1991; Stephenson, 1994; Dunlop & Özdemir, 2001). In addition to primary crystallographic and textural controls on magnetic fabrics, subsequent oxidation of remaining melt and secondary hydrothermal alteration can affect the magnetic mineralogy and, thereby, the AMS signal (e.g., Trindade *et al.,* 2001; Stevenson *et al.,* 2007a). A variety of rock magnetic experiments are thus required to determine the magnetic mineralogy. The most widely used method involves measuring susceptibility, and thereby behaviour of magnetic materials, at varying temperatures ranging from -200°C to 700°C (i.e. thermomagnetic analysis *sensu* Orlický, 1990; Hrouda *et al.,* 1997). For example, paramagnetic

858 materials (e.g., biotite) follow the Curie-Weiss law, whereby their susceptibility drops
859 hyperbolically with increasing temperature. In contrast, the thermomagnetic curve of ferromagnetic
860 materials (e.g., titanomagnetite) displays little change in susceptibility with temperature, apart from
861 when characteristic crystallographic transitions occur (e.g., the Curie point for pure magnetite at
862 ~580°C, Petrovský & Kapička, 2006) temperature. To determine the grainsize of ferromagnetic
863 fraction in the magnetic susceptibility signal, the hysteretic property of the magnetisation is
864 important (Dunlop, 2002). Other rock magnetic experiments (e.g., anisotropy of anhysteretic
865 remanent magnetism (AARM) can be conducted to further isolate the relative importance of
866 different paramagnetic and ferromagnetic phases (e.g., McCabe *et al.,* 1985; Richter & van der
867 Pluijm, 1994; Kelso *et al.,* 2002).
868
869 ***Observations***
870 Having established the magnetic mineralogy, AMS fabrics can be interpreted. Even in weakly
871 anisotropic igneous rocks (i.e. visually isotropic), particularly sheet intrusions, it is now accepted
872 that the magnetic lineation and foliation can provide information on magma migration (e.g., flow
873 direction) or regional and local strain (e.g., Hrouda, 1982; Knight & Walker, 1988; Rochette *et al.,*
874 1992; Bouchez, 1997; Tauxe *et al.,* 1998; Callot et al., 2001; Féménias *et al.,* 2004; Magee *et al.,*
875 2012a). For example, comparisons to other indicators of magma flow (e.g., intrusive steps and
876 visible mineral alignments) in sheet intrusions have shown that magnetic lineations commonly
877 parallel the magma flow (e.g., Knight & Walker, 1988; Cruden & Launeau, 1994; Callot *et al.,*
878 2001; Magee *et al.,* 2012a), whilst imbrication of elongate crystals induced by simple shear at
879 intrusion margins define the sense of magma flow (Fig. 12b) (e.g., Knight & Walker, 1988;
880 Hargraves *et al.,* 1991; Stephenson, 1994; Geoffroy *et al.,* 2002; Féménias *et al.,* 2004).
881 Alternatively, contact-parallel magnetic fabrics generated during the formation and inflation of
882 magma lobes can be used to determine flow and emplacement dynamics, even if other evidence for
883 the presence of magma lobes is lacking (e.g., Fig. 12c) (Cruden *et al.,* 1999; Stevenson *et al.,*

884 2007a; Magee *et al.,* 2012b). Identifying changes in fabric orientation within or between individual
885 sheet intrusions is also important because these variations suggest that deformation, imparted by
886 either the emplacement of adjacent magma bodies or tectonic processes, did not significantly
887 modify magma emplacement fabrics (e.g., Clemente *et al.,* 2007).
888 Post solidification textural modification and the possibility of overlap in tectonic and
889 magmatic strain fields during protracted emplacement is a particular complication when studying
890 granitoid and gabbroic plutons (e.g., Mamtani *et al.,* 2013; O'Driscoll *et al.,* 2015; Cheadle *et al.,*
891 2017). In fact, most early studies of granitoid emplacement using AMS, in conjunction with many
892 other structural analysis tools, concluded that tectonic strain was the main source of subtle fabrics
893 (e.g., Brun *et al.,* 1990; Bouchez, 1997; de Saint-Blanquat & Tikoff 1997; Neves *et al.,* 2003;
894 Mamtani *et al.,* 2005). Although primary magma flow fabrics in granitic and gabbroic plutons may
895 thus be overprinted, the magnetic fabrics characterised by AMS can still provide fundamental
896 insights into emplacement mechanics (e.g., Stevenson *et al.,* 2007a; Petronis *et al.,* 2012) and
897 magma/mush evolution (e.g., formation of layering; O'Driscoll *et al.,* 2015).
898
899 ***Implications and integration***
900 Overall, AMS has provided vital magma flow and evolution information that has helped to
901 understand mafic and silicic magma plumbing systems (e.g., Knight & Walker, 1988; Ernst &
902 Baragar, 1992; Glen *et al.,* 1997; Aubourg *et al.,* 2008; Petronis *et al.,* 2013; Petronis *et al.,* 2015).
903 Critical insights emanating from these AMS studies have revealed that: (i) flow trajectories
904 predicted by classic emplacement models (e.g., for ring dykes and cone sheets) are not always
905 consistent with measured AMS fabrics and supporting data, which thereby call into question the
906 application of such models (e.g., Stevenson *et al.,* 2007b; Magee *et al.,* 2012a); (ii) lateral magma
907 flow is recorded in many shallow, planar intrusions associated with volcanic magma plumbing
908 systems (e.g., Ernst & Baragar, 1992; Cruden & Laneau, 1994; Cruden *et al.,* 1999; Herrero-
909 Bervera *et al.,* 2001; Magee *et al.,* 2012a; Petronis *et al.,* 2013; Petronis *et al.,* 2015); and (iii)

plutons, particularly those with a granitic composition, commonly consist of incrementally emplaced magma pulses that often develop lobate geometries (e.g., Fig. 12c) (*e.g.,* Stevenson et al., 2007a). Analysing AMS fabrics from layered mafic-ultramafic intrusions can also provide evidence for magma reservoir processes, including crystal settling, or post-cumulus modification of crystal mushes (O'Driscoll *et al.,* 2008; O'Driscoll *et al.,* 2015). Importantly, AMS and related analyses provide robust, testable, and repeatable methods to constrain subtle shape and crystallographic orientations of crystals in igneous rocks. Rock magnetic instrumentation technology continues to advance with better automation of measurement protocols, sensitivity of measurements, and a greater ability to unravel contributors to the AMS signal. The direction and scope of these developments are improving the holistic integration of AMS with other structural, microstructural, geophysical, petrological and geochemical techniques, promising to advance our understanding of magmatism and crustal evolution.

3. Future advances

Our understanding of magma plumbing system structure and evolution has been significantly enhanced by the geophysical techniques described above. We have demonstrated that there is scope for advancement within individual methodologies and through the integration of different techniques, particularly involving the synthesis of geophysical, petrological, and geochemical data. In this section, we discuss two new techniques that will potentially revolutionize our understanding of magma plumbing systems. We also briefly discuss how integration of geophysical data with numerical modelling can enhance our knowledge of reservoir construction and evolution.

3.1. Full-Waveform Inversion

Technique

We have demonstrated that seismic reflection data can provide unique insight into the 3D structure of magma plumbing systems (e.g., see review by Magee *et al.,* 2016). In addition to using seismic

reflection data to image the subsurface, we can also invert the measured travel-times of reflected acoustic energy to model subsurface P-wave velocities. Full-waveform inversion (FWI) is a rapidly developing technology using active source seismic data to generate models that reproduce both the travel-times and full waveform of the arriving wavefield, thereby matching observed seismic data (Tarantola, 1984). Because FWI considers the full wavefield, as opposed to conventional techniques that only model travel-times, it is a technique capable of recovering high-resolution models of subsurface P-wave velocities and other physical properties (Warner *et al.,* 2013; Routh *et al.,* 2017). The FWI technique begins with a best-guess starting velocity model for the subsurface geology, which is then iteratively updated using a local linearized inversion until the observed seismic data is matched (Virieux & Operto, 2009). FWI is much more computationally expensive than travel-time tomography, as a full-physics implementation of the wave equation is required to generate the predicted seismic data at all energy source and receiver locations for each iteration (Routh *et al.,* 2017). FWI, however, has the advantage of being able to resolve much finer-scale structure than conventional techniques.

Observations

To date, 3D FWI has principally been applied within the petroleum sector to obtain high-resolution velocity models that can be used to improve depth-migrated (i.e. travel-time is converted to depth in metres) reflection images of petroleum reservoirs and their overburden (Sirgue *et al.,* 2010; Vigh *et al.,* 2010; Warner *et al.,* 2013; Kapoor *et al.,* 2013; Routh *et al.,* 2017). FWI can also produce interpretable, quantitative models of physical properties of rocks in the subsurface that can be related directly to compaction, permeability, and overpressure as measured in subsurface boreholes (Lazaratos *et al.,* 2011; Mancini *et al.,* 2015). Of relevance here is that mafic intrusions, which appear as high-amplitude reflections in seismic reflection data (Figs 10 and 11a), are recovered as high-velocity features in FWI velocity models (Fig. 13) (Mancini *et al.,* 2015; Kalincheva *et al.,* 2017). For example, successful application of 3D FWI to a marine ocean bottom seismometer

962 dataset acquired across the Endeavour segment of the Juan de Fuca Ridge led to generation of a
963 velocity model that had a resolution up to four times greater than travel-time tomography (Morgan
964 *et al.,* 2016). Within this new, high-resolution velocity model, several velocity anomalies were
965 identified and interpreted to indicate localized magma recharge of the axial reservoir, induced
966 seismogenic cracking, and increased permeability (Arnoux *et al.,* 2017).
967
968 ***Implications and integration***
969 Active magma plumbing systems comprise a complex network of interconnected conduits and
970 reservoirs with variable geometries and sizes, which likely contain magmatic vapour-rich, liquid-
971 rich, and mush-zones (Christopher *et al.,* 2015). These intrusions will all be associated with reduced
972 P-wave velocities, which could be resolved in high-resolution, 3D FWI datasets as supported by
973 successes in the fine-scale imaging of: (i) low-velocity gas clouds (Warner *et al.,* 2013); (ii) axial
974 reservoirs at an oceanic spreading centre (Arnoux *et al.,* 2017); (iii) relatively narrow, low-velocity
975 fault zones within an antiform (Morgan *et al.,* 2013); and (iv) a subduction zone using 2D FWI
976 (Kamei *et al.,* 2012). A suite of synthetic tests has been performed to investigate whether 3D FWI
977 could be applied to better understand magma plumbing systems (Morgan *et al.,* 2013). These tests
978 indicate that it is possible to recover high-resolution models of P-wave velocity beneath volcanoes,
979 which can then be used to better determine where magma/mush is stored beneath the surface. In
980 particular, these synthetic tests suggest that FWI could be used to: (i) distinguish between
981 continuous zones of mush and individual magma reservoirs; (ii) image sills and conduits of magma
982 and/or fluids that are a few 10s metres across (Fig. 13); and (iii) image the deeper (lower-crustal)
983 part of the magma system. We therefore consider that 3D FWI affords an unprecedented
984 opportunity to obtain high-resolution images of actual magma plumbing systems beneath active
985 volcanoes. To this end, the ongoing PROTEUS (Plumbing Reservoirs Of The Earth Under
986 Santorini) experiment was specifically designed to use 3D FWI to investigate the Santorini magma
987 plumbing system (Hooft *et al.,* 2017).

3.2. Unmanned Aerial Vehicle photogrammetry

Technique

Despite major advances in satellite-based remote sensing systems and aeromagnetic surveys, very high-resolution (i.e., mm–cm scale ground sampling distance) imagery of dykes and other igneous intrusions has been limited to low altitude aerial photography. This in turn has created a critical scale gap in intrusion studies, which range from <1 mm at thin section scale to the metres to 100's of metres scale provided by outcrop analysis, conventional remote sensing, and geophysical data. Fortunately, the emerging capability of unmanned aerial vehicle (UAV) photogrammetry fills this gap (e.g., Eisenbeiss, 2009; Westoby *et al.,* 2012; Bemis *et al.,* 2015; Eide *et al.,* 2017b). It is also noteworthy that several studies have demonstrated that digital photogrammetry can deliver high quality datasets with accuracies similar to more established laser scanning techniques (e.g., Leberl *et al.,* 2010; Hodgetts, 2013; Thiele *et al.,* 2015).

The basic setup required to carry out UAV (or drone) photogrammetry is commercially available and relatively inexpensive, comprising a fixed wing or rotary wing UAV, a digital camera, and access to a suitable digital photogrammetry software package (e.g., Agisoft Photoscan Pro, Pix4Dmapper Pro, VisualSFM). UAV photogrammetry combines a simple and cost-effective method to acquire geospatially referenced, overlapping digital aerial images, from which structure-from-motion algorithms can generate spatial 3D datasets (Bemis *et al.,* 2014; Vollgger & Cruden, 2016). Such an approach can be used for high spatial resolution mapping of all types of well-exposed igneous intrusions. The resulting data greatly enhance the effectiveness of traditional field mapping, particularly the characterisation of contact relationships and internal and external structure (e.g., fractures, fabrics, and phase distributions) of intrusive rocks, complementing AMS and petrological analyses.

Observations

Aa photogrammetric workflow was applied to examine a swarm of 5 cm to 1 m wide Palaeogene dolerite and dacite dykes exposed on coastal outcrops at Bingie Bingie Point, SE Australia (Fig. 14). The orthophotograph of the entire wave-cut platform shows the distribution of the Palaeogene dolerite and dacite dykes and their Devonian host rock lithologies, including a prominent moderately NE-dipping aplite dyke (Fig. 14a). Linear ENE-WSW linear terrain features pick out the traces of dyke-parallel joints (Fig. 14a). The Palaeogene dykes trend 063° parallel to a major set of joints in the country rock that likely formed contemporaneously with syn-dyking extension (Fig. 14b). Subsidiary joint sets trend NNW-SSE, sub-perpendicular to the Palaeogene dykes, N-S and E-W (Fig. 14b). The Palaeogene dykes display considerable structural complexity such as bridge structures, intrusive steps and apophyses (Fig. 14c). Where present, the steps mostly occur where dykes cross country rock contacts (e.g., the aplite-tonalite contact in the NE; Fig. 14c).

Implications and integration

Data such as the orthophotograph collected at Bingie Bingie Point indicate that high-resolution structural and lithological mapping and measurement can be carried out much more rapidly than by traditional survey methods (e.g., plane table or grid mapping). However, the use of conventional RGB cameras restricts the resulting image data to reflected visible light. Future applications will include the deployment of multispectral and hyperspectral sensors (infrared to short wave infrared to thermal infrared) as well as potential field geophysical or geodetic instruments (e.g., Sparks, 2012). A further challenge for UAV applications in many countries concerns the regulatory framework around the use of drones for research. The global trend is moving to require non-recreational UAV operators to have remotely piloted aircraft licences and for the associated organisation to be certified for UAV operations. Innovations in sensor types and design, attachment of geophysical instruments, machine learning, and integration with complementary techniques such as AMS will open up new avenues for UAV applications in the study of magma plumbing systems.

3.4. Numerical modelling of magma reservoir processes constrained by geophysical data

Geophysical imaging of both active and ancient magma plumbing systems is delivering new insights into the 3D geometry of reservoirs, the timing and rates of melt and magma transport, the pathways followed by magmas as they ascend through the crust, and typical stored melt fractions in mushes. These data can be used to constrain and calibrate numerical models of reservoir processes. Numerical models are used ubiquitously to understand and predict the behaviour of other subsurface crustal reservoirs, such as hydrocarbon reservoirs, groundwater resources, and targets for geological CO_2 storage (e.g., Chen *et al.,* 2003; Class *et al.,* 2009; Dean & Chen, 2011). However, there has been relatively little focus to date on developing numerical models for magma/mush reservoirs. Yet such models can integrate across different data sources and types, provide quantitative estimates of rates, volumes and timescales, and provide a framework for data interpretation. For example, numerical modelling of heat transfer within the plumbing system at Okmok Volcano in Alaska, which was informed by analytical models of geodetic data and estimated magma compositions of erupted material, allowed estimation of the role magma injection, crystallisation, and degassing processes had on volume changes over time (Caricchi *et al.,* 2014). Numerical thermal modelling has also helped interpret seismic data from the Soufrière Hills Volcano, Montserrat, suggesting higher melt fraction in the underlying magma reservoir than was inferred from seismic data alone (Paulatto *et al.,* 2012). More recent numerical models focus on crystal mushes, evaluating melt transport and reaction at low melt fractions, and these show that temperature and melt fraction in mushes can be decoupled; i.e. maximum temperature occurs close to the centre of the reservoir but maximum melt fraction occurs close to the top (Solano *et al.,* 2014). This decoupling impacts how seismic velocities and electrical conductivities will be modified within the mush (Solano *et al.,* 2014). Other numerical models show the important role played by exsolution, crystallisation, and the viscoelastic response of the crust in driving magma mobilisation in and eruption from shallow reservoirs (e.g., Degruyter & Huber, 2014; Parmigiani *et al.,* 2016), as well as providing insights into the mixing mechanisms of melt and crystals in mushes

(Bergantz *et al.,* 2015). However, most models to date have a lower dimensionality (zero dimension box models, or one/two dimensions) and capture only a small subset of the key physical and chemical processes that are likely to occur in crustal magma reservoirs or crystal mushes. Moreover, few studies have integrated modelling with geophysical data (cf. Gutierez *et al.,* 2013). This is in marked contrast to the 3D modelling routinely undertaken of other crustal reservoirs (e.g., hydrocarbon reservoirs), which is commonly integrated with and delimited by geophysical data. There is thus significant scope for improved, and integrated, numerical modelling of crustal magma reservoirs.

4. Conclusions

Determining the structure of magma plumbing systems is critical to understanding where melt and magma is stored in the crust, which can influence the location of volcanic eruptions and economic ore deposits, providing an important framework for interpreting the physical and chemical evolution of magma from petrological and geochemical datasets. Geophysical techniques have revealed unique insights into the architecture of active and ancient magma plumbing systems, which when integrated with traditional structural, petrological and geochemical results has yielded exciting advances in our understanding of magmatic processes. However, divisions between communities applying these methodologies still exist, contributing to diverging views on the nature of magma plumbing systems. To help promote collaboration, we have reviewed a range of geophysical techniques and discussed how they could be integrated with structural, petrological and geochemical datasets to answer outstanding questions in the volcanological community. In particular, we demonstrate how a range geophysical techniques can be applied to track melt migration in near real-time, map entire intrusion networks in 3D, examine magma emplacement mechanics, and understand the evolution of crystal mushes. For example, Interferometric Synthetic Aperture Radar (InSAR) allows measurement of the development of active magmatic systems by successive intrusion, the vertical and lateral movements of magma, and the relationship between

magma plumbing system dynamics and eruption. Seismicity beneath volcanoes can, when the magma interacts dynamically with the host rock, illuminate in high-resolution the time and spatial scales of the motion of magma and hydrothermal fluids. Seismic imaging of magma plumbing systems allows the spatial distribution of melt and magma to be determined whilst the inclusion of anisotropy within seismic techniques even allows sub-seismic wavelength features to be identified. Gravimetry can characterise the distribution and redistribution of mass (e.g., magma) in the subsurface over high spatial and temporal resolutions, helping to reveal the structure and composition of magma plumbing systems and the source(s) of volcano deformation. Electromagnetic methods, particularly magnetotellurics, can identify fluids within magmatic systems (e.g., melt, magma, and hydrothermal fluids). Seismic reflection data provide unprecedented 3D images of ancient magma plumbing systems and has revealed that laterally extensive, interconnected networks of sills and inclined sheets can play a pivotal role in transporting magma through the crust to eruption sites potentially located >100 km away from the melt source. Rock magnetics can provide fabric data pertaining to magma flow, deformation or crystallisation. All these methodologies discussed have provided unique insights into the structure of igneous intrusions and, through integration with petrological and geochemical datasets, are beginning to help unravel the entire evolution of magma plumbing systems. In addition to the ongoing application and advancement of these geophysical techniques, emerging methodologies look set to radically improve our understanding of magma plumbing systems. For example, full-waveform inversion can image and characterise physical properties across plumbing systems at an unprecedented resolution, whereas unmanned aerial vehicle photogrammetry provides a tool for high spatial resolution of outcrop scale intrusions that bridges the scale gap between seismic reflection data and traditional mapping of magma plumbing systems. The geophysical techniques discussed also provide critical constraints on input parameters for numerical modelling. Overall, we consider that the future of magma plumbing system studies will benefit greatly from the synthesis of geophysics and more traditional petrological and geochemical approaches.

5. Acknowledgements

We would like to thank Marian Holness for inviting us to put together this review article and for editorial handling. We are very grateful to Juliet Biggs, Martyn Unsworth, John Bartley, and Magnús Gudmundsson for their extensive and constructive reviews. CM is funded by an Imperial College Research Fellowship at Imperial College London. SKE is funded by an Early Career Fellowship from the Leverhulme Trust. KAW is funded by grant NE/L013932/1.

6. References

Abdelmalak, M. M., Andersen, T. B., Planke, S., Faleide, J. I., Corfu, F., Tegner, C., Shephard, G. E., Zastrozhnov, D., Myklebust, R. (2015). The ocean-continent transition in the mid-Norwegian margin: Insight from seismic data and an onshore Caledonian field analogue. *Geology* **43**, 1011-1014.

Aizawa, K., Kandam, W., Ogawa, Y., Iguchi, M., Yokoo, A., Yakiwara, H., Sugano, T. (2011). Temporal changes in electrical resistivity at Sakurajima volcano from continuous magnetotelluric observations. *Journal of Volcanology and Geothermal Research* **199**, 165-175.

Annen, C. (2011). Implications of incremental emplacement of magma bodies for magma differentiation, thermal aureole dimensions and plutonism–volcanism relationships. *Tectonophysics* **500**, 3-10.

Annen, C., Blundy, J. D., Sparks, R. S. J. (2006). The genesis of intermediate and silicic magmas in deep crustal hot zones. *Journal of Petrology* **47**, 505-539.

Annen, C., Blundy, J. D., Leuthold, J., Sparks, R. S. J. (2015). Construction and evolution of igneous bodies: Towards an integrated perspective of crustal magmatism. *Lithos* **230**, 206-221.

Arnoux G. M., Toomey, D., Hooft, E., Wilcock, W., Morgan, J., Warner, M., VanderBeek, B. (2017). Seismic evidence that black smoker heat flux is rate-limited by crustal permeability. *Geophysical Research Letters* **44**, 1687-1695.

1144 Aubourg, C., Tshoso, G., le Gall, B., Bertrand, H., Tiercelin, J. -J., Kampunzu, A. B., Dyment, J.,
1145 Modisi, M. (2008). Magma flow revealed by magnetic fabric in the Okavango giant dyke swarm,
1146 Karoo igneous province, northern Botswana. *Journal of Volcanology and Geothermal Research*
1147 **170**, 247-261.
1148 Baba, K., Chave, A. D., Evans, R. L., Hirth, G., Mackie, R. L. (2006). Mantle dynamics beneath the
1149 East Pacific Rise at 17°S: Insights from the Mantle Electromagnetic and Tomography (MELT)
1150 experiment. *Journal of Geophysical Resesearch* **111**, B02101.
1151 Bailey, R. C. (1970). Inversion of the geomagnetic induction problem. *Proceedings of the Royal*
1152 *Society* **315**, 185-194.
1153 Bagnardi, M., Amelung, F., Poland, M. P. (2013). A new model for the growth of basaltic shields
1154 based on deformation of Fernandina volcano, Galápagos Islands. *Earth and Planetary Science*
1155 *Letters* **377**, 358-366.
1156 Balsley, J. R, & Buddington, A. F. (1960). Magnetic susceptibility anisotropy and fabric of some
1157 Adirondack granites and orthogneisses. *American Journal of Science* **A258**, 6-20.
1158 Bannister, S., Reyners, M., Stuart, G. & Savage, M. (2007). Imaging the Hikurangi subduction
1159 zone, New Zealand, using teleseismic receiver functions: crustal fluids above the forearc mantle
1160 wedge. *Geophysical Journal International* ***169***, 602-616.
1161 Battaglia, M., Roberts, C. & Segall, P. (1999). Magma intrusion beneath Long Valley caldera
1162 confirmed by temporal changes in gravity. *Science* **285**, 2119-2122.
1163 Battaglia, M. & Segall, P. (2004). The Interpretation of Gravity Changes and Crustal Deformation
1164 in Active Volcanic Areas. *Pure and Applied Geophysics* **161**, 1453-1467.
1165 Battaglia, M., Troise, C., Obrizzo, F., Pingue, F. & De Natale, G. (2006). Evidence for fluid
1166 migration as the source of deformation at Campi Flegrei caldera (Italy). *Geophysical Research*
1167 *Letters* **33**, L01307.

1168 Bemis, S. P., Micklethwaite, S., Turner, D., James, M. R., Akciz, S., Thiele, S., Bangash, H. A.
1169 (2014). Ground-based and UAV-Based photogrammetry: A multi-scale, high-resolution mapping
1170 tool for structural geology and paleoseismology. *Journal of Structural Geology* **69**, 163-178.
1171 Bergantz, G. W., Schleicher, J. M., Burgisser, A. (2015) Open-system dynamics and mixing in
1172 magma mushes. *Nature Geoscience* **8**, 793-796.
1173 Berryman, J. G. (1980). Long-wavelength propagation in composite elastic media II. Ellipsoidal
1174 inclusions. *The Journal of the Acoustical Society of America* **68**, 1820-1831.
1175 Bersi, M., Saibi, H. & Chabou, M. C. (2016). Aerogravity and remote sensing observations of an
1176 iron deposit in Gara Djebilet, southwestern Algeria. *Journal of African Earth Sciences* **116**, 134-
1177 150.
1178 Biedermann, A. R., Pettke, T., Reusser, E., Hirt, A. M. (2014). Anisotropy of magnetic
1179 susceptibility in natural olivine single crystals. *Geochemistry, Geophysics, Geosystems* **15**, 3051–
1180 3065.
1181 Biggs, J., Anthony, E. Y. & Ebinger, C. J. (2009). Multiple inflation and deflation events at Kenyan
1182 volcanoes, East African Rift. *Geology* **37**, 979-982.
1183 Biggs, J., Bastow, I. D., Keir, D. & Lewi, E. (2011). Pulses of deformation reveal frequently
1184 recurring shallow magmatic activity beneath the Main Ethiopian Rift. Geochemistry. *Geophysics,*
1185 *Geosystems* **12**, Q0AB10.
1186 Biggs, J., Ebmeier, S. K., Aspinall, W. P., Lu, Z., Pritchard, M. E., Sparks, R. S. J., Mather, T. A.
1187 (2014). Global link between deformation and volcanic eruption quantified by satellite
1188 imagery. *Nature Communications* **5**, 3471.
1189 Biggs, J. & Pritchard, M. E. (2017). Global volcano monitoring: what does it mean when volcanoes
1190 deform?. *Elements* **13**, 17-22.
1191 Bonforte, A., Carbone, D., Greco, F. & Palano, M. (2007). Intrusive mechanism of the 2002 NE-rift
1192 eruption at Mt Etna (Italy) modelled using GPS and gravity data. *Geophysical Journal International*
1193 **169**, 339-347.

1194 Borradaile, G. J. & Henry, B. (1997). Tectonic applications of the magnetic susceptibility and its
1195 anisotropy. *Earth Science Reviews* **42**, 49-93.
1196 Bosworth, W., Stockli, D. F. & Helgeson, D. E. (2015). Integrated outcrop, 3D seismic, and
1197 geochronologic interpretation of Red Sea dike-related deformation in the Western Desert, Egypt–
1198 The role of the 23Ma Cairo “mini-plume”. *Journal of African Earth Sciences* **109**, 107-119.
1199 Bott, M. H. P. (1953). Negative gravity anomalies over acid "intrusions" and their relation to the
1200 structure of the Earth's crust. *Geological Magazine* **90**, 257-267.
1201 Bouchez, J. L. (1997). Granite is never isotropic: An introduction to AMS studies of granitic rocks.
1202 In: Bouchez, J. L., Hutton, D. H. W., Stephens, W. E. (eds) Granite: From Segregation of Melt to
1203 Emplacement Fabrics 8: pp. 95-112. Dordrecht: Kluwer Academic.
1204 Brown, A. R. (2004). *Interpretation of three-dimensional seismic data*. Oklahoma, USA: AAPG
1205 and SEG.
1206 Brun, J. P., Gapais, D., Cogne, J. P., Ledru, P. & Vigneresse, J. L. (1990). The Flamanville granite
1207 (northwest France): an unequivocal example of a syntectonically expanding pluton. *Geological*
1208 *Journal* **25**, 271-286.
1209 Bucher, W. H. (1944). Discussion in Romberg, F., and Barnes, V. E. Correlation of gravity
1210 observations with the geology of the Smoothingiron granite mass, Llano County, Texas. *Geophysics*
1211 **9**, 79-93.
1212 Callot, J. -P., Geoffroy, L., Aubourg, C., Pozzi, J., Mege, D. (2001). Magma flow directions of
1213 shallow dykes from the East Greenland volcanic margin inferred from magnetic fabric studies.
1214 *Tectonophysics* **335**, 313-329.
1215 Carbone, D., Poland, M. P., Patrick, M. R. & Orr, T. R. (2013). Continuous gravity measurements
1216 reveal a low-density lava lake at Kīlauea Volcano, Hawai‘i. *Earth and Planetary Science Letters*
1217 **376**, 178-185.

1218 Carbone, D., Poland, M. P., Diament, M. & Greco, F. (2017). The added value of time-variable
1219 microgravimetry to the understanding of how volcanoes work. *Earth-Science Reviews* **169**, 146-
1220 179.
1221 Caricchi, L., Biggs, J., Annen, C., Ebmeier, S. (2014) The influence of cooling, crystallisation and
1222 re-melting on the interpretation of geodetic signals in volcanic systems. *Earth and Planetary*
1223 *Science Letters* **388**, 166-174.
1224 Cartwright, J. & Hansen, D. M. (2006). Magma transport through the crust via interconnected sill
1225 complexes. *Geology* **34**, 929-932.
1226 Cartwright, J. & Huuse, M. (2005). 3D seismic technology: the geological 'Hubble'. *Basin*
1227 *Research* **17**, 1-20.
1228 Cashman, K. V. & Sparks, R. S. J. (2013). How volcanoes work: A 25 year perspective. *Geological*
1229 *Society of America Bulletin* **125**, 664-690.
1230 Cashman, K. V., Sparks, R. S. J. & Blundy, J. D. (2017). Vertically extensive and unstable
1231 magmatic systems: a unified view of igneous processes. *Science* **355**, p.eaag3055.
1232 Chaussard, E. & Amelung, F. (2013) Depth of magma storage in volcanic arcs: testing the influence
1233 of regional parameters using a global data compilation. In EGU General Assembly Conference
1234 Abstracts (Vol. 15).
1235 Cheadle, M. J., & Gee, J. S. (2017). Quantitative textural insights into the formation of gabbro in
1236 mafic intrusions. *Elements* **13**, 409-414.
1237 Chen, Y., Durlofsky, L. J., Gerritsen, M., Wen, X. H. (2003). A coupled local–global upscaling
1238 approach for simulating flow in highly heterogeneous formations. *Advances in Water Resources* **26**,
1239 1041-1060.
1240 Chmielowski, J., Zandt, G. & Haberland, C. (1999). The central Andean Altiplano-Puna magma
1241 body. *Geophysical Research Letters* **26**, 783-786.
1242 Chouet, B., Dawson, P., Martini, M. (2008). Shallow-conduit dynamics at Stromboli Volcano, Italy,
1243 imaged from waveform inversions. In: Lane, S. J., Gilbert, J. S. (Eds.), Fluid Motions in Volcanic

1244 Conduits: A Source of Seismic and Acoustic Signals. *Geological Society of London Special*
1245 *Publication* **307**, 57-84.
1246 Christopher, T. E., Blundy, J. D., Cashman, K., Cole, P., Edmonds, M., Smith, P. J., Sparks, R. S. J.
1247 & Stinton, A. (2015). Crustal-scale degassing due to magma system destabilization and magma-gas
1248 decoupling at Soufrière Hills Volcano, Montserrat. *Geochemistry Geophysics Geosystems* **16**, 2797-
1249 2811.
1250 Chouet, B. & Matoza, R. S. (2013). A Multi-decadal view of seismic methods for detecting
1251 precursors of magma movement and eruption. *Journal of Volcanology and Geothermal Research*
1252 **252**, 108-175.
1253 Class, H., Ebigbo, A., Helmig, R., Dahle, H. K., Nordbotten, J. M., Celia, M. A., Audigane, P.,
1254 Darcis, M., Ennis-King, J., Fan, Y., Flemisch, B. (2009). A benchmark study on problems related to
1255 CO2 storage in geologic formations. *Computational Geosciences* **13**, 409-434.
1256 Clemente, C. S., Amorós, E. B. & Crespo, M. G. (2007). Dike intrusion under shear stress: effects
1257 on magnetic and vesicle fabrics in dikes from rift zones of Tenerife (Canary Islands). *Journal of*
1258 *Structural Geology* **29**, 1931-1942.
1259 Comeau, M. J., Unsworth, M. J., Ticona, F., Sunagua, M. (2015). Magnetotelluric images of
1260 magma distribution beneath Volcán Uturuncu, Bolivia: Implications for magma dynamics. *Geology*
1261 **43**, 243-246.
1262 Comeau, M. J., Unsworth, M. J., Cordell, D. (2016). New constraints on the magma distribution
1263 and composition beneath Volcán Uturuncu and the southern Bolivian Altiplano from
1264 magnetotelluric data. *Geosphere* **12**, 1391-1421.
1265 Constable, S. C., Parker, R. L., Constable, C. G. (1987). Occam's inversion: A practical algorithm
1266 for generating smooth models from electromagnetic sounding data. *Geophysics* **52**, 289-300.
1267 Cruden, A. R. & Launeau, P. (1994). Structure, magnetic fabric and emplacement of the Archean
1268 Lebel Stock, SW Abitibi greenstone belt. *Journal of Structural Geology* **16**, 677-691.

1269 Cruden, A. R., Tobisch, O. T., Launeau, P. (1999). Magnetic fabric evidence for conduit fed
1270 emplacement of a tabular granite: Dinkey Creek Pluton, central Sierra Nevada Batholith, California.
1271 *Journal of Geophysical Research* **104**, 10,511-10,531.
1272 Cruden, A. R. & Weinberg, R. F. (2018). Mechanisms of magma transport and storage in the lower
1273 and middle crust – magma segregation, ascent and emplacement. In: Burkhardt, S. (Ed). *Volcanic*
1274 *and Igneous Plumbing Systems*, Elsevier, Amsterdam, In Press.
1275 Currenti, G., Del Negro, C. & Ganci, G. (2007). Modelling of ground deformation and gravity
1276 fields using finite element method: an application to Etna volcano. *Geophysical Journal*
1277 *International* **169**, 775-786.
1278 Currenti, G., Napoli, R., Coco, A. & Privitera, E. (2017). Effects of hydrothermal unrest on stress
1279 and deformation: insights from numerical modeling and application to Vulcano Island (Italy).
1280 *Bulletin of Volcanology* **79**, 28.
1281 de Saint Blanquat, M. & Tikoff, B. (1997). Development of magmatic to solid-state fabrics during
1282 syntectonic emplacement of the Mono Creek Granite, Sierra Nevada Batholith. In *Granite: from*
1283 *segregation of melt to emplacement fabrics*, Springer Netherlands, 231-252.
1284 Dean, O. S. & Chen, Y. (2011). Recent progress on reservoir history matching: a review.
1285 *Computational Geosciences* **15**, 152-221.
1286 DeGruyter, W. & Huber, C. (2014). A model for eruption frequency of upper crustal silicic magma
1287 chambers. *Earth and Planetary Science Letters* **403**, 117-130.
1288 del Potro, R., Díez, M., Blundy, J., Gottsmann, J. & Camacho, A. (2013). Diapiric ascent of silicic
1289 magma beneath the Bolivian Altiplano. *Geophysical Research Letters* **40**, 2044-2048.
1290 Delph, J. R., Ward, K. M., Zandt, G., Ducea, M. N., Beck, S. L. (2017). Imaging a magma
1291 plumbing system from MASH zone to magma reservoir. *Earth and Planetary Science Letters* **457**,
1292 313-324.
1293 Desissa, M., Johnson, N. E., Whaler, K. A., Hautot, S., Fisseha, S., Dawes, G. (2013). A mantle
1294 magma reservoir beneath an incipient mid-ocean ridge in Afar, Ethiopia. *Nature Geoscience* **6,** 861-

865.

Di Maio, R., Mauriello, P., Patella, D., Petrillo, Z., Piscitelli, S., Siniscalchi, A. (1998). Electric and electromagnetic outline of the Mount Somma–Vesuvius structural setting. *Journal of Volcanology and Geothermal Research* **82**, 219-238.

Dixon, T. H. (1991). An introduction to the Global Positioning System and some geological applications. *Reviews of Geophysics* **29**, 249-276.

Drew, J., White, R. S., Tilmann, F., Tarasewicz, J. (2013) Coalescence microseismic mapping. *Geophysical Journal International* **195**, 1773-1785.

Dugda, M. T., Nyblade, A. A., Julia, J., Langston, C. A., Ammon, C. J., Simiyu, S. (2005). Crustal structure in Ethiopia and Kenya from receiver function analysis: Implications for rift development in eastern Africa. *Journal of Geophysical Research* **110**, B01303.

Dunlop, D. J. (2002). Theory and application of the Day plot (Mrs/Ms versus Hcr/Hc) 1. Theoretical curves and tests using titanomagnetite data. *Journal of Geophysical Research: Solid Earth* **107**(B3).

Dunlop, D. J. & Özdemir, Ö. (2001). Rock magnetism: fundamentals and frontiers (Vol. 3). Cambridge university press.

Dvorak, J. J. & Dzurisin, D. (1997). Volcano geodesy: The search for magma reservoirs and the formation of eruptive vents. *Reviews of Geophysics* **35**, 343-384.

Dzurisin, D. (2006). Volcano deformation: new geodetic monitoring techniques. Springer Science & Business Media.

Eaton, G. P., Christiansen, R. L., Iyer, H. M., Pitt, A. D., Mabey, D. R., Blank, H. R., Zietz, I. & Gettings, M. E. (1975). Magma Beneath Yellowstone National park. *Science* **188,** 787.

Ebinger, C., Keir, D., Ayele, A., Calais, E., Wright, T. J., Belachew, M., Hammond, J. O. S., Campbell, E., Buck, W. R. (2008). Capturing magma intrusion and faulting processes during continental rupture: seismicity of the Dabbahu (Afar) rift. *Geophysical Journal International* **174**, 1138-1152.

1321 Ebinger, C. J., Keir, D., Bastow, I. D., Whaler, K., Hammond, J. O., Ayele, A., Miller, M. S.,
1322 Tiberi, C., Hautot, S. (2017). Crustal structure of active deformation zones in Africa: Implications
1323 for global crustal processes. *Tectonics*.
1324 Ebmeier, S. K., Elliott, J. R., Nocquet, J. M., Biggs, J., Mothes, P., Jarrín, P., Yépez, M., Aguaiza,
1325 S., Lundgren, P., Samsonov, S. V. (2016). Shallow earthquake inhibits unrest near Chiles–Cerro
1326 Negro volcanoes, Ecuador–Colombian border. *Earth and Planetary Science Letters* **450**, 283-291.
1327 Ebmeier, S. K., Andrews, B. J., Araya, M. C., Arnold, D. W. D., Biggs, J., Cooper, C. & 10 others.
1328 (2018). Synthesis of global satellite observations of magmatic and volcanic deformation:
1329 implications for volcano monitoring & the lateral extent of magmatic domains. *Journal of Applied*
1330 *Volcanology*, **7**, 2.
1331 Eide, C. H., Schofield, N., Lecomte, I., Buckley, S. J. and Howell, J. A. (2017a). Seismic
1332 interpretation of sill complexes in sedimentary basins: implications for the sub-sill imaging
1333 problem. *Journal of the Geological Society of London*, jgs2017-096.
1334 Eide, C. H., Schofield, N., Jerram, D. A., Howell, J. A. (2017b). Basin-scale architecture of deeply
1335 emplaced sill complexes: Jameson Land, East Greenland. *Journal of the Geological Society of*
1336 *London* **174**, 23-40.
1337 Eisenbeiss, H. (2009). UAV Photogrammetry. PhD thesis. ETH Zurich.
1338 Ernst, R. E. & Baragar, W. R. A. (1992). Evidence from magnetic fabric for the flow pattern of
1339 magma in the Mackenzie giant radiating dyke swarm. *Nature* **356**, 511.
1340 Féménias, O., Diot, H., Berza, T., Gauffriau, A., Demaiffe, D. (2004). Asymmetrical to symmetrical
1341 magnetic fabric of dikes: Paleo-flow orientations and Paleo-stresses recorded on feeder-bodies from
1342 the Motru Dike Swarm (Romania). *Journal of Structural Geology* **26**, 1401-1418.
1343 Ferguson, I. J. (2012). Instrumentation and field procedures, in *The Magnetotelluric Method:*
1344 *Theory and Practice*, ed. Chave, A. D. & Jones, A. G., Cambridge University Press.

1345 Field, L., Blundy, J. D., Brooker, R. A., Wright, T., Yirgu, G. (2012) Magma storage conditions
1346 beneath Dabbahu volcano (Ethiopia) constrained by petrology, seismicity and satellite geodesy.
1347 *Bulletin of Volcanology* **74**, 981-1004.
1348 Fournier, T. J., Pritchard, M. E., Riddick, S. N. (2010). Duration, magnitude, and frequency of
1349 subaerial volcano deformation events: New results from Latin America using InSAR and a global
1350 synthesis. *Geochemistry, Geophysics, Geosystems* **11**, Q01003.
1351 Gaillard, F. (2004). Laboratory measurements of electrical conductivity of hydrous and dry silicic
1352 melts under pressure. *Earth and Planetary Science Letters* **218**, 215-228.
1353 Galland, O. (2012). Experimental modelling of ground deformation associated with shallow magma
1354 intrusions. *Earth and Planetary Science Letters* **317**, 145-156.
1355 Gamble, T. D., Goubau, W. M., Clarke, J. (1979). Magnetotellurics with a remote magnetic
1356 reference. *Geophysics* **44**, 53-68.
1357 Garapic, G., Faul, U. H., Brisson, E. (2013). High-resolution imaging of the melt distribution in
1358 partially molten upper mantle rocks: evidence for wetted two-grain boundaries. *Geochemistry*
1359 *Geophysics Geosystems* **14**, 556-566.
1360 Geoffroy, L., Callot, J. P., Aubourg, C. & Moreira, M. (2002). Magnetic and plagioclase linear fabric
1361 discrepancy in dykes: a new way to define the flow vector using magnetic foliation. *Terra Nova* **14**,
1362 183-190.
1363 Gerst, A. & Savage, M. K. (2004). Seismic anisotropy beneath Ruapehu volcano: a possible eruption
1364 forecasting tool. *Science* **306**, 1543-1547.
1365 Glazner, A. F., Bartley, J. M. & Coleman, D. S. (2016). We need a new definition for "magma". *Eos*
1366 **97**.
1367 Glen, J. M., Renne, P. R., Milner, S. C., Coe, R. S. (1997). Magma flow inferred from anisotropy of
1368 magnetic susceptibility in the coastal Parana-Etendeka igneous province: Evidence for rifting before
1369 flood volcanism. *Geology* **25**, 1131-1134.
1370 Goes, S., Armitage, J., Harmon, N., Smith, H., Huismans, R. (2012). Low seismic velocities below

1371 mid-ocean ridges: Attenuation versus melt retention. *Journal of Geophysical Research* **117**, B12403.
1372 Gottsmann, J., Rymer, H. & Wooller, L. K. (2005). On the interpretation of gravity variations in the
1373 presence of active hydrothermal systems: Insights from the Nisyros Caldera, Greece. *Geophysical*
1374 *Research Letters* **32**, L23310.
1375 Gottsmann, J., Camacho, A. G., Tiampo, K. F. & Fernández, J. (2006). Spatiotemporal variations in
1376 vertical gravity gradients at the Campi Flegrei caldera (Italy): a case for source multiplicity during
1377 unrest?. *Geophysical Journal International* **167**, 1089-1096.
1378 Gottsmann, J., Carniel, R., Coppo, N., Wooller, L., Hautmann, S. & Rymer, H. (2007). Oscillations
1379 in hydrothermal systems as a source of periodic unrest at caldera volcanoes: Multiparameter insights
1380 from Nisyros, Greece. *Geophysical Research Letters* **34**, L07307.
1381 Gottsmann, J., Camacho, A. G., Marti, J., Wooller, L., Fernández, J., Garcia, A. & Rymer, H. (2008).
1382 Shallow structure beneath the Central Volcanic Complex of Tenerife from new gravity data:
1383 Implications for its evolution and recent reactivation. *Physics of the Earth and Planetary Interior* **68**
1384 212-230.
1385 Gottsmann, J., Blundy, J. D., Henderson, S., Pritchard, M. E. & Sparks, R. S. J. (2017).
1386 Thermomechanical Modeling of the Altiplano-Puna Deformation Anomaly: Multiparameter Insights
1387 into Magma Mush Reorganization. *Geosphere* **13**, 1042-1065.
1388 Graham, J. W. (1954). Magnetic anisotropy, an unexploited petrofabric element. *Geological Society*
1389 *of America Bulletin* **65**, 1257-1258.
1390 Gudmundsson, O., Brandsdottir, B., Menke, W. & Sigvaldason, G. E. (1994). The crustal magma
1391 chamber of the Katla volcano in south Iceland revealed by 2-D seismic undershooting. *Geophysical*
1392 *Journal International* **119**, 277-296.
1393 Guidarelli, M., Stuart, G., Hammond, J. O., Kendall, J. M., Ayele, A., Belachew, M. (2011).
1394 Surface wave tomography across Afar, Ethiopia: Crustal structure at a rift triple-junction zone.
1395 *Geophysical Research Letters* **38**, L24313.

1396 Guo, X., Zhang, L., Behrens, H., Ni, H. (2016). Probing the status of felsic magma reservoirs:
1397 Constraints from the *P*–*T*–H_2O dependences of electrical conductivity of rhyolitic melt. *Earth and*
1398 *Planetary Science Letters* **433**, 54-62.
1399 Gutierrez, F., Payacan, I., Gelman, S. E., Bachmann, O., Parada, M. A. (2013) Late-stage magma
1400 flow in a shallow felsic reservoir: Merging the anisotropy of magnetic susceptibility record with
1401 numerical simulations in La Gloria Pluton, central Chile. *Journal of Geophysical Research-Solid*
1402 *Earth* **118**, 1984-1998.
1403 Hamilton, M. P., Jones, A. G., Evans, R. L., Evans, S., Fourie, C. J. S., Garcia, X., Mountford, A,
1404 Spratt, J. E., SAMTEX MT Team. (2006). Electrical anisotropy of South African lithosphere
1405 compared with seismic anisotropy from shear-wave splitting analyses. *Physics of the Earth and*
1406 *Planetary Interiors* **158**, 226-239.
1407 Hamling, I. J., Wright, T. J., Calais, E., Bennati, L., Lewi, E. (2010). Stress transfer between
1408 thirteen successive dyke intrusions in Ethiopia. *Nature Geoscience* **3**(10), 713-717.
1409 Hamling, I. J., Hreinsdottir, S. & Fournier, N. (2015). The ups and downs of the TVZ: Geodetic
1410 observations of deformation around the Taupo Volcanic Zone, New Zealand. *Journal of*
1411 *Geophysical Research: Solid Earth* **120**, 4667-4679.
1412 Hammer, S. (1945). Estimating ore masses in gravity prospecting. *Geophsyics* **10**, 50-62.
1413 Hammond, W. & Humphreys, E. (2000a). Upper mantle seismic wave velocity: Effects of realistic
1414 partial melt geometries. *Journal of Geophysical Research* **105**, 10975-10986.
1415 Hammond, W. & Humphreys, E. (2000b). Upper mantle seismic wave attenuation: Effects of
1416 realistic partial melt distribution, *Journal of Geophysical Research* **105**, 10987-10999.
1417 Hammond, J. O. S., Kendall, J., Stuart, G. W., Keir, D., Ebinger, C. J., Ayele, A., Belachew, M.
1418 (2011). The nature of the crust beneath the Afar triple junction: Evidence from receiver functions.
1419 *Geochemistry Geophysics Geosystems* **12**, Q12004.
1420 Hammond, J. O. S. (2014). Constraining melt storage geometries beneath the Afar Depression,
1421 Ethiopia from teleseismic receiver functions: The anisotropic H-κ stacking technique. *Geochemistry*

Geophysics Geosystems **15**, 1316-1332.

Hammond, J. O. S. & Kendall, J. (2016). Constraints on melt distribution from seismology: a case study in Ethiopia. In: Wright, T. J., Ayele, A., Ferguson, D. J., Kidane, T., Vye-Brown, C. (eds.) *Magmatic Rifting and Active Volcanism*. Geological Society, Special Publication, London **420**, 127-147.

Hansen, D. M. & Cartwright, J. (2006). The three-dimensional geometry and growth of forced folds above saucer-shaped igneous sills. *Journal of Structural Geology* **28**, 1520-1535.

Hargraves, R. B., Chan, C. Y., Johnson, D. (1991). Distribution anisotropy: the cause of AMS in igneous rocks? *Geophysical Research Letters* **18**, 2193-2196.

Hargraves, R. B., Briden, J. C., Daniels, B. A. (1999). Palaeomagnetism and magnetic fabric in the Freetown Complex, Sierra Leone. *Geophysical Journal International* **I36**, 705-713.

Harmon, N., & Rychert, C. A. (2015). Seismic imaging of deep crustal melt sills beneath Costa Rica suggests a method for the formation of the Archean continental crust. *Earth and Planetary Science Letters* **430**, 140-148.

Hashin, Z. & Shtrikman, S. (1962). A variational approach to the theory of the effective magnetic permeability of multiphase materials. *Journal of Applied Physics* **33**, 3125-3131.

Hawkesworth, C. J., Blake, S., Evans, P., Hughes, R., Macdonald, R., Thomas, L. E., Turner, S. P., Zellmer, G. (2000). Time scales of crystal fractionation in magma chambers—integrating physical, isotopic and geochemical perspectives. *Journal of Petrology* **41**, 991-1006.

Heinson, G., Constable, S., White, A. (2000). Episodic melt transport at mid-ocean ridges inferred from magnetotelluric sounding. *Geophysical Research Letters* **27**, 2317-2320.

Hemmings, B., Coco, A., Gottsmann, J., Whitaker, F. (2016). Investigating hydrological contributions to volcano monitoring signals. *Geophysical Journal International* **207**, 259-273.

Herrero-Bervera, E., Walker, G., Canon-Tapia, E., Garcia, M. (2001). Magnetic fabric and inferred flow direction of dikes, conesheets and sill swarms, Isle of Skye, Scotland. *Journal of Volcanology and Geothermal Research* **106**, 195-210.

1448 Hickey, J., Gottsmann, J., Nakamichi, H., Iguchi, M. (2016). Thermomechanical controls on magma
1449 supply and volcanic deformation: application to Aira caldera, Japan. *Scientific Reports* **6**, 32691.
1450 Hickey, J., Gottsmann, J., Mothes, P., Odbert, H., Prutkin, I., Vajda, P. (2017). The ups and downs
1451 of volcanic unrest: insights from integrated geodesy and numerical modelling. Advances in
1452 Volcanology, 1-17, Springer.
1453 Hildreth, W. (2004). Volcanological perspectives on Long Valley, Mammoth Mountain, and Mono
1454 Craters: several contiguous but discrete systems. *Journal of Volcanology and Geothermal Research*
1455 **136**, 169-198.
1456 Hodgetts, D. (2013). Laser scanning and digital outcrop geology in the petroleum industry: A
1457 review. *Marine and Petroleum Geology* **46**, 335-354.
1458 Hooft, E. E. E., Morgan, J. V., Nomikou, P., Toomey, D. R., Papazachos, C. V., Warner, M., Heath,
1459 B., Christopoulou, M-E., Lampridou, D., Kementzetzidou, D. (2016). The PROTEUS Experiment:
1460 Active Source Seismic Imaging of the Crustal Magma Plumbing Structure of the Santorini Arc
1461 Volcano. *AGU Fall meeting*, Abstract# DI23B-2619.
1462 Holohan, E. P., Sudhaus, H., Walter, T. R., Schöpfer, M. P., Walsh, J. J. (2017). Effects of Host-
1463 rock Fracturing on Elastic-deformation Source Models of Volcano Deflation. *Scientific Reports* **7**,
1464 10970.
1465 Hrouda, F. (1982). Magnetic anisotropy of rocks and its application in geology and geophysics.
1466 *Geophysical Surveys* **5**, 37-82.
1467 Hrouda, F., Schulmann, K., Suppes, M., Ullemayer, K., de Wall, H., Weber, K. (1997). Quantitative
1468 relationship between low-field AMS and phyllosilicate fabric: a review. *Physics and Chemistry of*
1469 *the Earth* **22**, 153-156.
1470 Hübert, J., Whaler, K. A., Fisseha, S. (2018). The electrical structure of the Central Main Ethiopian
1471 Rift as imaged by Magnetotellurics - Implications for magma storage and pathways. *Journal of*
1472 *Geophysical Research*, in review.

1473 Hunt, T. & Bowyer, D. (2007). Reinjection and gravity changes at Rotokawa geothermal field, New
1474 Zealand. *Geothermics* **36**, 421-435.
1475 Husen, S., Taylor, R., Smith, R. B., Healser, H. (2004). Changes in geyser eruption behavior and
1476 remotely triggered seismicity in Yellowstone National Park produced by the 2002 M 7.9 Denali
1477 fault earthquake, Alaska. *Geology* **32**(6), 537-540.
1478 Ivanic, T., Zibra, I., Doublier, M., Wyche, S. (2013). Geological Interpretation of the Youanmi and
1479 Southern Carnarvon seismic lines 10GA-YU1, 10GA-YU2, 10GA-YU3, and 11GA-SC1. In:
1480 Wyche, S., Ivanic, T., Zibra, I. (eds.) *Youanmi and Southern Carnarvon seismic and*
1481 *magnetotelluric (MT) workshop 2013*. Geological Survey of Western Australia, Plate 3.
1482 Jachens, R. C. & Roberts, C. W. (1985). Temporal and areal gravity investigations at Long Valley
1483 Caldera, California. *Journal of Geophysical Research* **90**, 11210-11218.
1484 Jackson, C. A.-L., Schofield, N., Golenkov, B. (2013). Geometry and controls on the development
1485 of igneous sill–related forced folds: A 2-D seismic reflection case study from offshore southern
1486 Australia. *Geological Society of America Bulletin* **125**, 1874-1890.
1487 Jackson, I., Fitzgerald, J. D., Faul, U. H., Tan, B. H. (2002). Grain-size-sensitive seismic wave
1488 attenuation in polycrystalline olivine. *Journal of Geophysical Research* **107**, B12, 2156-2202.
1489 Jaxybulatov, K., Shapiro, N. M., Koulakov, I., Mordret, A., Landes, M., Sens-Schonfelder, C. (2014).
1490 A large magmatic sill complex beneath the Toba caldera. *Science* **346**, 617-619.
1491 Jay, J. A., Pritchard, M. E., West, M. E., Christensen, D. H., Haney, M., Minaya, E., Sunagua, M.,
1492 McNutt, S. R., Zabala, M. (2012). Shallow seismicity, triggered seismicity, and ambient noise
1493 tomography at the long-dormant Uturuncu volcano, Bolivia. *Bulletin of Volcanology* **74**, 817-837.
1494 Jay, J., Costa, F., Pritchard, M., Lara, L., Singer, B., Herrin, J. (2014). Locating magma reservoirs
1495 using InSAR and petrology before and during the 2011–2012 Cordón Caulle silicic eruption. *Earth*
1496 *and Planetary Science Letters* **395**, 254-266.
1497 Johnson, J. H. & Poland, M. P. (2013). Seismic detection of increased degassing before Kīlauea's
1498 2008 summit explosion. *Nature communications* **4**, 1668.

1499 Johnson, N. E., Whaler, K. A., Hautot, S., Fisseha, S., Desissa, M. & Dawes, G. J. K. (2016). Magma
1500 imaged magnetotellurically beneath an active and an inactive magmatic segment in Afar, Ethiopia.
1501 *Geological Society, London, Special Publications* **420**, 105-125.
1502 Jones, A. G. (2012). Distortion of magnetotelluric data: its identification and removal, in *The*
1503 *Magnetotelluric Method: Theory and Practice*, ed. Chave, A. D. & Jones, A. G., Cambridge
1504 University Press.
1505 Jousset, P., Mori, H. & Okada, H. (2000). Possible magma intrusion revealed by temporal gravity,
1506 ground deformation and ground temperature observations at Mount Komagatake (Hokkaido) during
1507 the 1996-1998 crisis. *Geophysical Journal International* **143**, 557-574.
1508 Kalinicheva, T., Warner, M., Ashley, J., Mancini, F. (2017). Two vs three-dimensional FWI in a 3D
1509 world. S*EG International Exhibition and 87th Annual Meeting*.
1510 Kamei, R., Jang, U. G., Lumley, D., Mouri, T., Nakatsukasa, M., Kato, A. & Takanashi, M. (2017).
1511 Time-lapse Full Waveform Inversion for Monitoring Near-surface Microbubble Injection. *79th*
1512 *Conference and Exhibition, EAGE, Extended Abstracts*.
1513 Kapoor, S., Vigh, D., Wiarda, E., Alwon, S. (2013). Full waveform inversion around the world. *75th*
1514 *Conference and Exhibition, EAGE, Extended Abstracts*.
1515 Karato, S. & Jung, H. (1998). Water, partial melting and the origin of the seismic low velocity and
1516 high attenuation zone in the upper mantle. *Earth and Planetary Science Letters* **157**, 193-207.
1517 Kavanagh, J. L., Burns, A. J., Hazim, S. H., Wood, E., Martin, S. A., Hignett, S. Dennis, D. J. 2018.
1518 Challenging dyke ascent models using novel laboratory experiments: Implications for reinterpreting
1519 evidence of magma ascent and volcanism. *Journal of Volcanology and Geothermal Research*.
1520 Keir, D., Hamling, I. J., Ayele, A., Calais, E., Ebinger, C. J., Wright, T. J., Jacques, E., Mohamed,
1521 K., Hammond, J. O. S., Belachew, M., Baker, E., Rowland, J. V., Lewi, E., Bennati, L. (2009).
1522 Evidence for focused magmatic accretion at segment centers from lateral dike injection captured
1523 beneath the Red Sea rift of Afar. *Geology* **37**, 59-62.
1524 Keir, D., Belachew, M., Ebinger, C. J., Kendall, J. -M., Hammond, J. O. S., Stuart, G. W., Ayele, A.,

1525 Rowland, J. R. (2011). Mapping the evolving strain field during continental breakup from crustal
1526 anisotropy in the Afar Depression. *Nature Communications* **2**, 285–7.
1527 Kelso, P. R., Tikoff, B., Jackson, M., Sun, W. (2002). A new method for the separation of
1528 paramagnetic and ferromagnetic susceptibility anisotropy using low field and high field methods.
1529 *Geophysical Journal International* **151**, 345-359.
1530 Kent, G. M., Singh, S. C., Harding, A. J., Sinha, M. C., Orcutt, J. A. (2000). Evidence from three-
1531 dimensional seismic reflectivity images for enhanced melt supply beneath mid-ocean-ridge
1532 discontinuities. *Nature* **406**, 614-618.
1533 Key, K., Constable, S., Liu, L., Pommier, A. (2013). Electrical image of passive upwelling beneath
1534 the northern East Pacific Rise. *Nature* **495**, 499-502.
1535 Khan, M. A. (1962). The anisotropy of magnetic susceptibility of some igneous and metamorphic
1536 rocks. *Journal of Geophysical Research* **67**, 2873-2885.
1537 Kim, D., Brown, L. D., Árnason, K., Águstsson, K., Blanck, H. (2017). Magma reflection imaging in
1538 Krafla, Iceland, using microearthquake sources. *Journal of Geophysical Research Solid Earth* **122**,
1539 5228-5242.
1540 Kiser, E., Levander, A., Schmandt, B., Palomeras, I., Harder, S. H., Creager, K. C., Vidale, J. E.,
1541 Malone, S. D. (2014). Field report on the iMUSH active source seismic experiment. *AGU Fall*
1542 *Meeting Abstracts* **1**, 2.
1543 Knight, M. D. & Walker, G. P. (1988). Magma flow directions in dikes of the Koolau Complex,
1544 Oahu, determined from magnetic fabric studies. *Journal of Geophysical Research* **93**, 4301-4319.
1545 Koulakov, I., Gordeev, E. I., Dobretsov, N. L., Vernikovsky, V. A., Senyukov, S., Jakovlev, A. &
1546 Jaxybulatov, K. (2013). Rapid changes in magma storage beneath the Klyuchevskoy group of
1547 volcanoes inferred from time-dependent seismic tomography. *Journal of Volcanology and*
1548 *Geothermal Research* **263**, 75-91.

1549 Laumonier, M., Gaillard, F., Sifre, D. (2015). The effect of pressure and water concentration on the
1550 electrical conductivity of dacitic melts: Implication for magnetotelluric imaging in subduction areas.
1551 *Chemical Geology* **418**, 66-76.
1552 Launeau, P. & Cruden, A. R. (1998). Magmatic fabric acquisition mechanisms in a syenite: Results
1553 of a combined anisotropy of magnetic susceptibility and image analysis study. *Journal of*
1554 *Geophysical Research* **103**, 5067-5089.
1555 Lazaratos, S., Chikichev, I., Wang, K. (2011). Improving the convergence rate of full wavefield
1556 inversion using spectral shaping. *81st Annual International Meeting, SEG, Expanded Abstracts*.
1557 Le Mével, H., Feigl, K. L., Córdova, L., DeMets, C. & Lundgren, P. (2015). Evolution of unrest at
1558 Laguna del Maule volcanic field (Chile) from InSAR and GPS measurements, 2003 to 2014.
1559 *Geophysical Research Letters* **42**, 6590-6598.
1560 Leberl, F., Irschara, A., Pock, T., Meixner, P., Gruber, M., Scholz, S., Wiechert, A. (2010). Point
1561 Clouds: Lidar versus 3D Vision. *Photogrammetric Engineering and Remote Sensing* **76**, 1123-
1562 1134.
1563 Lees, J. M. (2007). Seismic tomography of magmatic systems. *Journal of Volcanology and*
1564 *Geothermal Research* **167**, 37-56.
1565 Lu, Z. Dzurisin, D. (2014). InSAR Imaging of Aleutian Volcanoes. In*InSAR Imaging of Aleutian*
1566 *Volcanoes* (pp. 87-345). Springer Berlin Heidelberg.
1567 MacGregor, L. M., Constable, S., Sinha, M. C. (1998). The RAMESSES experiment—III.
1568 Controlled-source electromagnetic sounding of the Reykjanes Ridge at 57° 45′ N. *Geophysical*
1569 *Journal International* **135**, 773-789.
1570 Magee, C., Stevenson, C. T. E., O'Driscoll, B., Schofield, N., McDermott, K. (2012a). An
1571 alternative emplacement model for the classic Ardnamurchan cone sheet swarm, NW Scotland,
1572 involving lateral magma supply via regional dykes. *Journal of Structural Geology* **43**, 73-91.

1573 Magee, C., Stevenson, C. T. E., O'Driscoll, B., Petronis, M. S. (2012b). Local and regional controls
1574 on the lateral emplacement of the Ben Hiant Dolerite intrusion, Ardnamurchan (NW Scotland).
1575 *Journal of Structural Geology* **39**, 66-82.
1576 Magee, C., Hunt-Stewart, E., Jackson, C. A. L. (2013a). Volcano growth mechanisms and the role
1577 of sub-volcanic intrusions: Insights from 2D seismic reflection data. *Earth and Planetary Science*
1578 *Letters* **373**, 41-53.
1579 Magee, C., Briggs, F., Jackson, C. A.-L. (2013b). Lithological controls on igneous intrusion-
1580 induced ground deformation. *Journal of the Geological Society* **170**, 853-856.
1581 Magee, C., Jackson, C. L., Schofield, N. (2014). Diachronous sub-volcanic intrusion along deep-
1582 water margins: insights from the Irish Rockall Basin. *Basin Research* **26**, 85-105.
1583 Magee, C., Maharaj, S. M., Wrona, T., Jackson, C. A.-L. (2015). Controls on the expression of
1584 igneous intrusions in seismic reflection data. *Geosphere*, GES01150.01151.
1585 Magee, C., Muirhead, J. D., Karvelas, A., Holford, S. P., Jackson, C. A., Bastow, I. D., Schofield,
1586 N., Stevenson, C. T., McLean, C., McCarthy, W. (2016). Lateral magma flow in mafic sill
1587 complexes. *Geosphere*, GES01256.01251.
1588 Magee, C., Bastow, I. D., van Wyk de Vries, B., Jackson, C. A. L., Hetherington, R., Hagos, M. &
1589 Hoggett, M. (2017). Structure and dynamics of surface uplift induced by incremental sill
1590 emplacement. *Geology* **45**, 431-434.
1591 Magee, C., Muirhead, J., Schofield, N., Walker, R., Galland, O., Holford, S., Spacapan, J., Jackson,
1592 C. A-L., McCarthy, W. (2017). Structural signatures of igneous sheet intrusion propagation.
1593 *EarthArXiv* doi:10.17605/OSF.IO/PDN42.
1594 Malehmir, A., Durrheim, R., Bellefleur, G., Urosevic, M., Juhlin, C., White, D. J., Milkereit, B.,
1595 Campbell, G. (2012). Seismic methods in mineral exploration and mine planning: A general
1596 overview of past and present case histories and a look into the future. *Geophysics* **77**, WC173-
1597 WC190.

1598 Mamtani, M. A., Pal, T. & Greiling, R. O. (2013). Kinematic analysis using AMS data from a
1599 deformed granitoid. *Journal of Structural Geology* **50**, 119-132.
1600 Mancini, F., Moss, J., Prindle, K., Ridsdill-Smith, T. (2015). Where can full waveform inversion
1601 have the biggest impact in the exploration and production cycle? *77th International Conference and*
1602 *Exhibition, EAGE, Extended Abstracts*.
1603 Manzella, A., Volpi, G., Zaja, A., Meju, M. (2004). Combined TEM-MT investigation of shallow-
1604 depth resistivity structure of Mt Somma-Vesuvius. *Journal of Volcanology and Geothermal*
1605 *Research* **131**, 19-32.
1606 Marjanovic, M., Carbotte, S. M., Carton, H., Nedimovic, M. R., Mutter, J. C., Canales, J. P. (2014).
1607 A multi-sill magma plumbing system beneath the axis of the East Pacific Rise. *Nature Geoscience* **7**,
1608 825-829.
1609 Mark, N. J., Schofield, N., Pugliese, S., Watson, D., Holford, S., Muirhead, D., Brown, R., Healy, D.
1610 (2017). Igneous intrusions in the Faroe Shetland basin and their implications for hydrocarbon
1611 exploration; new insights from well and seismic data. *Marine and Petroleum Geology*
1612 Masterlark, T. (2007). Magma intrusion and deformation predictions: Sensitivities to the Mogi
1613 assumptions. *Journal of Geophysical Research: Solid Earth*, **112**(B6).
1614 Masturyono., McCaffrey, R., Wark, D. A., Roecker, S. W., Fauzi Ibrahim, G. & Sukhyar. (2001).
1615 Distribution of magma beneath Toba caldera complex, north Sumatra, Indonesia, constrained by
1616 three-dimensional P wave velocities, seismicity, and gravity. *Geochemitry Geophysics Geosystems*
1617 **2**, 1014.
1618 Matsushima, N., Oshima, H., Ogawa, Y., Takakura, S., Satoh, H., Utsugi, M., Nishida, Y. (2011).
1619 Magma prospecting in Usu volcano, Hokkaido, Japan, using magnetotelluric soundings. *Journal of*
1620 *Volcanology and Geothermal Research* **109**, 263-277.
1621 McBride, J. H., William Keach, R., Leetaru, H. E. & Smith, K. M. (2018). Visualizing Precambrian
1622 basement tectonics beneath a carbon capture and storage site, Illinois Basin. *Interpretation* **6**, T257-
1623 T270.

McCabe, C., Jackson, M., Ellwood, B. B. (1985). Magnetic anisotropy in the Trenton limestone: results of a new technique, anisotropy of anhysteretic susceptibility. *Geophysical Research Letters* **12**, 333-336.

McCormick Kilbride, B., Edmonds, M. & Biggs, J. (2016). Observing eruptions of gas-rich compressible magmas from space. *Nature communications* **7**, 13744.

McKenzie, D. A. N., & O'Nions, R. K. (1991). Partial melt distributions from inversion of rare earth element concentrations. *Journal of Petrology* **32**, 1021-1091.

McLean, C. E., Schofield, N., Brown, D. J., Jolley, D. W., Reid, A. (2017). 3D seismic imaging of the shallow plumbing system beneath the Ben Nevis Monogenetic Volcanic Field: Faroe-Shetland Basin. *Journal of the Geological Society* **174**, 468-485.

Miller, V. & Savage, M. (2001). Changes in seismic anisotropy after volcanic eruptions: evidence from Mount Ruapehu. *Science* **293**, 2231-2233.

Miller, C. F., Furbish, D. J., Walker, B. A., Claiborne, L. L., Koteas, G. C., Bleick, H. A., Miller, J. S. (2011). Growth of plutons by incremental emplacement of sheets in crystal-rich host: evidence from Miocene intrusions of the Colorado River region, Nevada, USA. *Tectonophysics* **500**, 65-77.

Miller, K. J., Zhu, W., Montesi, L. G. J., Gaetani, G. A. (2014). Experimental quantification of permeability of partially molten mantle rock. *Earth and Planetary Science Letters* **388**, 273-282.

Miller, C. A., Le Mével, H., Currenti, G., Williams-Jones, G. & Tikoff, B. (2017). Microgravity changes at the Laguna del Maule volcanic field: Magma-induced stress changes facilitate mass addition. *Journal of Geophysical Research: Solid Earth* **122**, 3179-3196.

Mitchell, M. A., White, R. S., Roecker, S., Greenfield, T. (2013). Tomographic image of melt storage beneath Askja Volcano, Iceland using local microseismicity. *Geophysical Research Letters* **40**, 5040-5046.

Morgan, J. V., Warner, M., Bell, R. E., Ashley, J., Barnes, D., Little, R., Roele, K., Jones, C. (2013). Next-generation seismic experiments: wide-angle, multi-azimuth, three-dimensional, full-waveform inversion. *Geophysical Journal International* **195**, 1657-1678.

1650 Morgan, J. V., Warner, M., Arnoux, G., Hooft, E., Toomey, D., VanderBeek, B., Wilcock, W.
1651 (2016), Next-generation seismic experiments – II: wide-angle, multi-azimuth, 3-D, full-waveform
1652 inversion of sparse field data. *Geophysical Journal International* **204**, 1342-1363.
1653 Muirhead, J. D., Airoldi, G., White, J. D., Rowland, J. V. (2014). Cracking the lid: Sill-fed dikes are
1654 the likely feeders of flood basalt eruptions. *Earth and Planetary Science Letters* **406**, 187-197.
1655 Neuberg, J., Baptie, B., Luckett, R., Stewart, R. (1998). Results from the broadband seismic
1656 network on Montserrat. *Geophysical Research Letters* **25(19)**, 3661-3664.
1657 Neuberg, J., Tuffen, H., Collier, L., Green, D., Powell, T., Dingwell, D. (2006). The trigger
1658 mechanism of low-frequency earthquakes on Montserrat. *Journal of Volcanology and Geothermal*
1659 *Research* **153**, 37-50.
1660 Neves, S. P., Araújo, A. M., Correia, P. B. & Mariano, G. (2003). Magnetic fabrics in the Cabanas
1661 Granite (NE Brazil): interplay between emplacement and regional fabrics in a dextral transpressive
1662 regime. *Journal of Structural Geology* **25**, 441-453.
1663 Newman, A. V., Dixon, T. H., Gourmelen, N. (2006). A four-dimensional viscoelastic deformation
1664 model for Long Valley Caldera, California, between 1995 and 2000. *Journal of Volcanology and*
1665 *Geothermal Research* **150**(1), 244-269.
1666 O'Driscoll, B., Stevenson, C. T. E., Troll, V. R. (2008). Mineral lamination development in layered
1667 gabbros of the British Palaeogene Igneous Province: A combined anisotropy of magnetic
1668 susceptibility, textural and mineral chemistry study. *Journal of Petrology* **49**, 1187-1221.
1669 O'Driscoll, B., Ferré, E. C., Stevenson, C. T. E., Magee, C. (2015). The significance of
1670 magnetic fabrics in layered mafic-ultramafic intrusions. In: Charlier, B., Latypov, R., Namur,
1671 O., Tegner, C. (Eds), *Layered Intrusions*, Springer, 295-329.
1672 Okubo, P. G., Benz, H. M., Chouet, B. A. (1997). Imaging the crustal magma sources beneath
1673 Mauna Loa and Kilauea volcanoes, Hawaii. *Geology* **25**(10), 867-870.

1674 Orlický, O. (1990). Detection of magnetic carriers in rocks: results of susceptibility changes in
1675 powdered rock samples induced by temperature. *Physics of the Earth and Planetary Interiors*
1676 **63**, 66-70.
1677 Padilha, A. L., Vitorello, Í., Pádua, M. B., Bologna, M. S. (2006). Lithospheric and
1678 sublithospheric anisotropy beneath central-southeastern Brazil constrained by long period
1679 magnetotelluric data. *Physics of the Earth and Planetary Interiors* **158**, 190-209.
1680 Pagli, C., Wright, T. J., Ebinger, C. J., Yun, S. H., Cann, J. R., Barnie, T. & Ayele, A. (2012).
1681 Shallow axial magma chamber at the slow-spreading Erta Ale Ridge. *Nature Geoscience* **5**, 284-
1682 288.
1683 Parker, R. L. (1980). The inverse problem of electromagnetic induction: Existence and construction
1684 of solutions based on incomplete data. *Journal of Geophysical Research* **85**, 4421-4428.
1685 Parks, M. M., Biggs, J., England, P., Mather, T. A., Nomikou, P., Palamartchouk, K., Papanikolaou,
1686 X., Paradissis, D., Parsons, B., Pyle, D. M., Raptakis, C. (2012). Evolution of Santorini Volcano
1687 dominated by episodic and rapid fluxes of melt from depth. *Nature Geoscience* **5**(10), 749-754.
1688 Parker, A. L. (2016). InSAR Observations of Ground Deformation: Application to the Cascades
1689 Volcanic Arc. Springer Theses.
1690 Parmigiani, A., Faroughi, S. A., Huber, C., Bachmann, O., Su, Y. (2016) Bubble accumulation and
1691 its role on the evolution of upper crustal magma reservoirs. *Nature* **532**, 492-495.
1692 Paulatto, M., Minshull, T., Baptie, B., Dean, S., Hammond, J. O. S., Henstock, T., Kenedi, C.,
1693 Kiddle, E., Malin, P., Peirce, C., Ryan, G. (2010). Upper crustal structure of an active volcano from
1694 refraction/reflection tomography, Montserrat, Lesser Antilles. *Geophysical Journal International*
1695 **180**, 685-696.
1696 Paulatto, M., Annen, C., Henstock, T. J., Kiddle, E., Minshull, T. A., Sparks, R. S. J., Voight, B.
1697 (2012). Magma chamber properties from integrated seismic tomography and thermal modeling at
1698 Montserrat. *Geochemistry, Geophysics, Geosystems* **13**(1).

1699 Pedersen, R. & Sigmundsson, F. (2006). Temporal development of the 1999 intrusive episode in the
1700 Eyjafjallajökull volcano, Iceland, derived from InSAR images. *Bulletin of Volcanology* **68**(4), 377-
1701 393.
1702 Peron-Pinvidic, G., Shillington, D. J., Tucholke, B. E. (2010). Characterization of sills associated
1703 with the U reflection on the Newfoundland margin: evidence for widespread early post-rift
1704 magmatism on a magma-poor rifted margin. *Geophysical Journal International* **182**, 113-136.
1705 Petford, N., Cruden, A. R., McCaffrey, K. J. W. & Vigneresse, J. L. (2000). Granite magma
1706 formation, transport and emplacement in the Earth's crust. *Nature* **408**, 669-673.
1707 Petronis, M. S., Delcamp, A., de Vries, B. V. W. (2013). Magma emplacement into the Lemptégy
1708 scoria cone (Chaîne Des Puys, France) explored with structural, anisotropy of magnetic
1709 susceptibility, and Paleomagnetic data. *Bulletin of Volcanology* **75**, 753.
1710 Petronis, M. S., Brister, A. R., Rapprich, V., de Vries, B. V. W., Lindline, J., Misurec, J. (2015).
1711 Emplacement history of the Trosky basanitic volcano (Czech Republic): paleomagnetic, rock
1712 magnetic, petrologic, and anisotropy of magnetic susceptibility evidence for lingering growth of a
1713 monogenetic volcano. *Journal of Geosciences* **60**, 129-147.
1714 Petrovský, E. & Kapička, A. (2006). On determination of the Curie point from thermomagnetic
1715 curves. *Journal of Geophysical Research* **111**, B12S27.
1716 Phillips, T. B., Magee, C., Jackson, C. A. L. & Bell, R. E. (2017). Determining the three-
1717 dimensional geometry of a dike swarm and its impact on later rift geometry using seismic reflection
1718 data. *Geology* **46**, 119-122.
1719 Pinel, V., Poland, M. P., Hooper, A. (2014). Volcanology: Lessons learned from synthetic aperture
1720 radar imagery. *Journal of Volcanology and Geothermal Research* **289**, 81-113.
1721 Planke, S., Symonds, P. A., Alvestad, E., Skogseid, J. (2000). Seismic volcanostratigraphy of large-
1722 volume basaltic extrusive complexes on rifted margins. *Journal of Geophysical Research: Solid*
1723 *Earth* **105**, 19335-19351.

1724 Planke, S., Rasmussen, T., Rey, S. S., Myklebust, R. (2005). Seismic characteristics and
1725 distribution of volcanic intrusions and hydrothermal vent complexes in the Vøring and Møre basins.
1726 In: Doré, A. G. (ed.) *Petroleum Geology: North-West Europe and Global Perspectives -*
1727 *Proceddings of the 6th Petroleum Geology Conference*: Geological Society, London, 833-844.
1728 Poland, M. P., Miklius, A., Sutton, A. J. and Thornber, C. R. (2012). A mantle-driven surge in
1729 magma supply to Kilauea Volcano during 2003-2007. *Nature Geoscience* **5**(4), 295-300.
1730 Poland, M. P. & Carbone, D. (2016). Insights into shallow magmatic processes at Kīlauea Volcano,
1731 Hawai'i, from a multiyear continuous gravity time series. *Journal of Geophysical Research: Solid*
1732 *Earth* **121**, 5477-5492.
1733 Pommier, A. (2014). Interpretation of magnetotelluric results using laboratory measurements.
1734 *Surveys in Geophysics* **35**, 41-84.
1735 Pommier, A., Tarits, P., Hautot, S., Pichavant, M., Scaillet, B. & Gaillard, F. (2010). A new
1736 petrological and geophysical investigation of the present-day plumbing system of Mount
1737 Vesuvius. *Geochemistry Geophysics Geosystems* **11**, Q07013.
1738 Pommier, A. & Le Trong, E. (2011). SIGMELTS: A web portal for electrical conductivity
1739 calculations in geosciences. *Computational Geoscience* **37**, 1450-1459.
1740 Pritchard, M. E. & Simons, M. (2004). An InSAR-based survey of volcanic deformation in the
1741 central Andes. *Geochemistry, Geophysics, Geosystems* **5**(2).
1742 Prutkin, I., Vajda, P. & Gottsmann, J. (2014). The gravimetric picture of magmatic and
1743 hydrothermal sources driving hybrid unrest on Tenerife in 2004/5. *Journal of Volcanology and*
1744 *Geothermal Research* **282**, 9-18.
1745 Reeves, J., Magee, C. & Jackson, C. A. L. (2018). Unravelling intrusion-induced forced fold
1746 kinematics and ground deformation using 3D seismic reflection data. *Volcanica* **1**, 1-17.
1747 Reich, H. (1932). Die Bedeutung der finnischen Schweremessungen fur die angewandte Geophysik:
1748 Beitr. *Angew. Geophys., Erganzungsh* **2**, 1-13.

1749 Richter, C. & van der Pluijm, B.A. (1994). Separation of paramagnetic and ferrimagnetic
1750 susceptibilities using low temperature magnetic susceptibilities and comparison with high field
1751 methods. *Physics of the Earth and Planetary Interiors* **82**, 113-123.
1752 Rivalta, E. & Segall, P. (2008). Magma compressibility and the missing source for some dike
1753 intrusions. *Geophysical Research Letters* **35**(4).
1754 Roberts, J. J. & Tyburczy, J. A. (1999). Partial-melt electrical conductivity: Influence of melt
1755 composition. *Journal of Geophysical Research* **104**, 7055-7065.
1756 Rocchi, S., Mazzotti, A., Marroni, M., Pandolfi, L., Costantini, P., Giuseppe, B., Biase, D. D.,
1757 Federici, F. & Lo, P. G. (2007). Detection of Miocene saucer-shaped sills (offshore Senegal) via
1758 integrated interpretation of seismic, magnetic and gravity data. *Terra Nova* **19**, 232-239.
1759 Rochette, P., Jackson, M., Aubourg, C. (1992). Rock magnetism and the interpretation of
1760 anisotropy of magnetic susceptibility. *Reviews of Geophysics* **30**, 209-226.
1761 Roman, D. C. & Cashman, K.V. (2006). The origin of volcano-tectonic earthquake swarms.
1762 *Geology* **34**, 457-460.
1763 Roman, D. C., Savage, M. K., Arnold, R., Latchman, J. L. & De Angelis, S. (2011). Analysis and
1764 forward modeling of seismic anisotropy during the ongoing eruption of the Soufrière Hills Volcano,
1765 Montserrat, 1996–2007. *Journal of Geophysical Research: Solid Earth* **116**, B03201.
1766 Ronchin, E., Masterlark, T., Dawson, J., Saunders, S., Martì Molist, J. (2017). Imaging the complex
1767 geometry of a magma reservoir using FEM-based linear inverse modeling of InSAR data:
1768 application to Rabaul Caldera, Papua New Guinea. *Geophysical Journal International* **209**, 1746-
1769 1760.
1770 Routh, P., Neelamani, R., Lu, R., Lazaratos, S., Braaksma, H., Hughes, S., Saltzer, R., Stewart, J.,
1771 Naidu, K., Averill, H. & Gottumukkula, V. (2017). Impact of high-resolution FWI in the western
1772 black sea: Revealing overburden and reservoir complexity. *The Leading Edge* **36**, 60-66.
1773 Rubin, A. & Gillard, D. (1998). Dike-induced earthquakes: Theoretical considerations. *Journal of*
1774 *Geophysical Research* **103**, 10017-10030.

1775 Rymer, H. & Brown, G. C. (1986). Gravity fields and the interpretation of volcanic structures:
1776 Geological discrimination and temporal evolution. *Journal of Volcanology and Geothermal*
1777 *Research* **27**, 229-254.
1778 Rymer, H., Locke, C. A., Brenes, J. & Williams-Jones, G. (2005). Magma plumbing processes for
1779 persistent activity at Poas volcano, Costa Rica. *Geophysical Research Letters* **32**, L08307.
1780 Salzer, J. T., Nikkhoo, M., Walter, T. R., Sudhaus, H., Reyes-Dávila, G., Bretón, M., Arámbula, R.
1781 (2014). Satellite radar data reveal short-term pre-explosive displacements and a complex conduit
1782 system at Volcán de Colima, Mexico. *Frontiers in Earth Science* **2**, 12.
1783 Samrock, F., Kuvshinov, A., Bakker, J., Jackson, A., Fisseha, S. (2015). 3D analysis and
1784 interpretation of Magnetotelluric data from the Aluto-Langano geothermal field, Ethiopia.
1785 *Geophysical Journal International* **202**, 1923-1948
1786 Saunders, K., Blundy, J. D., Dohmen, R., Cashman, K. (2012). Linking Petrology and Seismology
1787 at an active volcano. *Science* **336**, 1023-1027.
1788 Saxby, J., Gottsmann, J., Cashman, K. & Gutiérrez, E. (2016). Magma storage in a strike-slip
1789 caldera. *Nature Communications* **7**, 12295.
1790 Schaefer, L. N., Lu, Z., Oommen, T. (2015). Dramatic volcanic instability revealed by InSAR.
1791 *Geology* **43**, 743-746.
1792 Schmeling, H. (1986). Numerical models on the influence of partial melt on elastic, anelastic and
1793 electrical properties of rocks. Part II: electrical conductivity. *Physics of Earth and Planetary*
1794 *Interiors* **43**, 123-136.
1795 Schofield, N., Stevenson, C., Reston, T. (2010). Magma fingers and host rock fluidization in the
1796 emplacement of sills. *Geology* **38**, 63-66.
1797 Schofield, N., Heaton, L., Holford, S. P., Archer, S. G., Jackson, C. A. L., Jolley, D. W. (2012a).
1798 Seismic imaging of 'broken bridges': linking seismic to outcrop-scale investigations of intrusive
1799 magma lobes. *Journal of the Geological Society of London* **169**, 421-426.

1800 Schofield, N. J., Brown, D. J., Magee, C., Stevenson, C. T. E. (2012b) Sill morphology and
1801 comparison of brittle and non-brittle emplacement mechanisms. *Journal of the Geological Society*
1802 *of London* **169**, 127-141.
1803 Schofield, N., Holford, S., Millett, J., Brown, D., Jolley, D., Passey, S., Muirhead, D., Grove, C.,
1804 Magee, C., Murray, J., Hole, M., Jackson, C., Stevenson, C. (2017). Regional Magma Plumbing and
1805 emplacement mechanisms of the Faroe-Shetland Sill Complex: Implications for magma transport
1806 and petroleum systems within sedimentary basins. *Basin Research* **29**, 41-63.
1807 Segall, P. (2010). *Earthquake and volcano deformation*. Princeton University Press.
1808 Shalev, E., Kenedi, C. L., Malin, P., Voight, V., Miller, V., Hidayat, D., Sparks, R. S. J., Minshull,
1809 T., Paulatto, M., Brown, L. & Mattioli, G. (2010). Three-dimensional seismic velocity tomography
1810 of Montserrat from the SEA-CALIPSO offshore/onshore experiment. *Geophysical Research Letters*
1811 **37**, L00E17.
1812 Sigmundsson, F., Hreinsdóttir, S., Hooper, A., Árnadóttir, T., Pedersen, R., Roberts, M.J.,
1813 Óskarsson, N., Auriac, A., Decriem, J., Einarsson, P., Geirsson, H. (2010). Intrusion triggering of
1814 the 2010 Eyjafjallajokull explosive eruption. *Nature* **468**(7322), 426-430.
1815 Sigmundsson, F. & 37 others (2015). Segmented lateral dyke growth in a rifting event at
1816 Bardabunga volcanic system, Iceland. *Nature* **517**, 191-195.
1817 Sigmundsson, F. (2016), New insights into magma plumbing along rift systems from detailed
1818 observations of eruptive behavior at Axial volcano. *Geophysical Research Letters* **43**, 12,423-
1819 12,427.
1820 Simons, M. & P. A. Rosen. (2007). Interferometric synthetic aperture radar geodesy. *Treatise on*
1821 *Geophysics - Geodesy* **3**, 391-446, Elsevier, Amsterdam.
1822 Simpson, F. & Bahr, K. (2005). *Practical Magnetotellurics*. Cambridge University Press,
1823 Cambridge, UK.

1824 Singer, B. S., Andersen, N. L., Le Mével, H., Feigl, K. L., DeMets, C., Tikoff, B., Thurber, C. H.,
1825 Jicha, B. R., Cardona, C., Córdova, L. and Gil, F. (2014). Dynamics of a large, restless, rhyolitic
1826 magma system at Laguna del Maule, southern Andes, Chile. *GSA Today* **24**, 4-10.
1827 Sirgue, L., Barkved, O. I., Dellinger, J., Etgen, J., Albertin, U., Kommedal, J. H. (2010) Full
1828 waveform inversion: the next leap forward in imaging at Valhall. *First Break* **28**, 65-70.
1829 Smallwood, J. R. & Maresh, J. (2002). The properties, morphology and distribution of igneous sills:
1830 modelling, borehole data and 3D seismic from the Faroe-Shetland area. In: Jolley, D. W. & Bell, B.
1831 R. (eds.) *The North Atlantic Igneous Province: Stratigraphy, tectonic, Volcanic and Magmatic*
1832 *Processes*: Geological Society, London, Special Publications, 271-306.
1833 Sofyan, Y., Kamah, Y., Nishijima, J., Fujimitsu, Y., Ehara, S., Fukuda, Y. & Taniguchi, M. (2011).
1834 Mass variation in outcome to high production activity in Kamojang Geothermal Field, Indonesia: A
1835 reservoir monitoring with relative and absolute gravimetry. *Earth, Planets and Space* **63**, 1157-
1836 1167.
1837 Solano, J. M. S., Jackson, M. D., Sparks, R. S. J., Blundy, J. D., Annen, C. (2012). Melt segregation
1838 in deep crustal hot zones: a mechanism for chemical differentiation, crustal assimilation and the
1839 formation of evolved magmas. *Journal of Petrology* **53**, 1999-2026.
1840 Sparks, R., Biggs, J., Neuberg, J. (2012). Monitoring volcanoes. *Science* **335**, 1310-1311.
1841 Stacey, F. D., Joplin, G., Lindsay, J. (1960). Magnetic anisotropy and fabric of some foliated rocks
1842 from S.E. Australia. *Pure Applied Geophysics* **47**, 30-40.
1843 Stankiewicz, J., Ryberg, T., Haberland, C., Natawidjaja, D. (2010). Lake Toba volcano magma
1844 chamber imaged by ambient seismic noise tomography. *Geophysical Research Letters* **37**, L17306.
1845 Stephenson, A. (1994). Distribution anisotropy: two simple models for magnetic lineation and
1846 foliation. *Physics of the Earth and Planetary Interiors* **82**, 49-53.
1847 Sternberg, B., Washburne, J. C., Pellerin, L. (1988). Correction for the static shift in
1848 magnetotellurics using transient electromagnetic soundings. *Geophysics* **53**, 1459-1468.

1849 Stevenson, C. T. E., Owens, W. H., Hutton, D. H. W. (2007a). Flow lobes in granite: the
1850 determination of magma flow direction in the Trawenagh Bay Granite, N.W. Ireland, using
1851 anisotropy of magnetic susceptibility. *Geological Society of America Bulletin* **119**, 1368-1386.
1852 Stevenson, C. T. E., Owens, W. H., Hutton, D. H. W., Hood, D. N., Meighan, I. G. (2007b).
1853 Laccolithic, as opposed to cauldron subsidence, emplacement of the Eastern Mournes pluton, N.
1854 Ireland: evidence from anisotropy of magnetic susceptibility. *Journal of the Geological Society of*
1855 *London* **164**, 99-110.
1856 Stork, A., Stuart, G. W., Henderson, C. M., Keir, D., Hammond, J. O. S. (2013). Uppermost mantle
1857 (Pn) velocity model for the Afar region, Ethiopia: An insight into rifting processes. *Geophysical*
1858 *Journal International* **193**, 321-328.
1859 Stuart, G. W., Bastow, I. D., Ebinger, C. J. (2006). Crustal structure of the Northern Main Ethiopian
1860 rift from receiver function studies. In: Yirgu, G., Ebinger, C. J., Maguire, P. K. H. (eds) The Afar
1861 Volcanic Province within the East African Rift System. *Geological Society, London, Special*
1862 *Publications* **259**, 253-267.
1863 Sturkell, E., Einarsson, P., Sigmundsson, F., Geirsson, H., Olafsson, H., Pedersen, R., de Zeeuw-
1864 van Dalfsen, E., Linde, A.T., Sacks, S.I., Stefánsson, R. (2006). Volcano geodesy and magma
1865 dynamics in Iceland. *Journal of Volcanology and Geothermal Research* **150**, 14-34.
1866 Svensen, H., Corfu, F., Polteau, S., Hammer, Ø., Planke, S. (2012). Rapid magma emplacement in
1867 the Karoo Large Igneous Province. *Earth and Planetary Science Letters* **325-326**, 1-9.
1868 Symonds, P. A., Planke, S., Frey, O., Skogseid, J. (1998). Volcanic evolution of the Western
1869 Australian Continental Margin and its implications for basin development. *The Sedimentary Basins*
1870 *of Western Australia 2: Proc. of Petroleum Society Australia Symposium, Perth, WA*.
1871 Takada, Y. & Fukushima, Y. (2013). Volcanic subsidence triggered by the 2011 Tohoku earthquake
1872 in Japan. *Nature Geoscience* **6**(8), 637-641.
1873 Takei, Y. (2002). Effect of pore geometry on V-P/V-S: From equilibrium geometry to crack.
1874 *Journal of Geophysical Research-Solid Earth* **107**, 2043.

1875 Tarantola, A. (1984) Inversion of seismic reflection data in the acoustic approximation. *Geophysics*
1876 **49**, 1259-1266.
1877 Tarling, D. H. & Hrouda, F. (1993). The Magnetic Anisotropy of Rocks, Chapman and Hall, New
1878 York, pp. 1-232.
1879 Tauxe, L. (1998). Paleomagnetic Principles and Practice. In: Of Modern approaches in geophysics,
1880 vol. 17: Kluwer Academic Publishers, Dordrecht, Boston, London.
1881 Thiele, S., Micklethwaite, S., Bourke, P., Verrall, M., Kovesi, P. (2015). Insights into the mechanics
1882 of en-echelon sigmoidal vein formation using ultra-high resolution photogrammetry and computed
1883 tomography. *Journal of Structural Geology* **77**, 27-54.
1884 Thomas, M. E. & Neuberg, J. (2012). What makes a volcano tick - A first explanation of deep
1885 multiple seismic sources in ascending magma. *Geology* **40**, 351-354.
1886 Thomson, K. (2007). Determining magma flow in sills, dykes and laccoliths and their implications
1887 for sill emplacement mechanisms. *Bulletin of Volcanology* **70**, 183-201.
1888 Thomson, K. & Hutton, D. (2004). Geometry and growth of sill complexes: insights using 3D
1889 seismic from the North Rockall Trough. *Bulletin of Volcanology* **66**, 364-375.
1890 Tizzani, P., Battaglia, M., Zeni, G., Atzori, S., Berardino, P. & Lanari, R. (2009). Uplift and magma
1891 intrusion at Long Valley caldera from InSAR and gravity measurements. *Geology* **37**, 63-66.
1892 Tolstoy, M., Waldhauser, F., Bohnenstiehl, D. R., Weekly, R. T., Kim, W. -Y. (2008). Seismic
1893 identification of along-axis hydrothermal flow on the East Pacific Rise. *Nature* **451**, 181-184.
1894 Trasatti, E., Giunchi, C.& Agostinetti, N. P. (2008). Numerical inversion of deformation caused by
1895 pressure sources: application to Mount Etna (Italy). *Geophysical Journal International* **172**, 873-
1896 884.
1897 Trindade, R. I. F., Nguema, T. M. M., Bouchez, J. L. (2001). Thermally enhanced mimetic fabric of
1898 magnetite in a biotite granite. *Geophysical Research Letters* **28**, 2687-2690.
1899 Trude, J., Cartwright, J., Davies, R. J. & Smallwood, J. (2003). New technique for dating igneous
1900 sills. *Geology* **31**, 813-816.

1901 Tuffen, H., Smith, R., Sammonds, P. R. (2008). Evidence for seismogenic fracture of silicic
1902 magma. *Nature* **453**, 511-514.
1903 Van Camp, M., de Viron, O., Watlet, A., Meurers, B., Francis, O. & Caudron, C. (2017).
1904 Geophysics trom terrestrial time-variable gravity measurements. *Reviews of Geophysics* **55**, 938-
1905 992
1906 Vargas-Bracamontes, D. M. & Neuberg, J. W. (2012). Interaction between regional and magma-
1907 induced stresses and their impact on volcano-tectonic seismicity. *Journal of Volcanology and*
1908 *Geothermal Research* **243**, 91-96.
1909 Vasuki, Y., Holden, E. -J., Kovesi, P., Micklethwaite, S. (2014) Semi-automatic mapping of
1910 geological Structures using UAV-based photogrammetric data: An image analysis approach.
1911 *Computers and Geosciences* **69**, 22-32.
1912 Vasuki, Y., Holden, E. -J., Kovesi, P., Micklethwaite, S. (2017). An interactive image segmentation
1913 method for lithological boundary detection: A rapid mapping tool for geologists. *Computers and*
1914 *Geosciences* **100**, 27-40.
1915 Verwey, E. J. W. (1939). Electronic conduction of magnetite (Fe3O4) and its transition point at low
1916 temperatures. *Nature* **144**, 327-328.
1917 Vigh, D., Starr, B., Kapoor, J., Li, H. (2010) 3D full waveform inversion on a GOM data set. *80th*
1918 *Annual International Meeting, SEG, Expanded Abstracts*.
1919 Vigneresse, J. L. (1995). Crustal regime of deformation and ascent of granitic magma.
1920 *Tectonophysics* **249**, 187-202.
1921 Vigneresse, J. L., Tikoff, B. & Améglio, L. (1999). Modification of the regional stress field by
1922 magma intrusion and formation of tabular granitic plutons. *Tectonophysics* **302**, 203-224.
1923 Voigt, W. & Kinoshita, S. (1907). Bestimmung absoluter Werte von Magnetisierungszahlen,
1924 insbesondere für Kristalle. *Annalen der Physik* **329**, 492-514.

Vollgger, S. A. & Cruden, A. R. (2016). Mapping folds and fractures in basement and cover rocks using UAV photogrammetry, Cape Liptrap and Cape Paterson, Victoria, Australia. *Journal of Structural Geology* **85**, 168-187.

Waite, G. P. & Moran, S. C. (2009). VP Structure of Mount St. Helens, Washington, USA, imaged with local earthquake tomography. *Journal of Volcanology and Geothermal Research* **182**, 113-122.

Wall, M., Cartwright, J., Davies, R. & McGrandle, A. (2010). 3D seismic imaging of a Tertiary Dyke Swarm in the Southern North Sea, UK. *Basin Research* **22**, 181-194.

Wannamaker, P. E., Hasterok, D. P., Johnston, J. M., Stodt, J. A., Hall, D. B., Sodergren, T. L., Pellerin, L., Maris, V., Doerner, W. M., Groenewold, K. A., Unsworth, M. J. (2008). Lithospheric dismemberment and magmatic processes of the Great Basin–Colorado Plateau transition, Utah, implied from magnetotellurics. *Geochemistry, Geophysics, Geosystems* **9**, Q05019.

Ward, K. M., Zandt, G., Beck, S. L., Christensen, D. H. & McFarlin, H. (2014). Seismic imaging of the magmatic underpinnings beneath the Altiplano-Puna volcanic complex from the joint inversion of surface wave dispersion and receiver functions. *Earth and Planetary Science Letters* **404**, 43-53.

Warner, M., Ratclie, A., Nangoo, T., Morgan, J., Umpleby, A., Shah, N., Vinje, V., Stekl, I., Guasch, L., Win, C., Conroy, G., Bertrand, A. (2013). Anisotropic 3D full-waveform inversion. *Geophysics* **78**, R59-R80.

Wauthier, C., Roman, D. C., Poland, M. P. (2013). Moderate-magnitude earthquakes induced by magma reservoir inflation at Kīlauea Volcano, Hawaii. *Geophysical Research Letters* **40**(20), 5366-5370.

Wawrzyniak, P., Zlotnicki, J., Sailhac, P. Marquis, G. (2017). Resistivity variations related to the large March 9, 1998 eruption at La Fournaise volcano inferred by continuous MT monitoring. *Journal of Volcanology and Geothermal Research* **347**, 185-206.

Weaver, J. (1994). *Mathematical methods for geo-electromagnetic induction*. Research Studies Press.

Westoby, M. J., Brasington, J., Glasser, N. F., Hambrey, M. J., Reynolds, J. M. (2012). "Structure-from-Motion" photogrammetry: A low-cost, effective tool for geoscience applications. *Geomorphology* **179**, 300-314.

Whaler, K. A. & Hautot, S. (2006). The electrical resistivity structure of the crust beneath the northern Main Ethiopian Rift. In: Yirgu, G., Ebinger, C. J., Maguire, P. K. H. (eds) The Afar Volcanic Province within the East African Rift System. *Geological Society, London, Special Publications* **259**, 293-305.

White, R. & McCausland, W. (2016). Volcano-tectonic earthquakes: A new tool for estimating intrusive volumes and forecasting eruptions. *Journal of Volcanology and Geothermal Research* **309**, 139-155.

Wicks, C.W., Thatcher, W., Dzurisin, D., Svarc, J. (2006). Uplift, thermal unrest and magma intrusion at Yellowstone caldera. *Nature* **440**(7080), 72-75.

Yamasaki, T., Kobayashi, T., Wright, T. J., Fukahata, Y. (2018). Viscoelastic crustal deformation by magmatic intrusion: A case study in the Kutcharo caldera, eastern Hokkaido, Japan. J*ournal of Volcanology and Geothermal Research* **349**, 128-145.

Zandomeneghi, D., Aster, R., Kyle, P., Barclay, A., Chaput, J., Knox, H. (2013). Internal structure of Erebus volcano, Antarctica imaged by high-resolution active-source seismic tomography and coda interferometry. *Journal of Geophysical Research-Solid Earth* **118**, 1067–1078.

7. Figure captions

Figure 1: Schematic of a vertically extensive, transcrustal magma plumbing system involving transient, interconnected, relatively low-volume tabular magma intrusions (e.g., dykes, sills, and laccoliths) within a crystal mush (based on Cashman *et al.,* 2017; Cruden *et al.,* 2018).

1975 Figure 2: (A) Interferograms showing fringes caused by the pressurisation of a point source directly
1976 beneath a stratovolcano from both ascending and descending satellite lines of sight. Note that the
1977 centre of the fringes are slightly offset from the summit of the volcano (marked by a black triangle).
1978 (B) Typical fringe patterns for analytical deformation sources in an elastic half space from
1979 ascending satellite geometry: (i) Mogi source at 5 km depth; (ii) dyke extending between depths of
1980 3 and 9 km; (iii) rectangular sill; and (iv) a penny-shaped horizontal crack both at 5 km depth.
1981
1982 Figure 3: (A) Ascending line of sight (LOS) co-eruptive interferogram from the 2008 basalt lava
1983 extrusion between the Alu and Alu South domes and the Dalafilla stratovolcano (modified from
1984 Pagli *et al.,* 2012). (B) Inversion of uplift and subsidence patterns, recorded by InSAR during the
1985 2008 basalt lava eruption at the Alu dome in the Danakil Depression, suggested ground deformation
1986 could be attributed to a combination of: (i) deflation of a reservoir, modelled as a Mogi source, at
1987 ~4 km depth; (ii) inflation and deflation of a tabular sill at ~1 km depth; and (iii) opening of a dyke
1988 beneath the eruptive fissure (Figs 3A and B) (Pagli *et al.,* 2012). See Figure 3A for location. (C)
1989 Geological map showing that lava flows radiate out from Alu and originate from the periphery of
1990 the dome, which is cross-cut by an array of randomly oriented faults (modified from Magee *et al.,*
1991 2017). (D) Magee *et al.,* (2017) inferred Alu is underlain by a saucer-shaped sill plumbing system,
1992 based on field observations and comparison to seismic reflection data, not a tabular sill (Fig. 3B).
1993
1994 Figure 4: Example of integrating seismology and petrology to constrain time-scales of magma
1995 storage and recharge (from Saunders *et al.,* 2012). Calculated Fe-Mg diffusion time scales of
1996 orthopyroxene crystals compared to monitoring data for the same eruptive period for Mount St.
1997 Helens. (A) The seismic record of depth against time of the 1980–1986 eruption sequence. (B)
1998 Measured flux of SO_2 gas. (C) Calculated age of orthopyroxene rim growth binned by month for the
1999 entire population. The age recorded is the month in which the orthopyroxene rim growth was
2000 triggered by magmatic perturbation. The black line displays the running average (over five points,

2001 equivalent to the average calculated uncertainty in calculated time scales) of all the data. The peaks
2002 in the diffusion time series correspond to episodes of deep seismicity in 1980 and 1982 and to
2003 elevated SO_2 flux in 1980 and possibly 1982. (D) Running average of the orthopyroxene rim time
2004 scales, displaying reverse zonation (Mg-rich rims) in blue and normal zonation (Fe-rich rims) in
2005 green. There are reverse zonation peaks in the early 1980, probably due to rejuvenation of the
2006 magma system by hotter pulses, whereas Fe-rich rims are more dominant from 1982 on. Vertical
2007 dashed grey lines represent the volcanic eruptions.
2008
2009 Figure 5: Plot of melt inclusion saturation and earthquake hypocentre depths, which suggest magma
2010 storage occurred at 1–5 km depths, beneath the Dabbahu volcanic system in Afar, Ethiopia
2011 (modified from Field *et al.,* 2012). Melt inclusion data obtained from analyses of alkali feldspar,
2012 clinopyroxene, and olivine phenocrysts within Dabbahu lavas <8 Kyr (Field *et al.,* 2012).
2013 Earthquake data recorded during the 2005 dyke event (Ebinger *et al.,* 2008).
2014
2015 Figure 6: (A) P-wave (V_p) tomography beneath Montserrat (black outline), highlighting the location
2016 of fast and slow seismic velocity anomalies (i.e. >6% faster or slower than average) relative to the
2017 location of the Silver Hills (SH), Central Hills (CH), and Soufrière Hills (SHV) volcanoes
2018 (modified from Shalev *et al.,* 2010). The fast velocity anomalies, interpreted to represent solidified
2019 andesitic intrusions underlie the volcanoes (Shalev *et al.,* 2010).
2020
2021 Figure 7: Static and dynamic gravimetric investigations of two active silicic magmatic systems in
2022 the Andes: Uturuncu volcano (Bolivia; A, C, and E) and the Laguna del Maule volcanic field
2023 (Chile; B, D, and F). (A) 3D view of the isosurface corresponding to the -120 kg m^3 density contrast
2024 beneath Uturuncu volcano, derived from Bouguer gravity data, interpreted to reflect a large (~750
2025 km^3) plumbing system composed of a lower (<-10 km) partially molten reservoir and upper,
2026 fractured and fluid-bearing solidified intrusions above sea level (after del Potro *et al.,* 2013). (B) 3D

2027 view of the -600 kg m^3 density contrast isosurface beneath the Laguna del Maule, which is
2028 interpreted to define a magma reservoir (>50 % melt) within a larger region of a crystal mush
2029 system; the 2D planes show slices through the dataset (Miller *et al.,* 2017). Elevation above sea
2030 level (a.s.l.) shown. See Figure 7D for area of data coverage. (C) Map of the 55 km long, dynamic
2031 gravity network (white circles) installed to track changes in gravity over time and space at Uturuncu
2032 volcano between 2010 and 2013 (modified from Gottsmann *et al.,* 2017). (D) Spatio-temporal
2033 residual gravity changes at Laguna del Maule recorded from 2013–2014, after correcting for
2034 deformation effects (modified from Miller *et al.,* 2017). (E) Gravity and deformation data, recorded
2035 from Uturuncu from 2010–2013, plotted against the measured free-air gravity gradient (solid red
2036 line) and associated errors (broken red lines) (modified from Gottsmann *et al.,* 2017). The data
2037 follow the gradient and are indicative of a subsurface density change as a cause of the uplift,
2038 possibly reflecting the release of fluids from a large deep-seated magma reservoir (i.e. the
2039 Altiplano-Puna Magmatic Body; Chmielowski *et al.,* 1999) through the vertically extensive crystal
2040 mush system shown in (A) (Gottsmann *et al.,* 2017). (F) Plot of gravity against horizontal distance
2041 for the source centre at Laguna del Maule (modified from Miller *et al.,* 2017). The increase in
2042 gravity of up to 120 µGal is explained by a hydrothermal fluid injection focused along a fault
2043 system, shown in (D), at 1.5–2 km depth as a result of a deeper seated magma injection, and is best
2044 modelled by a vertical rectangular prism source.
2045
2046 Figure 8: Gravity changes and deformation at the restless Long Valley caldera. (A) Map of the
2047 Long Valley caldera, California, USA, which hosts a resurgent dome (black outline), to highlight
2048 changes in residual gravity between 1982 and 1999 (modified from Tizzani *et al.,* 2009). (B) Plot of
2049 ground uplift and residual gravity changes with radial distance from the centre of the resurgent
2050 dome in (A) (modified from Tizzani *et al.,* 2009). The correlation between uplift and positive
2051 gravity residuals across the resurgent dome indicates ground deformation was instigated by
2052 intrusion of magma (Tizzani *et al.,* 2009).

2053

2054 Figure 9: (A) Map showing MT stations deployed around Volcán Uturuncu (U) and Volcán
2055 Quetena (Q), relative to areas of uplift and subsidence (modified from Comeau *et al.,* 2015). The
2056 white box shows area of modelled 3D MT data (Comeau *et al.,* 2015). (B) Regional 2D
2057 magnetotelluric line through the Altiplano-Puna magma body (APMB) highlighting the position of
2058 Volcán Uturuncu (modified from Comeau *et al.,* 2015). The APMB corresponds to a large,
2059 conducive (i.e. low-resistivity) body (Comeau *et al.,* 2015; Comeau *et al.,* 2016). Above the APMB
2060 are other areas of low-resistivity (e.g., C4) that are likely upper crustal magma reservoirs and dykes
2061 (Comeau *et al.,* 2016). C1–C7 and R1–R2 identify discrete zones of marked conductivity or
2062 resistivity, respectively (see Comeau *et al.,* 2015; Comeau *et al.,* 2016 for details). The white box
2063 shows area of modelled 3D MT data (Comeau *et al.,* 2015). See Figure 9A for location.

2064

2065 Figure 10: (A) Interpreted seismic section and geological map showing the distribution of and
2066 connectivity between sills within the Faroe-Shetland Basin (modified from Schofield *et al.,* 2017).
2067 Mapping of magma flow patterns within individual sills reveals that the sill-complex facilitates
2068 extensive vertical and lateral magma transport. Magma was fed into the sedimentary basin via
2069 basement-involved faults. TWT = two-way travel time. (B) Interpreted seismic section and
2070 geological map describing the spatial relationship between volcanoes/vents and sills, inferred to
2071 represent the magma plumbing system, emplaced at ~42 Ma (modified from Jackson *et al.,* 2013;
2072 Magee *et al.,* 2013a). Sills are laterally offset from the volcanoes/vents summits. No 'magma
2073 chambers' are observed in the seismic data, which images down to ~8 s TWT (i.e. ~>10 km)
2074 (Magee *et al.,* 2013a).

2075

2076 Figure 11: (A) Interpreted seismic section from the Exmouth Sub-basin offshore NW Australia,
2077 which images a saucer-shaped sill that is overlain by a forced fold and feeds a small vent from its
2078 inclined limb (modified from Magee *et al.,* 2013b). See Figure 11B for line location). (B) Time-

structure map of the folded horizon (thick black line) in (A), highlighting fault traces and vent locations and thicknesses (modified from Magee *et al.,* 2013b). (C) Seismic section from the Farsund Basin, offshore southern Norway, which images part of a dyke-swarm that has been rotated by basin flexure post-emplacement (modified from Phillips et al., 2017).

Figure 12: (A) At the sample scale, all magnetic grains create a magnetic fabric. (i) Dominantly prolate fabric, where K_2 and K_3 are least certain and form a girdle. Only the magnetic lineation (K_1) can be confidently determined. (ii) When $K_1>K_2>K_3$, both a foliation (K_1–K_2) and a lineation (K_1) may be discerned, defining a triaxial fabric. (iii) When K_1 and K_2 are equally uncertain and form a girdle, K_3 is perpendicular to a foliation. (B) Schematic representation of how magma flow within a planar sheet intrusion can produce imbricated magnetic fabrics at its margins, the closure of which define the magma flow direction (after Féménias *et al.,* 2004). (C) AMS data and interpretations from part of the Trawenagh Bay Granite, NW Ireland (adapted from Stevenson *et al.,* 2007a). (i) AMS foliation traces are shown in blue and lineation traces in red. Lobes were defined in this intrusion based on foliations curving around a lineation axis. In some lobes, the magnetic lineation trend was parallel to this axis, whilst in others they tended to splay or converge down flow. (ii) 3D sketch showing the geometry of three of the lobes (numbered in part i).

Figure 13: (A) Starting model derived from smoothed, pre-stack, time-migrated (PSTM) stacking velocities. (B) Final 2D FWI-derived velocity model obtained using 10 km streamer data and inversion frequencies of between 2.5 and 24 Hz. (C) FWI velocity model overlain by the 2D pre-stack, depth-migrated (PSDM) section. Strong irregular reflections in the lower half of the section are from basaltic intrusions, which appear as high-velocity anomalies in the FWI velocity model. Both the FWI velocity model and the PSDM pick out a major unconformity, and show shallow channels in the upper parts of the section (redrawn from Kalincheva *et al.,* 2017).

Figure 14: (A) UAV orthophotograph of the wave cut platform at Bingie Point, NSW, Australia showing the distribution of Palaeogene dolerite (Dol) and dacite (Dac) dykes within Devonian tonalite (Ton), diorite (Di), and aplite (Ap) host rocks. (B) Circular histogram of joint sets measured in the Devonian rocks from the orthophotograph; the dominant (purple) set is parallel to and likely contemporaneous with the Palaeogene dykes. (C) Annotated close-up image highlighting dykes and structural features. The northern dacite dyke shows two broken bridge (BB) structures, whilst the central dolerite dyke displays prominent step structures (S). Narrow apophyses are also associated with the broken bridges and steps.

Figure 1

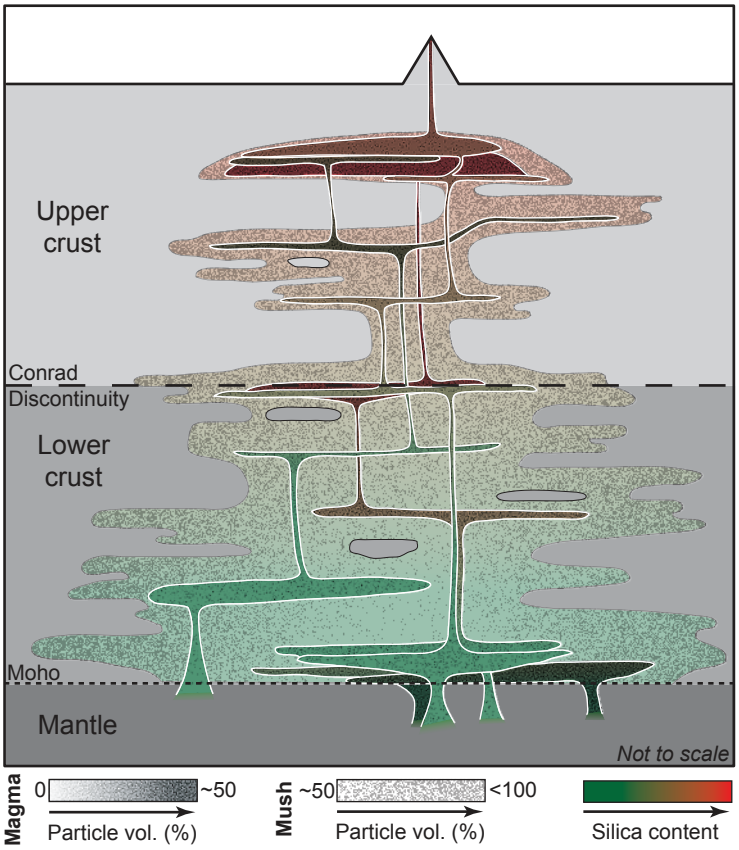
Upper
crust
Conrad
Discontinuity
Lower
crust
Moho
Mantle
Not to scale
Magma
0
~50
Particle vol. (%)
Mush
~50
<100
Particle vol. (%)
Silica content

Figure 2

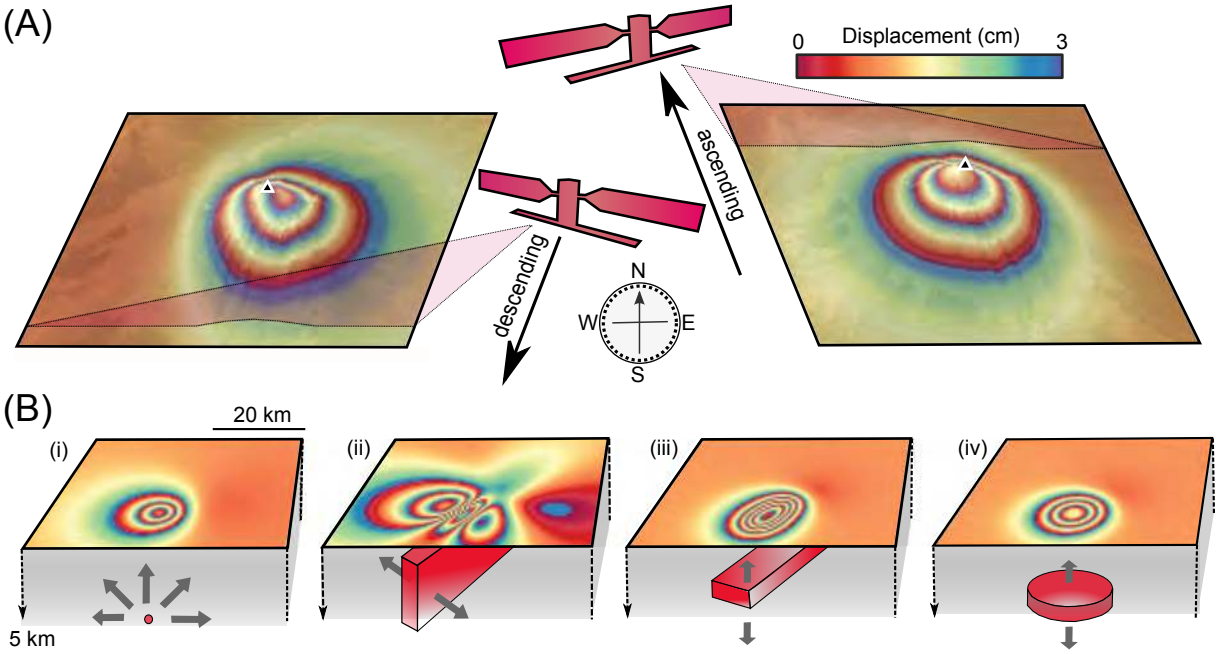
(A)
0
Displacement (cm)
3
ascending
descending
N
W
E
S
(B)
20 km
(i)
(ii)
(iii)
(iv)
5 km

Figure 3

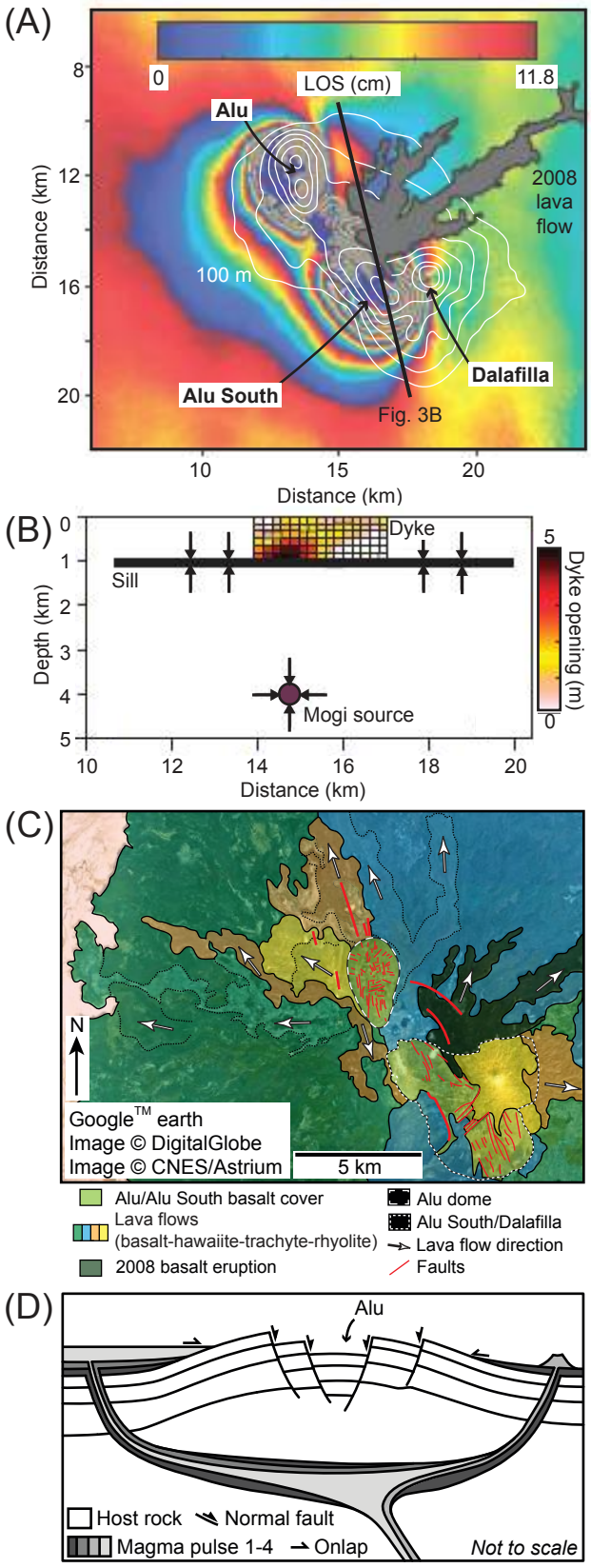
(A)
0
LOS (cm)
11.8
Alu
2008
lava
flow
100 m
Alu South
Dalafilla
Fig. 3B
Distance (km)
Distance (km)
(B)
Dyke
Sill
Mogi source
Depth (km)
Dyke opening (m)
Distance (km)
(C)
N
Google™ earth
Image © DigitalGlobe
Image © CNES/Astrium
5 km
Alu/Alu South basalt cover
Lava flows
(basalt-hawaiite-trachyte-rhyolite)
2008 basalt eruption
Alu dome
Alu South/Dalafilla
Lava flow direction
Faults
(D)
Alu
Host rock
Normal fault
Magma pulse 1-4
Onlap
Not to scale

Figure 4

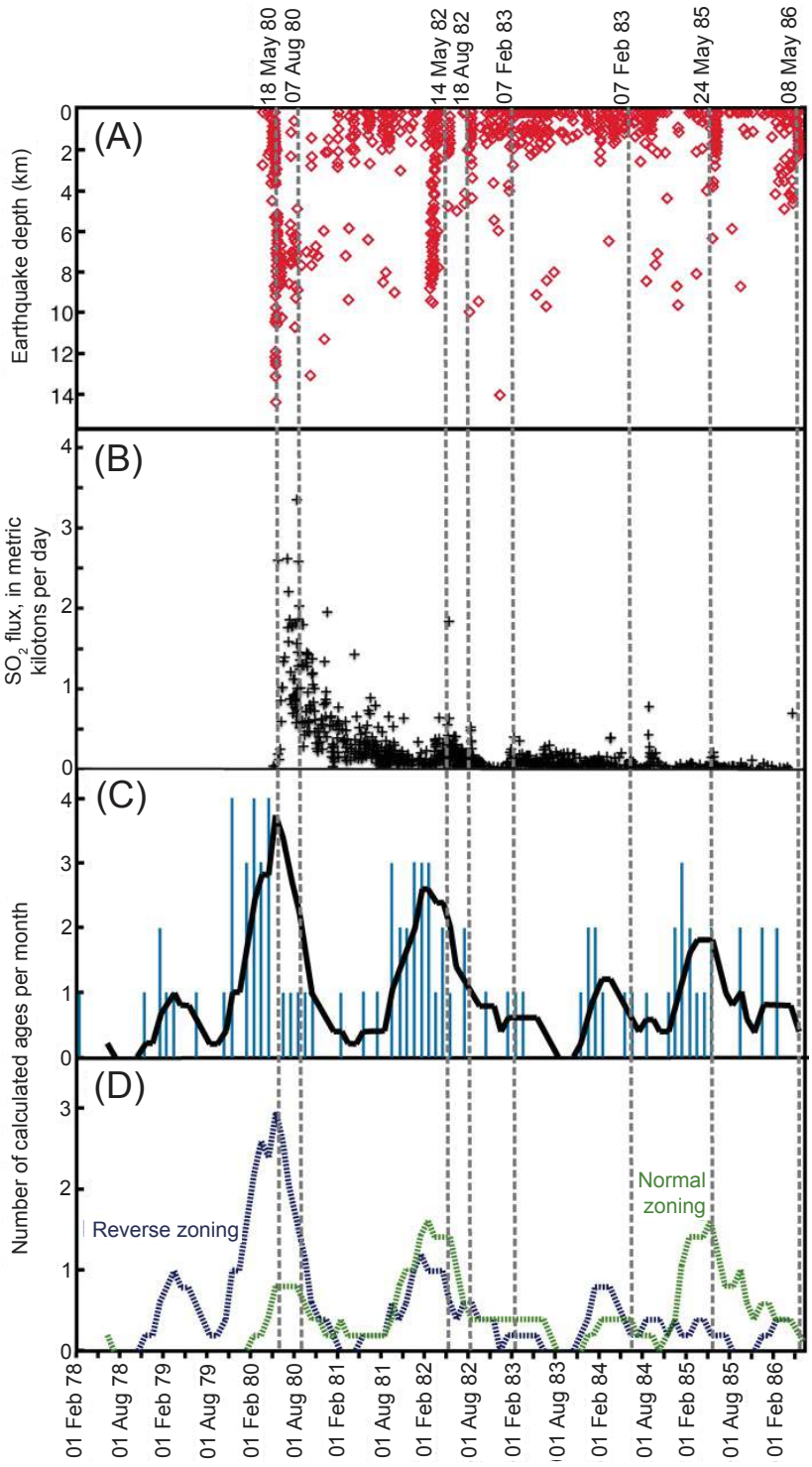
18 May 80
07 Aug 80
14 May 82
18 Aug 82
07 Feb 83
07 Feb 83
24 May 85
08 May 86
(A)
Earthquake depth (km)
(B)
SO2 flux, in metric kilotons per day
(C)
Number of calculated ages per month
(D)
Reverse zoning
Normal zoning
01 Feb 78
01 Aug 78
01 Feb 79
01 Aug 79
01 Feb 80
01 Aug 80
01 Feb 81
01 Aug 81
01 Feb 82
01 Aug 82
01 Feb 83
01 Aug 83
01 Feb 84
01 Aug 84
01 Feb 85
01 Aug 85
01 Feb 86

Figure 5

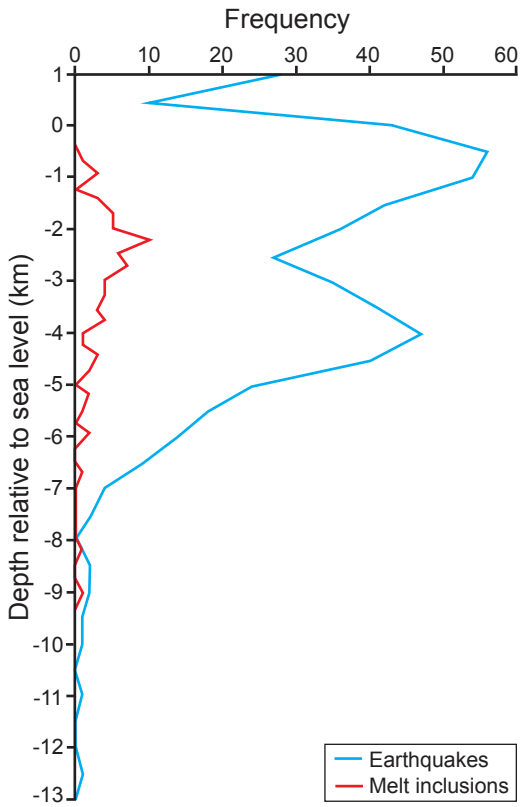
Frequency
0
10
20
30
40
50
60
1
0
-1
-2
-3
-4
-5
-6
-7
-8
-9
-10
-11
-12
-13
Depth relative to sea level (km)
Earthquakes
Melt inclusions

Figure 6

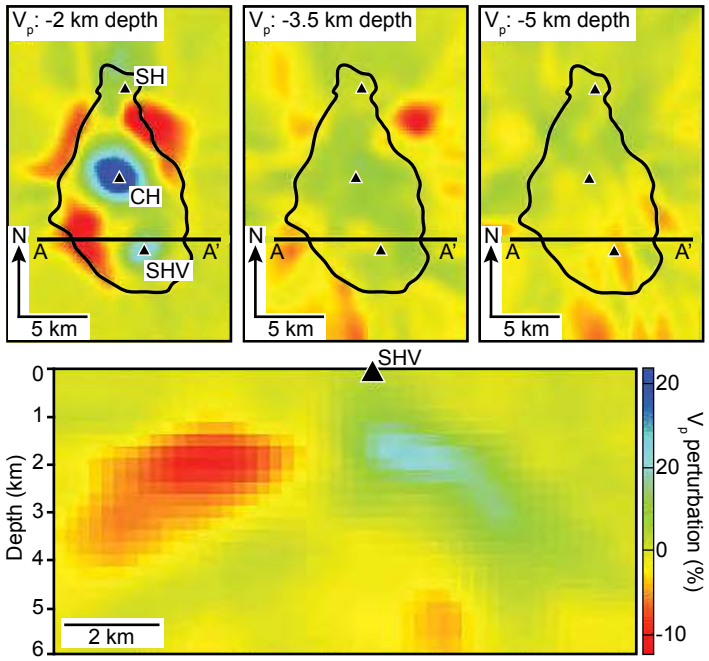
V_p: -2 km depth
SH
CH
N
A
A'
SHV
5 km
V_p: -3.5 km depth
N
A
A'
5 km
V_p: -5 km depth
N
A
A'
5 km
SHV
Depth (km)
0
1
2
3
4
5
6
2 km
20
20
0
-10
V_p perturbation (%)

Figure 7

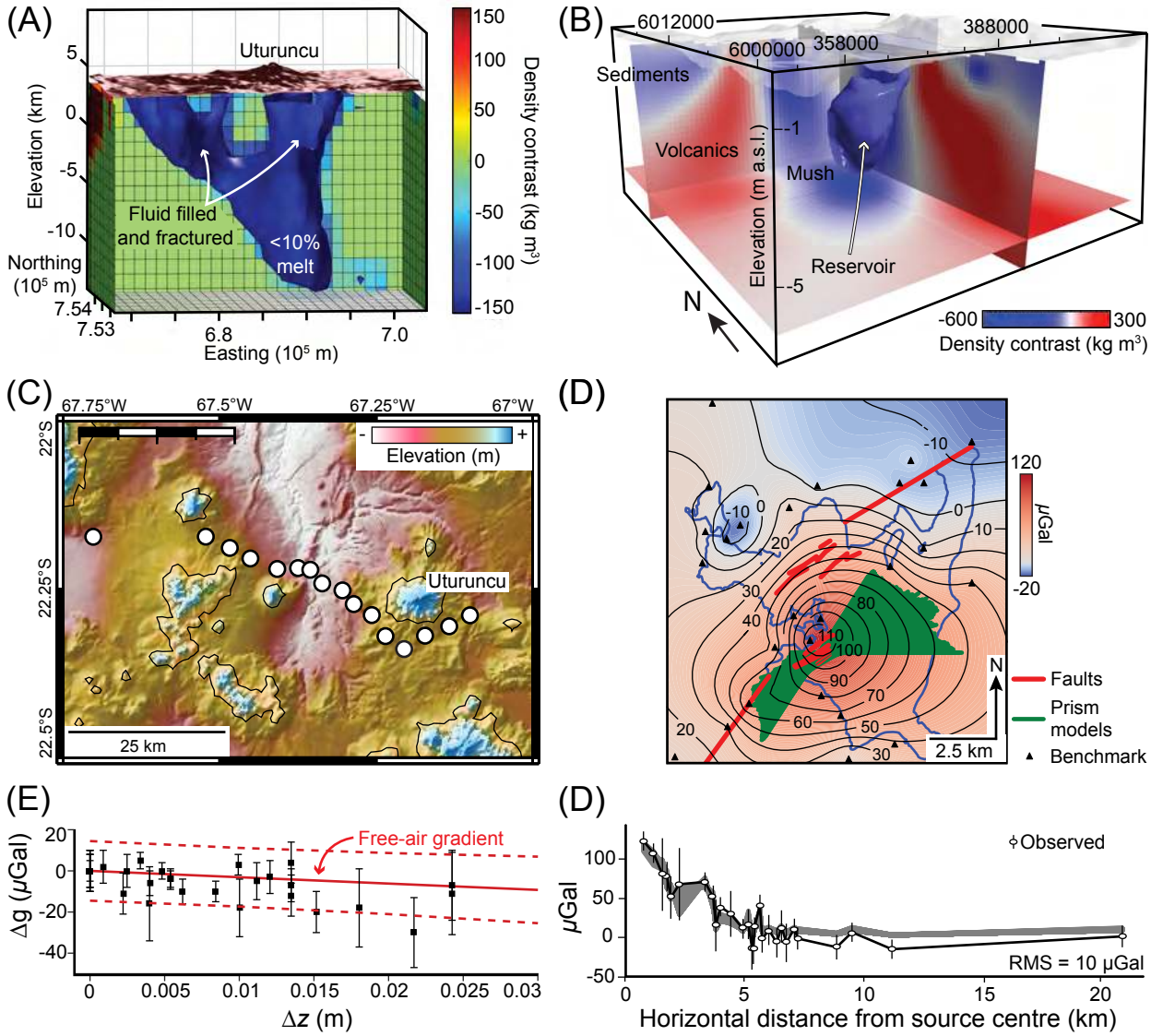
(A)
Uturuncu
Elevation (km)
Fluid filled and fractured
<10% melt
Northing (10⁵ m)
Easting (10⁵ m)
Density contrast (kg m³)
(B)
Sediments
Volcanics
Mush
Reservoir
Elevation (m a.s.l.)
N
Density contrast (kg m³)
(C)
Elevation (m)
Uturuncu
25 km
(D)
Faults
Prism models
Benchmark
2.5 km
(E)
Free-air gradient
Δg (μGal)
Δz (m)
(D)
Observed
μGal
RMS = 10 μGal
Horizontal distance from source centre (km)

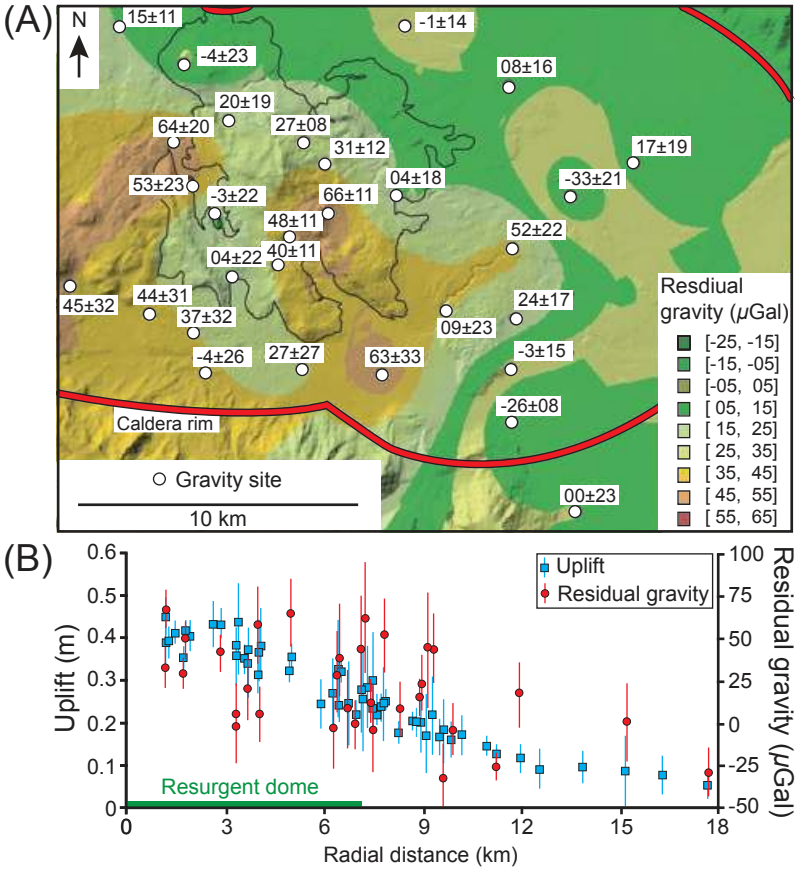
(A)
N
15±11
-1±14
-4±23
08±16
20±19
64±20
27±08
31±12
17±19
53±23
-3±22
66±11
04±18
-33±21
48±11
52±22
04±22
40±11
45±32
44±31
24±17
37±32
09±23
-4±26
27±27
63±33
-3±15
-26±08
Caldera rim
Gravity site
10 km
00±23
Resdiual gravity (μGal)
[-25, -15]
[-15, -05]
[-05, 05]
[05, 15]
[15, 25]
[25, 35]
[35, 45]
[45, 55]
[55, 65]
(B)
Uplift
Residual gravity
Resurgent dome
Uplift (m)
Residual gravity (μGal)
Radial distance (km)
0
0.1
0.2
0.3
0.4
0.5
0.6
-50
-25
0
25
50
75
100
0
3
6
9
12
15
18

Figure 9

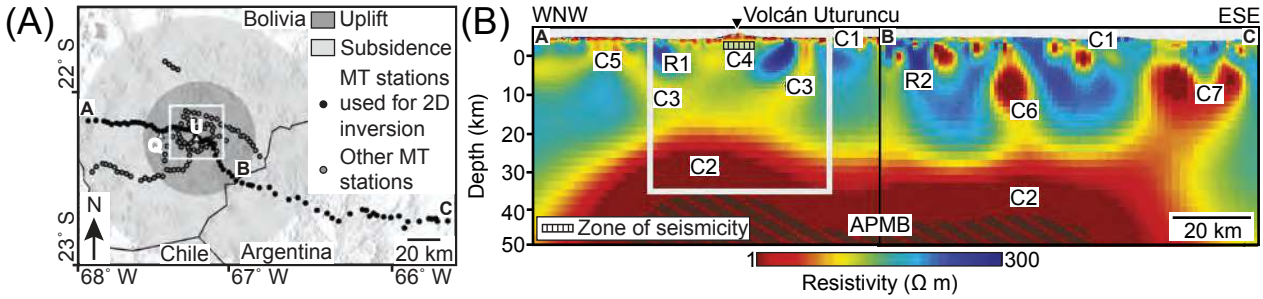
(A)
Bolivia
Uplift
Subsidence
MT stations used for 2D inversion
Other MT stations
22° S
23° S
A
B
C
N
Chile
Argentina
20 km
68° W
67° W
66° W
(B)
WNW
Volcán Uturuncu
ESE
Depth (km)
0
10
20
30
40
50
C1
C2
C3
C4
C5
C6
C7
R1
R2
Zone of seismicity
APMB
20 km
1
300
Resistivity (Ω m)

Figure 9

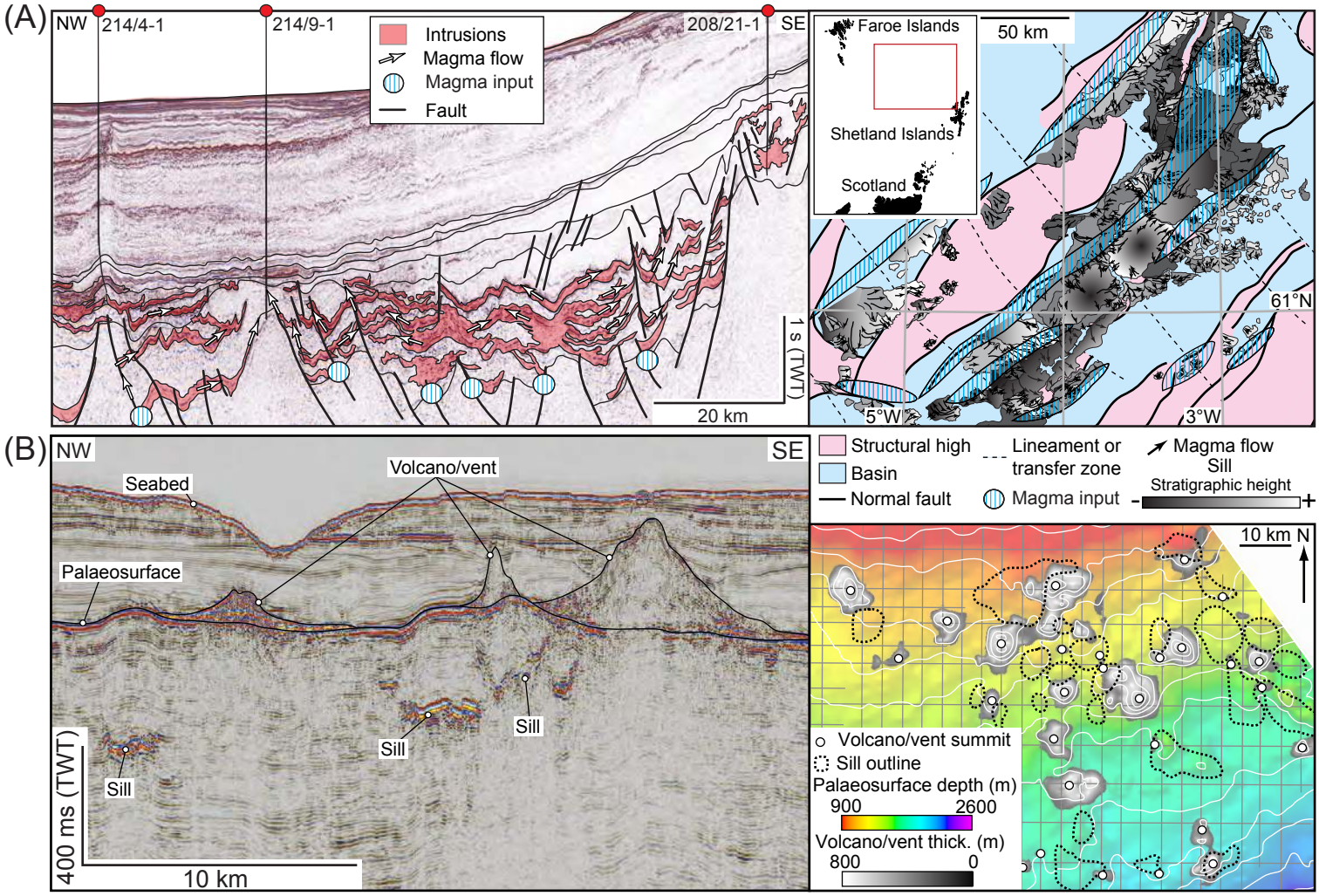
(A)
NW
214/4-1
214/9-1
208/21-1
SE
Intrusions
Magma flow
Magma input
Fault
1 s (TWT)
20 km
Faroe Islands
Shetland Islands
Scotland
50 km
61°N
5°W
3°W
(B)
NW
SE
Seabed
Volcano/vent
Palaeosurface
Sill
Sill
Sill
400 ms (TWT)
10 km
Structural high
Basin
Normal fault
Lineament or transfer zone
Magma input
Magma flow
Sill
Stratigraphic height
-
+
10 km
N
Volcano/vent summit
Sill outline
Palaeosurface depth (m)
900
2600
Volcano/vent thick. (m)
800
0

Figure 10

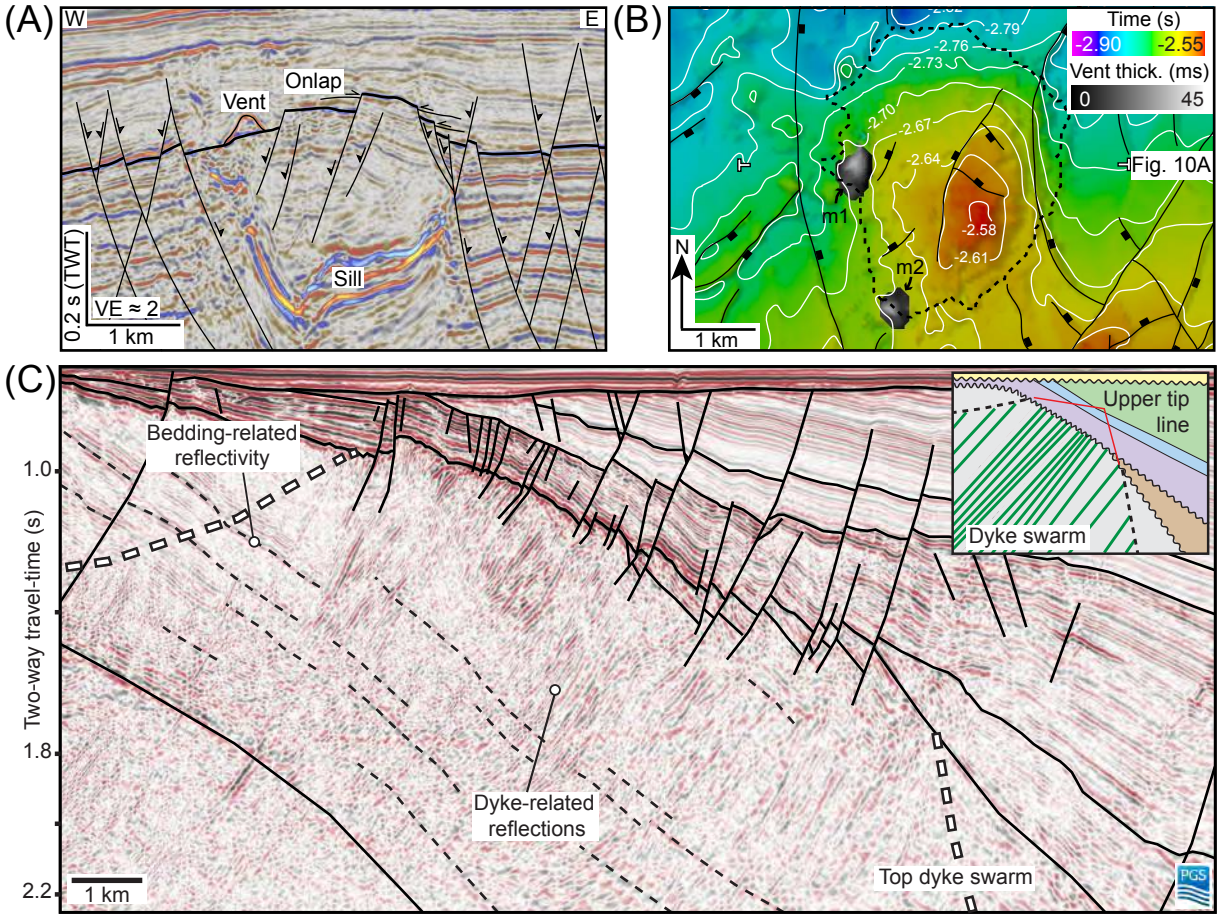
(A)
W
E
Onlap
Vent
Sill
0.2 s (TWT)
VE ≈ 2
1 km
(B)
Time (s)
-2.90
-2.55
Vent thick. (ms)
0
45
-2.79
-2.76
-2.73
-2.70
-2.67
-2.64
-2.58
-2.61
m1
m2
Fig. 10A
N
1 km
(C)
Bedding-related reflectivity
Upper tip line
Dyke swarm
Two-way travel-time (s)
1.0
1.8
2.2
Dyke-related reflections
Top dyke swarm
1 km
PGS

Figure 11

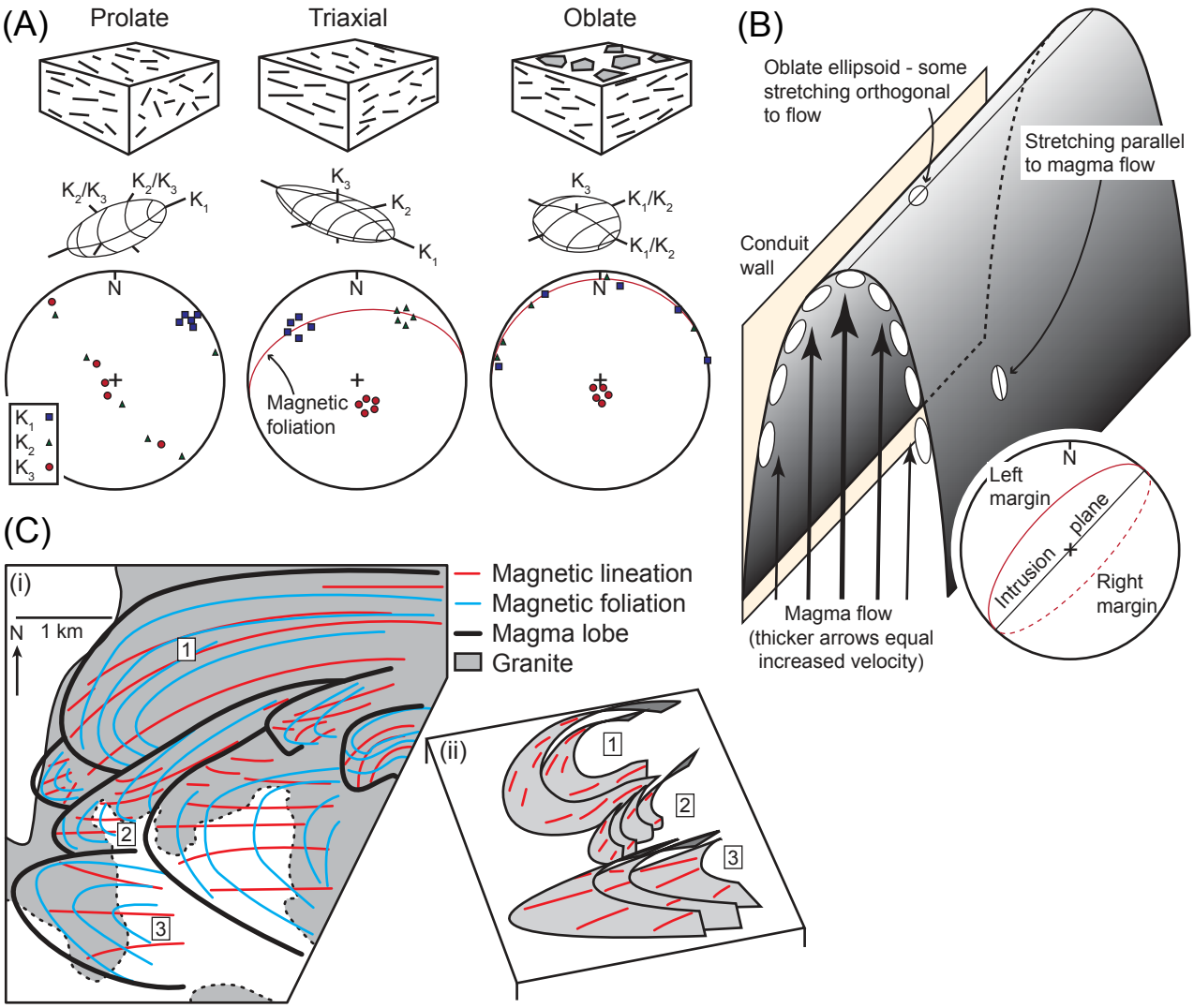
(A)
Prolate
Triaxial
Oblate
K2/K3
K2/K3
K1
K3
K2
K1
K3
K1/K2
K1/K2
N
N
N
Magnetic foliation
K1
K2
K3
(B)
Oblate ellipsoid - some stretching orthogonal to flow
Stretching parallel to magma flow
Conduit wall
Magma flow (thicker arrows equal increased velocity)
N
Left margin
plane
Intrusion
Right margin
(C)
(i)
N
1 km
1
2
3
Magnetic lineation
Magnetic foliation
Magma lobe
Granite
(ii)
1
2
3

Figure 12

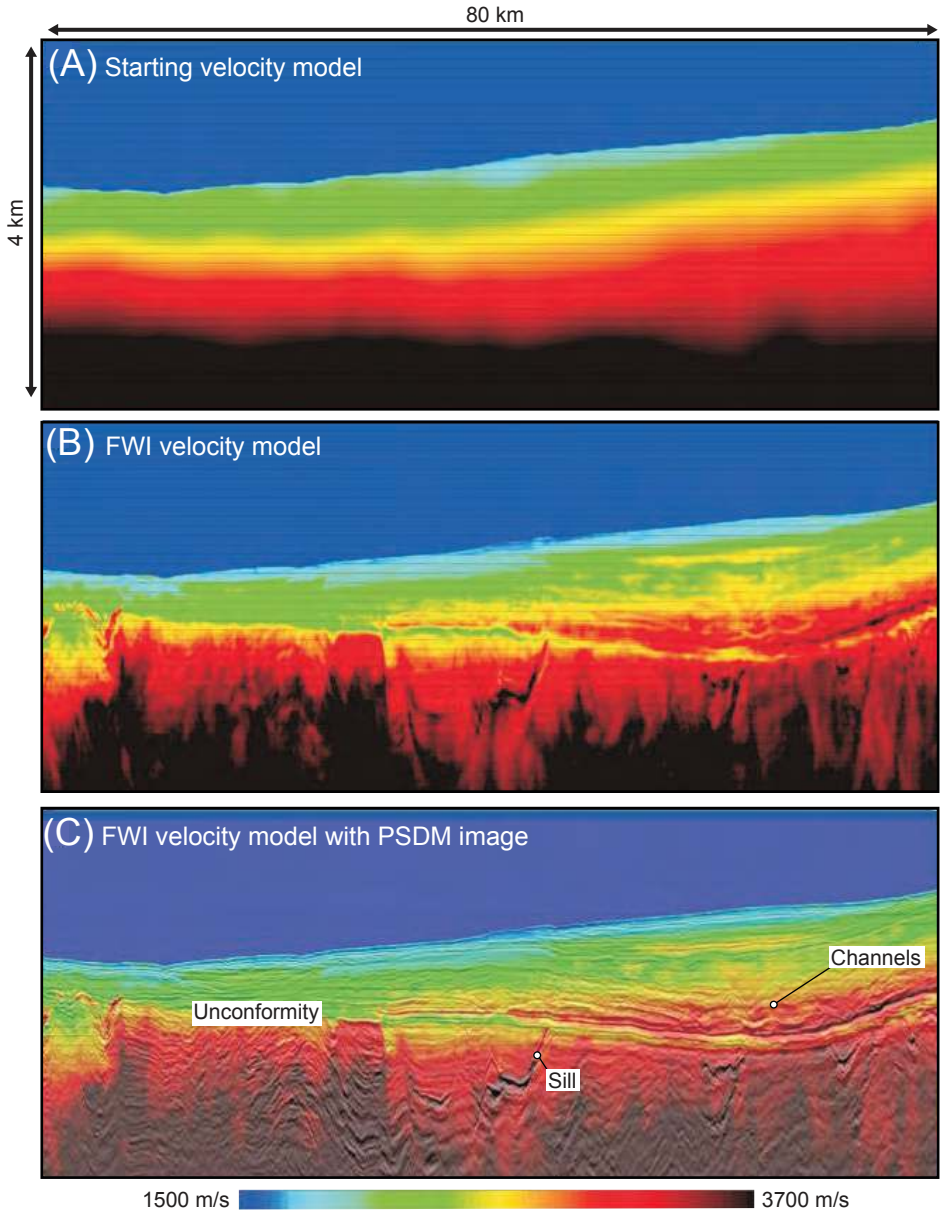
80 km
4 km
(A) Starting velocity model
(B) FWI velocity model
(C) FWI velocity model with PSDM image
Channels
Unconformity
Sill
1500 m/s
3700 m/s

Figure 13

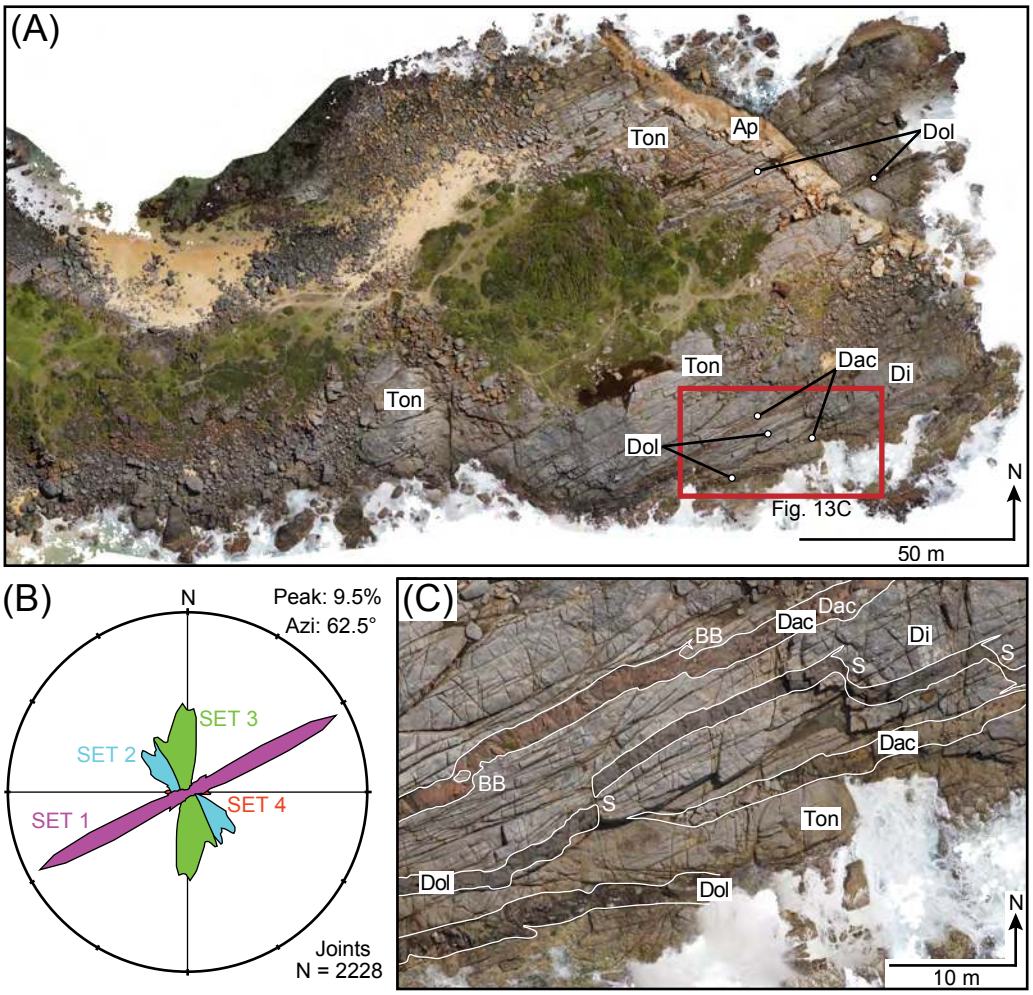
(A)
Ton
Ap
Dol
Ton
Dac
Di
Ton
Dol
Fig. 13C
N
50 m
(B)
N
Peak: 9.5%
Azi: 62.5°
SET 3
SET 2
SET 1
SET 4
Joints
N = 2228
(C)
BB
Dac
Dac
Di
S
S
Dac
BB
S
Ton
Dol
Dol
N
10 m